# Advanced Welding Manufacturing: A Brief Analysis and Review of Challenges and Solutions

**Yu Ming Zhang**[1]
Department of Electrical and Computer Engineering,
Institute for Sustainable Manufacturing,
University of Kentucky,
Lexington, KY 40506
e-mail: yuming.zhang@uky.edu

**Yu-Ping Yang**
Edison Welding Institute,
Columbus, OH 43221
e-mail: yyang@ewi.org

**Wei Zhang**
Department of Materials Science and Engineering,
The Ohio State University,
Columbus, OH 43221
e-mail: zhang.3978@osu.edu

**Suck-Joo Na**
Department of Mechanical Engineering,
KAIST, Daedeok Innopolis,
Daejeon 34141, South Korea
e-mail: sjoona@kaist.ac.kr

*Welding is a major manufacturing process that joins two or more pieces of materials together through heating/mixing them followed by cooling/solidification. The goal of welding manufacturing is to join materials together to meet service requirements at lowest costs. Advanced welding manufacturing is to use scientific methods to realize this goal. This paper views advanced welding manufacturing as a three step approach: (1) pre-design that selects process and joint design based on available processes (properties, capabilities, and costs); (2) design that uses models to predict the result from a given set of welding parameters and minimizes a cost function for optimizing the welding parameters; and (3) real-time sensing and control that overcome the deviations of welding conditions from their nominal ones used in optimizing the welding parameters by adjusting the welding parameters based on such real-time sensing and feedback control. The paper analyzes how these three steps depend on process properties/capabilities, process innovations, predictive models, numerical models for fluid dynamics, numerical models for structures, real-time sensing, and dynamic control. The paper also identifies the challenges in obtaining ideal solutions and reviews/analyzes the existing efforts toward better solutions. Special attention and analysis have been given to (1) gas tungsten arc welding (GTAW) and gas metal arc welding (GMAW) as benchmark processes for penetration and materials filling; (2) keyhole plasma arc welding (PAW), keyhole-tungsten inert gas (K-TIG), and keyhole laser welding as improved/capable penetrative processes; (3) friction stir welding (FSW) as a special penetrative low heat input process; (4) alternating current (AC) GMAW and double-electrode GMAW as improved materials filling processes; (5) efforts in numerical modeling for fluid dynamics; (6) efforts in numerical modeling for structures; (7) challenges and efforts in seam tracking and weld pool monitoring; (8) challenges and efforts in monitoring of keyhole laser welding and FSW; and (9) efforts in advanced sensing, data fusion/sensor fusion, and process control using machine learning/deep learning, model predictive control (MPC), and adaptive control.*
[DOI: 10.1115/1.4047947]

*Keywords: welding, manufacturing, numerical model, weld pool, transport phenomena, microstructure, distortion, residual stress, process, sensor, machine learning, deep learning, CNN, adaptive control, model predictive control, MPC, control, automation, modeling, simulation, sensing, monitoring, diagnostics, sensors, joining*

## 1 Welding Manufacturing Problems

**1.1 Welding Manufacturing.** Manufacturing is the production of products for use or sale using labor and machines, tools, chemical or biological processing or formulation and is the essence of secondary industry. The term may refer to a range of human activity from handicraft to high tech but is most commonly applied to industrial design, in which raw materials from primary industry are transformed into finished goods on a large scale. Here, the primary industry implies extracting, collecting, or producing directly from natural resources such as farming, mining, refining, etc., and the second industry processes the products from primary industry as raw materials to form more advanced products for use and sale.

Joining is to connect materials together in a permanent way to form a more complex structure/shape and welding joins materials through fusing materials, to be joined, to make them flowable such that part of each material involved can physically move to mix with filler material or another material involved. After solidification, the mixed materials will be joined together, either between the materials to be joined (direct joining) or through joining of the filler materials with involved materials (indirect joining) or a combination of direct and indirect joining. Because of the physical mixing of materials, welding is often considered offering stronger joining than brazing where materials to be joined are not melted and moved in any way and is thus considered the primary process for metals joining that is concerned in this paper.

Manufacturing uses available materials to produce a product for use. Designing a product to be manufactured tends to minimize the overall cost and would tend to specify what and how materials are used and, for joining involved, what are the basic requirements on finished joints. As such, the requirements on the finished welding jobs as part of the manufacturing should have been given although how to weld/manufacture to satisfy these requirements is still to determine. Ideally, such design requires knowledge of feasibility and cost of the manufacturing means proposed. Feasibility related to welding includes weldability of materials that are good for the product but may not be weldable. Finding innovative ways, often finding the filler metal composition, to make it possible to weld particular materials together is the core of welding and the field is termed weldability. In this review paper, we do not

[1]Corresponding author.
Manuscript received February 11, 2020; final manuscript received July 28, 2020; published online September 29, 2020. Assoc. Editor: Albert Shih.

consider weldability as part of welding manufacturing and wish to define welding manufacturing as to use methods with proved weldability.

As such, we broadly categorize welding studies and technologies into two categories: *feasibility* (must be considered in product design) and *manufacturing*. Welding manufacturing concerns using and integrating technologies with proven weldability for use during manufacturing.

**1.2 What Are Involved?** We take the butt joining problem as shown in Fig. 1 as an example to illustrate what are involved.

Figure 1(*a*) illustrates the requirement from a product design for welding. It requires a stainless steel (SS) sheet and a mild steel (MS) sheet, both 2 mm in thickness, be butt fused together for use in a final product. However, how to fuse them together is not specified by the product design. For the best of the finished product, we prefer them be fused together almost with no side effects: the weld width and heat-affected zone (HAZ) be very small, no distortion and residual stress on the materials, no slope change on both of the surfaces, etc., after the welding. To this end, an ideal welding process to meet such requirements is one that can apply highly localized heat to the interface and direct the heat to go in the thickness direction to all the interfaces. Electron beam (EB) may be considered such an ideal process but the product value may not justify the use of highly costly EB process.

We may use gas tungsten arc welding (GTAW) to fuse them together. Figure 1(*b*) compares the process and resultant weld between GTAW and EB. Because the density of the heat provided by GTAW is much reduced, GTAW produces much larger, wider weld using much greater heat input resulting in much greater side effects including much larger weld, HAZ, distortion, residual stress, etc. However, the cost is much lower. If the butt joint still meets the product need, GTAW would be much more preferred.

Gas tungsten arc welding may be relatively slow in comparison with another low cost arc process—gas metal arc welding (GMAW). While GTAW in Fig. 1(*b*) directly melts the materials to be fused, joining using GMAW as shown in Fig. 2 uses a gap between the two interfaces and fills the gap with a filler metal melted by the arc. This reduces the need to penetrate the materials in the thickness direction because the gap allows the interfaces to be easier for access by the arc/heat. However, it requires a highly efficient way to melt the filler metal. We know that this is the basic advantage of GMAW. Because of the reduced need to penetrate the materials and the highly efficient melting of filler wire, GMAW can fuse the stainless steel and mild steel sheets at high speed. In addition, the cost is also low and the side effects may be comparable with those of GTAW. There may be slight reinforcements/convexities on the finished weld but they should be acceptable for many products.

The above example and analysis suggest that welding manufacturing first requires a *pre-design* that determines which process and joint design be used. *Available processes, their properties/capabilities and costs* play important roles in making such pre-design decision. In the above example, we tend to choose GTAW over EB or to choose GMAW, if the requirement for the finished weld is not extremely high especially for reinforcements/convexities of the finished weld, based on process availability, capability, and cost.

We further take using GMAW as example to discuss our topic, welding manufacturing, further. The next issue is what welding parameters as denoted by vector $\varpi$ should be used to actually perform the butt welding/manufacturing for the particular materials in our application. This is the *design* of welding manufacturing and it is typically considered an optimization problem. To state more clearly, we first define a set of outputs $o$ as our major concern for the particular application that may include, but not limited to, the measures for the weld size/geometry, heat input, distortion, residual stress, microstructure, etc. The optimization problem may be considered to minimize a (scalar) semidefinite positive function $P$

$$\min_{\varpi} P(o(\varpi/\kappa)) \tag{1}$$

with respect to variable vector $\varpi$, where $\kappa$ represents given welding conditions/welding parameters that are considered invariant here, and $P$ is a semidefinite positive function of vector $o$. $o(\varpi/\kappa)$ suggests that the outputs ($o$) are controlled by $\varpi$ and gives the relationship between $o$ and $\varpi$ under given $\kappa$.

As can be seen, the optimization problem is mathematically solvable only when $o(\varpi/\kappa)$ is available. This is the *predictive model* that can either be an empirical model obtained using experimental data or be a numerical model. Empirical models are widely used and can be easily mastered but the effectiveness is limited to the range of the experimental data and restricted by the experimental conditions. Numerical models are more complex but provide insightful information and are more transparent with better confidence. For **advanced welding manufacturing**, *numerical models* are considered needed tools as the basis to generate the needed predictive models.

In certain applications, we may further specify the requirement for each measure in $o$. The specification is typically given by the limits for each measurement. In such cases, the design problem becomes a constrained optimization problem. If the welding parameters are also subject to constraints $\varpi^{(L)} \le \varpi \le \varpi^{(U)}$ as should be, the problem becomes

$$\begin{cases} \min\limits_{\varpi^{(L)} \le \varpi \le \varpi^{(U)}} P(o(\varpi/\kappa)) \\ o^{(L)} \le o(\varpi/\kappa) \le o^{(U)} \end{cases} \tag{2}$$

where vector $o^{(L)}$ and $o^{(U)}$ specify the lower and upper limits for each of the measure in $o$. We may denote the result as

$$\begin{cases} P(o(\varpi^*/\kappa^*)) = \min\limits_{\varpi^{(L)} \le \varpi \le \varpi^{(U)}} P(o(\varpi/\kappa^*)) \\ o^{(L)} \le o(\varpi/\kappa^*) \le o^{(U)} \end{cases} \tag{2a}$$

where $\kappa^*$ is the given $\kappa$ used in the optimization referring to the *nominal conditions*, $\varpi^*$ is the solution under the nominal conditions $\kappa^*$. The particular value $o(\varpi^*/\kappa^*)$ may be denoted as $o^*$, i.e., $o^* = o(\varpi^*/\kappa^*)$.

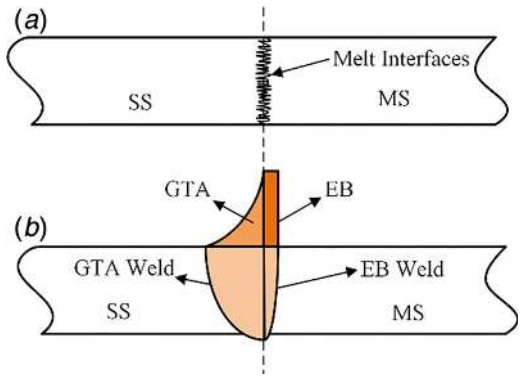


**Fig. 1 Design requirement and candidate predesigns—a welding example: (*a*) illustration of design requirement and (*b*) comparison between two candidate predesigns. SS, stainless steel; MS, mild steel.**

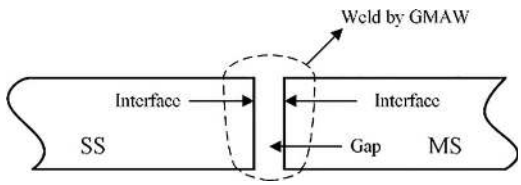


**Fig. 2 A more competitive pre-design based on available process properties**

With the designed welding parameters $\varpi^*$, the welding manufacturing can be carried at manufacturing sites. We note that there must be deviations $\Delta\kappa$ of the actual welding conditions $\kappa$ (including some welding parameters counted as given conditions) from those ($\kappa^*$) in the predictive models/numerical models. To distinguish, those used in the models or solved from the design are referred as to nominal ones ($\varpi^*$, $\kappa^*$). If the actual manufacturing conditions $\kappa$ and welding parameters $\varpi$ are the same as the nominal ones, we should expect the actual $o$ to be close to the predicted $o$, i.e., $o^*$. However, while we may automate the process to assure the actually delivered $\varpi$ have no essential differences from $\varpi^*$, maintaining the actual manufacturing conditions $\kappa$ the same as the nominal ones $\kappa^*$ may be too costly for welding manufacturing.

Some of the welding manufacturing conditions may be correctible such as the weld seam. By online sensing of some $\kappa$, especially most important ones, we can make adjustments such that important components $\kappa^*$ are maintained at a cost-effective way to help welding manufacturing to deliver the designed results. However, some of the welding conditions may not be easily measurable or not measurable at all or even if measurable but not online correctible. In such cases, we would need to actually measure the results $o$ in real time if possible and then adjust some or all of the welding parameters $\varpi$ from their designed ones $\varpi^*$ within the permitted range to compensate the effect from uncorrectable $\kappa$ components. Ideally, this is to minimize

$$\min_{\Delta\varpi} P(o(\varpi = \varpi^* + \Delta\varpi/\varpi^*, \kappa^*, \Delta\kappa)) \tag{2b}$$

where the deviation $\Delta\kappa$, nominal $\kappa^*$ (thus $\kappa = \kappa^* + \Delta\kappa$), and $\varpi^*$ are given. In real-time implementation, implementing this optimization is difficult (or impossible if $\Delta\kappa$ is not measured/known) and the problem is converted to a feedback control one for example a model predictive control (MPC) problem that predicts the future $o(t+\tau)$ as a function of the present adjustment $\Delta\varpi(t)$ and future adjustments $\Delta\varpi(t+\tau)$ ($\tau > 0$) and optimizes $\Delta\varpi(t)$ and $\Delta\varpi(t+\tau)$ such that $o(t+\tau)$ be maintained at, close to, the designed value $o^*$.

**1.3 Issues in Advanced Welding Manufacturing.** Figure 3 can be used to summarize the welding manufacturing problem and extract the major issues in advanced welding manufacturing for this review paper to cover.

As can be seen, (1) for the pre-design, the solution improves as the availability of processes with different capabilities at lower costs increases. This calls for innovations of processes with different desirable capabilities. (2) For the design, the key is the predictive models that are capable of predicting behaviors of and results from the processes. This calls for availability of powerful numerical models that can provide realistic solutions. (3) For the manufacturing phase, online sensing and feedback control are the keys to accommodating the deviations from the design to still achieve results as close as possible to the designed ones. In this keynote paper, we will analyze respective challenges and review solutions for how they have addressed some or all these respective challenges.

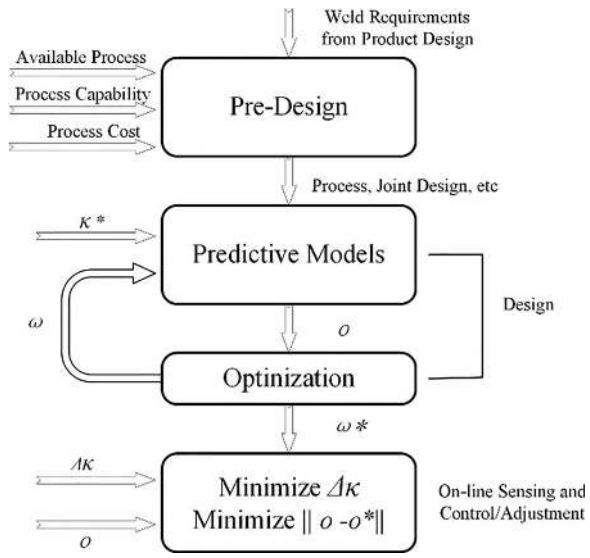


**Fig. 3 Decomposition of advanced welding manufacturing problem**

## 2 Analysis of Desirable Process Properties and Challenges

Advanced welding manufacturing begins at the pre-design (Fig. 3) that determines which process and joint design to be used from the *Available processes, their properties/capabilities, and costs* based on weld requirements from product design. We below first analyze what are the common desirable process properties that help better meet welding manufacturing goal—producing welds to meet service needs at minimized costs.

**2.1 Analysis of Desirable Process Properties.** Welding processes serve to provide best possible solution to make welds as required by the final product. Figure 4 shows five basic joint designs that may be welded as butt (A and E) and fillet (B, C, and D) welds. For sheet metal, B may also be joined using spot weld. In this review paper, we will focus on butt and fillet welds only, without covering spot welding. While butt weld has been explained in Fig. 1, Fig. 4(*c*) can be used as fillet weld example.

*Penetrative process/property*: For butt joint, if there is no gap or groove (as referred to as the benchmark butt weld problem in this paper), the objective of welding is to melt the interfaces of the two metal members (Fig. 5). A heat distributed on the interfaces would realize the objective in an ideal way and can be achieved by processes like friction welding [2]. However, such processes are not always convenient for most structures and a typical realistic solution is to apply an energy beam as shown in the figure. That is, the beam with a radius $r$ is symmetrically applied from the upper surface along the $z$ axis direction with the beam center aiming at the origin $o$.

The goal of welding is to melt each of the two interfaces just with a minimal thickness $\varepsilon$ as shown in the figure. To this end, the heat applied from the upper surface must transfer along the $z$ axis direction through the entire thickness $\delta$. However, the heat also transfers radially in $x$ and $-x$ directions in Fig. 5. A side effect of the radial transfer of heat is that the actual $w(z) - \varepsilon \gg 0$. From this point of view, an ideal heat source for the benchmark butt joint problem, without gap or groove, should be a penetrative one that directs its heat in $z$ (thickness) direction and have its $r \to 0$.

The above discussion is about the heat flux imposed on the surface of the work-piece. A heat source has properties more than just the heat flux. Another important property is its pressure imposed on the work-piece. A large pressure along $z$ direction helps the heat to transfer along $z$ direction to make the heat source to be more penetrative.

As such, for the benchmark butt joint welding (butt welding), penetrative capability is the major requirement for the process. As discussed, reducing the energy beam radius and increasing the pressure both tend to increase the penetrative capability. Plasma arc welding (PAW) [3] does both, reducing the radius and increasing the pressure. Other method to increase the penetrative capability includes changing the fluid flow from radial to digging as in A-TIG [4–6]. Laser is probably the most widely used penetrative process that reduces energy beam radius. Its increased pressure is a byproduct of reducing energy beam.

*Filling process/property*: The cross section shown in Fig. 6 is from Fig. 4(*d*) and is used here to illustrate the original/benchmark fillet joint problem. The ideal result is a weld that has a minimal

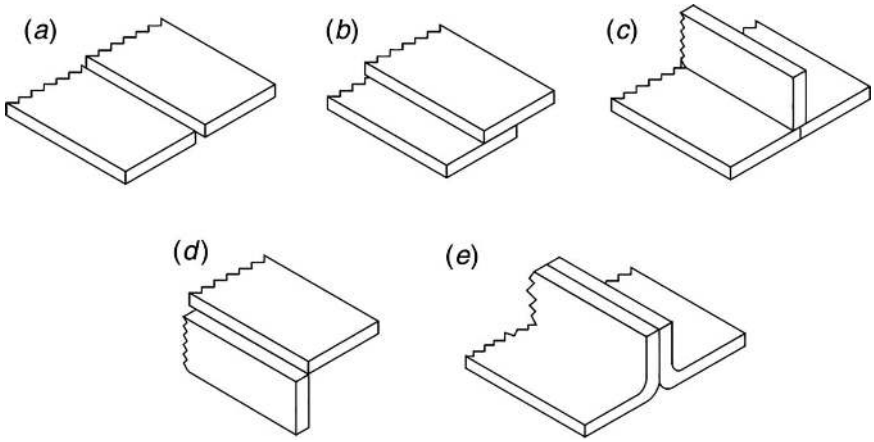


**Fig. 4 Five basic joint designs: (*a*) butt, (*b*) lap, (c) TEE, (*d*) outside corner, and (*f*) edge [1]**

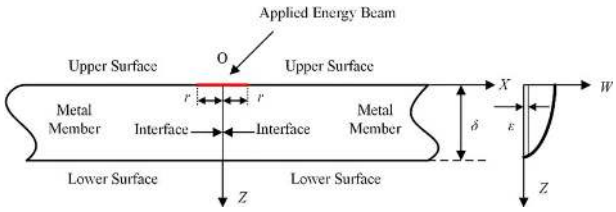


**Fig. 5 Illustration of benchmark butt weld problem**

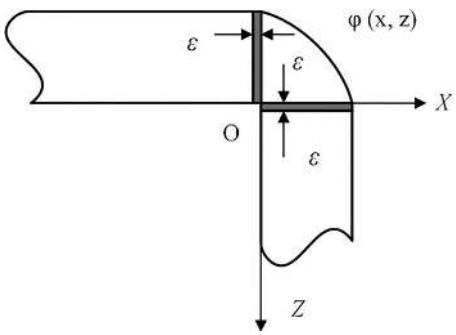


**Fig. 6 Illustration of benchmark fillet joint**

thickness $\varepsilon$ in both members of the work-piece and a fill-up contour similar as $\varphi(x, z)$ (slightly convex) with $\min H \le |\varphi(0, z)| \le \mathrm{s}H$ and $\min W \le |\varphi(x, 0)| \le \max W$, that is, the height and width of the weld are within the specified ranges. In this case, the *work-piece direct heat* (directly imposed on the work-piece) should be relatively small or controllable. *Wire direct heat*, heat directly melting the filler metal, must be sufficient and it will also be indirectly applied into the work-piece due to the transfer of the melted wire metal into the work-piece.

Now it is clear that we have at least one requirement for an ideal filling process: providing the needed/sufficient, and relatively large amount of, wire direct heat to melt filler metal at high speed for high productivity and imposing only the needed/sufficient, but relatively small and controllable amount of, work-piece direct heat on the work-piece. We note that forming the weld shape desired as described above first requires the two sides of the fillet joint be directly heated sufficiently and evenly. This requires a distributive heat source that can directly impose distributive heat on the needed areas work-piece. A desirable penetrative heat source will tend to apply more direct work-piece heat around the origin. For fillet joint, such a heat source would reduce the weld height $|\varphi(0, z)|$ and width $|\varphi(x, 0)|$ and increase the convexity of the weld profile $\varphi(x, z)$. This implies wasting filler metal and increasing heat input, distortion, and residual stress.) As such, *controllable heat proportion* between wire and work-piece direct heats and *controllable heat distribution* are the two desirable properties for an ideal filling process.

For all processes, *productivity/speed*, *quality*, and *cost* are important properties and all process innovations must take them into consideration.

**2.2 Challenges.** *Penetrating benchmark process*: We analyze from autogenous GTAW [3] as the benchmark for a penetrative process. Figure 7 shows the principle of the process. In benchmark GTAW, the tungsten electrode is connected to the negative terminal of the power source and the work-piece is connected to the positive terminal. In this process, the tungsten electrode is used to emit electrons. If the gap between the electrode and the work-piece becomes conductive, the electrons can emit from the electrode and flow through the conductive gap to the work-piece. The electrons enter from the gap into the work-piece. To be conductive, the gas in the gap must be ionized. To maintain being ionized, the temperature must be sufficiently high. The ionized gas is the arc plasma [7] forming the arc column. A conventional welding arc has one cathode to emit electrons, arc column to allow the electrons to flow, and an anode to receive electrons. The current passing through each of them is exactly the same. However, their voltage drops are different. Tungsten electrode is alloyed to make electrons easily to emit such that the cathode voltage in GTAW is very low and the power consumed/wasted on the electrode is small. Because of the high melting point, the tungsten is also not melted.

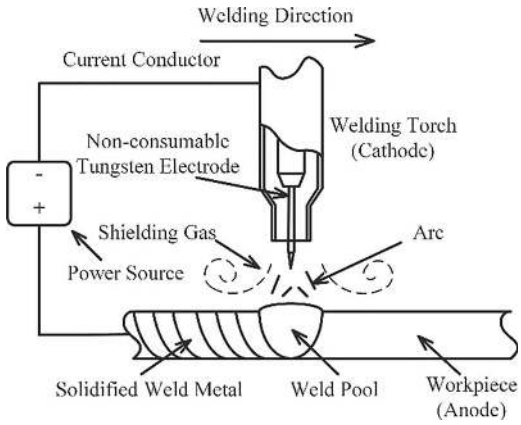


**Fig. 7 Autogenous GTAW**

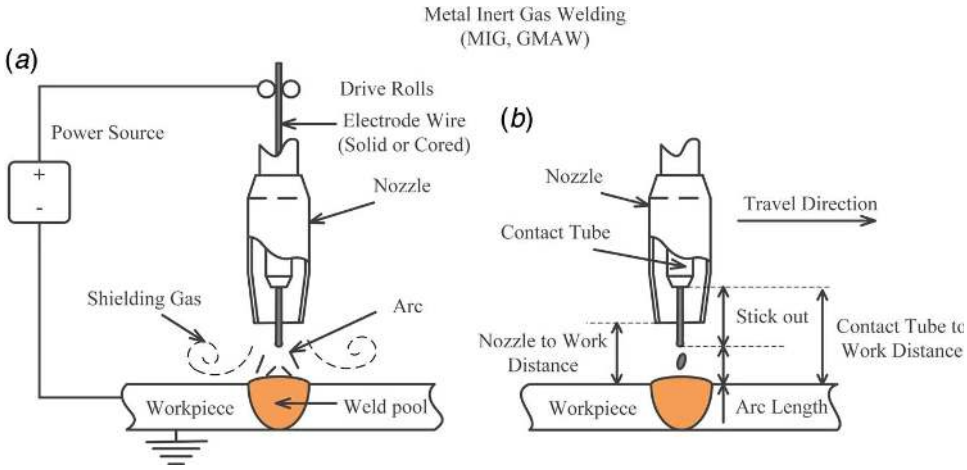


**Fig. 8 Benchmark GMAW: (*a*) overall system and (*b*) arcing system**

Because of the high temperature needed to maintain the ionization, the ionized gas tends to expend radially. The current density thus decreases as the electrons leave from the electrode. The electrons become more distributive on their path after the emission. As a result, the current distribution on the work-piece must increase. Hence, although the voltage drop on the work-piece anode is much greater than that of the arc column and of the cathode such that the heat flux directly imposed on the work-piece is large, the heat flux is distributive such that the energy beam radius $r$ cannot be as small as desired.

As can be seen, the challenge toward a desirable penetrative process for the GTAW is due to the mechanism of arcing that cannot work without the conductive gas and the anode voltage drop, needed for the power of anode $V_{\text{anode}}I$, only occurs when the electrons flow between gas and solid/liquid. Maintaining the gas to be conductive must maintain ionizing the gas for it becomes high temperature. Unrestricted gas must expend at elevated temperatures. The anode on the work-piece thus becomes distribution such that the density of the power $V_{\text{anode}}I$ imposed on the work-piece is small or the diameter is large.

*Filling benchmark process:* We now analyze from GMAW [3] as the benchmark for filling process. Figure 8 illustrates this process. A wire is continuously fed to the torch and is guided by the contact tube toward the work-piece. The contact tube is typically connected to the positive terminal of the power source while the work-piece to the negative. The wire, by passing the contact tube, becomes electrically positively charged. While in GTAW process, the electrode is un-melted, the electrode/wire in GMAW will be melted to become part of the weld metal. Also, the work-piece is whatever metals being joined. The materials of the electrode/wire and work-piece are thus not selectable but given. As a result, the cathode/work-piece cannot be selected to ease the emission of the electrons. The cathode voltage drop is not freely controllable.

Unlike in GTAW where an alloyed tungsten electrode is used to minimize the cathode voltage, the cathode voltage drop in GMAW is typically large. For steel, it is approximately twice of that of the anode voltage [8].

To maintain an arc, the melted wire, that forms a droplet at the tip of the wire, needs to be detached from the wire before it touches the work-piece. The electromagnetic force is the major force that detaches the droplet from the wire [9,10]. For the electromagnetic force to be detaching force rather than retaining force, the wire must be connected to the positive terminal. As such, the work-piece must be the cathode. When the current is the same as in conventional arc welding process, the power at the anode to melt the wire is thus only a half of the power at the cathode/work-piece.

For a filling process, the first desirable property is the controllability of the heat proportion among the wire and work-piece direct heats. However, in benchmark GMAW process, this proportion is approximately fixed due to that both the polarities and materials of the electrode/wire and work-piece are not freely selective and are given. In addition, for filling process, achieving high productivity implies a high proportion of the wire direct heat in order to add filler metal onto the work-piece quickly. For the second desirable property, i.e., distributive energy beam, we note that the energy beam in benchmark GMAW is distributive but approximately fixed again due to the similar need for maintaining the gas ionized as in GTAW.

*Productivity, quality, and cost:* For all process innovations, achieving high quality welds at high productivity/high welding speed and low cost is always challenging. The challenges vary and depend on the specific innovations and their mechanisms.

## 3 Process Innovations

We above analyzed what are the common desirable process properties and what are the difficulties in achieving these desirable properties. The desirable process properties identified through the analysis are the penetrative and filling capabilities. This section reviews efforts in process innovation to improve these two capabilities.

**3.1 Penetrative Process.** The penetration capability has been improved by reducing energy beam diameter and directing the heat vertically through different process innovations from the benchmark GTAW process. A major method is to establish a keyhole such that the energy beam can be directly penetrating into the thickness direction, rather than heating the surface and relying on the heat to transfer through liquid metal. However, the control of the keyhole process is relatively complex and the cost to concentrate the energy beam is relatively expensive. Another method is to change the fluid flow pattern in the liquid metal.

*Plasma arc welding* [3]: In the benchmark autogenous GTAW (Fig. 9 left), the shield gas is fed through the nozzle toward the work-piece. After the nozzle, the restriction on the shield gas is lifted such that the pressure is reduced and the gas is free to expand. Since the nozzle diameter is relatively large in order to provide the shield gas to shield the hot metal from oxidation, the shield gas is relatively widely distributed. The existence of the ionizable gas provides the condition for the arc plasma of highly elevated temperature to expand. In addition, the speed of the shield gas feeding is relatively slow such that the gas has relatively long time to expand.

Plasma arc welding (Fig. 9 right) is a modification of the GTAW. As shown in Fig. 9, there are two isolated gas chambers, shielding gas (outer one) and orifice gas (inner one), and the gases for the two chambers are separately supplied. The tungsten electrode resides in

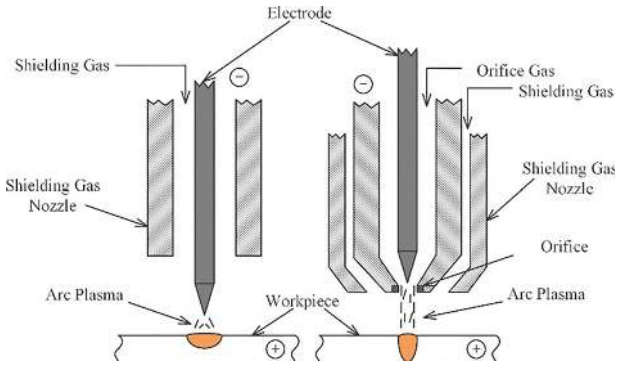


**Fig. 9 Plasma arc welding in comparison with GTAW [3]; left: GTAW and right: PAW**

the inner chamber and the gas exit (orifice) of the inner chamber is small, 1–2 mm in diameter typically. As such, the arc plasma (ionized gas that conducts the current) is restricted by the orifice (small exit). Because its diameter is very small, the orifice gas can exit at high speed as a jet from the orifice chamber. The time for it to expand, before reaching the work-piece, is much reduced such that the diameter of the plasma jet may still be small when it arrives on the work-piece. As such, the diameter of the energy beam imposed on the work-piece is much reduced from the benchmark GTAW process. Also, because of the high speed of the plasma jet, a high impact/pressure is imposed on the liquid weld pool. It can displace the liquid metal to generate the concavity on the weld pool surface such that the energy beam is applied on the bottom of the concave upper surface. This helps the heat be directed vertically in the thickness direction when the torch aims at the normal of the upper surface of the work-piece. The process has been combined with gas metal arc welding (also known as metal inert gas (MIG) welding) to form plasma-MIG process to achieve penetration and deposition at the same time [11,12].

One issue PAW must avoid is the double arcing [13]. Since the diameter of the orifice is small, the orifice (exit of orifice gas/plasma jet) is subject to high temperature and will be easily damaged if not appropriately cooled. It thus should be made from highly heat conductive metal, typically bronze, and strongly cooled. Since it must restrict the plasma jet, the plasma jet may reach it. If this occurs, an arc will be established between the tungsten and the orifice and then another between the orifice and work-piece. The arc imposed on the work-piece will be the latter such that the energy beam is no longer subject to any restriction and will become a free arc with large diameter like a gas tungsten arc. Hence, strong cooling is needed to keep the orifice at lower temperature. The gas close to the orifice, or the gas around the outer diameter of the plasma jet, is thus low in temperature and is not ionized. The current flow can thus be constricted by the orifice. To this end, for the same torch and cooling condition, the minimal orifice diameter that may be used increases as the welding current increases.

Plasma arc welding is applied in two modes: keyhole [14] where the melted metal is displaced by the high temperature high pressure plasma jet such that the plasma jet can penetrate through the entire thickness of the work-piece to form a through-cavity referred to as keyhole (Fig. 10(*a*)), and melt-in where the concavity caused by the plasma jet is relatively small. Because of the keyhole, part of the heat from the source is directed along the thickness direction to the interfaces directly. The loss through heat transfer into the metal work-piece is reduced. Keyhole PAW can thus penetrate 10 mm steel in a single pass as shown in the cross section of sample in Fig. 10(*b*) that was produced at the University of Kentucky Welding Research Laboratory. Melt-in mode can improve the penetration capability due to the reduced energy beam diameter and increased pressure. However, it may produce a partial keyhole that is not through the entire thickness of the work-piece to allow the gas to exit from the lower surface of the work-piece (Fig. 11) and cause gases be trapped in the weld metal (Fig. 12). As such, the improvement achieved by the melt-in mode over the GTAW is relatively limited and may not also be justified for using a more complex equipment that requires higher labor skills.

*Keyhole-tungsten inert gas (K-TIG)* [15–19]: In PAW, the plasma jet is constricted by the orifice that is highly cooled such that the gas in its vicinity is not ionized. This requires an inner chamber making the torch to be more complex than that of the GTAW. K-TIG (keyhole TIG where TIG, tungsten inert gas, is the term of International Institute of Welding (IIW) for GTAW) highly cools (by the cooling shoulder in Fig. 13) the tungsten. As illustrated in Fig. 13, the tungsten is much cooler and the electrons can only emit from a much smaller region at the tip of the tungsten electrode. Because of the reduction in the emission area where the electron flow originates, the diameter of the electron flow when encountering the work-piece is reduced (Fig. 13 right). However, this is still not sufficient to drastically increase the penetration capability. Hence, to achieve the keyhole, the process must also use a very high current. Because the arc pressure is proportional to the square of the current, a very high arc pressure becomes available to displace the liquid metal to dig into the liquid pool to form a keyhole.

Although K-TIG equipment arguably becomes simpler than that of PAW, the mandatory need for high current makes its application range be narrowed. The energy beam is reduced but is still larger than that of a plasma arc. The electrons not only enter the work-piece at the lower part of the keyhole surface but also at upper and middle surfaces where the anode voltage drop occurs and the

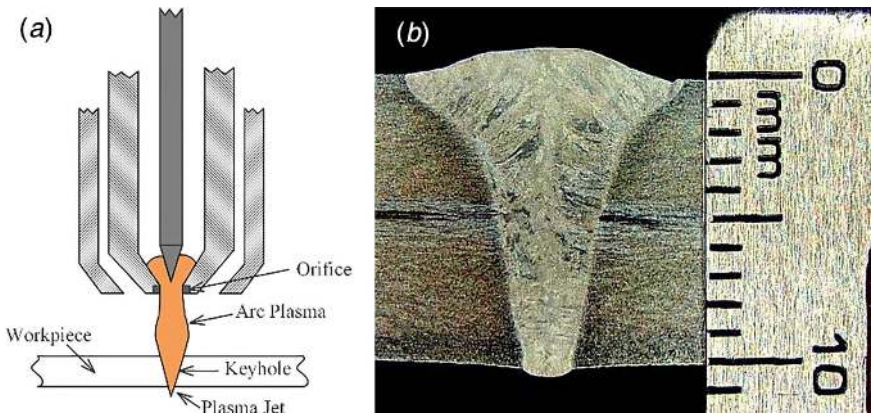


**Fig. 10 Keyhole PAW: (*a*) keyhole and (*b*) a weld sample by keyhole PAW from University of Kentucky**

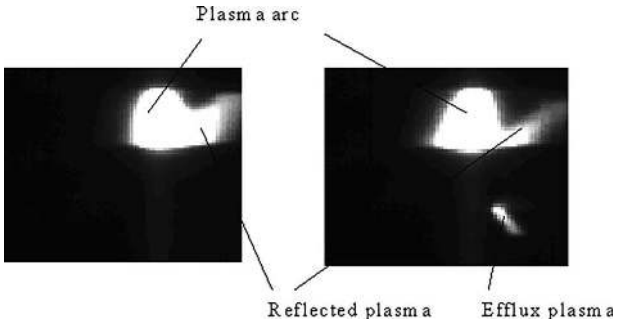


**Fig. 11 Comparison between partial and complete keyhole. Left: partial and right: complete. Efflux plasma at the lower surface indicates a complete keyhole for the gas to exit. Efflux plasma reduces the plasma reflected from the upper surface.**

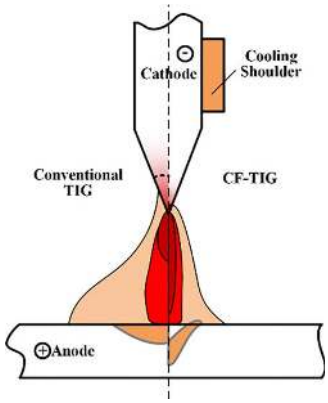


**Fig. 13 Comparison between conventional GTAW/TIG and K-TIG [19]**

heat input through anode spreads on the weld pool/keyhole surface. To maintain the keyhole, the liquid metal must be sufficient such that the heat input must be over supplied into the work-piece. The weld becomes large making the stability of the process and the weld pool a major concern [19–23].

Because of the large heat input in a single pass, the materials properties become a concern. Studies have been conducted for particular materials/applications to evaluate its feasibility [24–27]. Studies have uncovered that in many applications, K-TIG supplies similar heat input into the work-piece and achieves similar acceptable materials properties as multiple pass processes. However, it appears that such results should be materials and applications dependent and may not be always true in general. In conventional multiple pass processes, the heat is applied multiple times. The resultant effect on the cooling and metallurgical properties must be different from being applied in one time.

*Laser keyhole welding*: The most widely used penetrative process is probably the laser keyhole process. While EB process requires vacuum, this is not the case for laser. In addition, many high-power lasers can be easily transmitted by fiber optics that is bendable and flexible such that it can be easily robotized/automated. The ability of laser for keyhole welding is due to the availability of high-power laser and its capability to focus on very small dimeters. On the other hand, for arcs, the power can be high but it is difficult to focus.

Solid-state lasers with power greater than 10 kW have been made available to market [28]. Multi-kilowatt lasers have become standard for industrial applications not only on shop floors but also in fields. The power density of a high quality focused beam can exceed $10^6$ kW/mm$^2$ [29]. However, keyhole welding requires smaller power density than cutting. The needed power density is in the order of $10^4$ kW/mm$^2$ [30] but there are reports that the keyhole be established at lower power density.

Stanciu et al. [30] provided a comprehensive survey for laser keyhole welding including the mechanism that is illustrated in Fig. 14. When a laser is applied onto the material, part of the laser energy transfers to the interaction surface from photons to electrons through the Inverse Bremsstrahlung absorption. If the power density is adequate, the surface is not only melted quickly but also partially vaporized. The vaporization generates a large recoil force that can depress the surface of unvaporized liquid metal. This allows the laser to be applied beyond the original work-piece surface to further the vaporization. The surface depression is also further deepened into a cavity. As the cavity deepens, the laser beam reflects within the cavity from the inner surface that is irregular in shape. This involves the Fresnel absorption such that the laser energy is just partially absorbed. However, the rest is reflected by the walls whose surface is liquid and mirror like specular such that part of the laser energy continues to propagate to be reflected to go deep. As a result, the cavity may be established deeply. The diameter of the deep cavity, approximately that of the beam diameter, is small such that the cavity is referred to as keyhole.

Lasers have been successfully used to keyhole weld different materials at high speeds. However, using high-power lasers to keyhole weld thick materials to produce defect free welds is challenging. Underfills, undercuts, porosities, irregular/unsmooth backside beads, etc., are often associated with this extremely violent and fast process. Needs for precision fit-up introduce another significant issue. Efforts have been taken to address these issues and many papers have been published. For example, Zhang et al. [31] used a 10-kW fiber laser to keyhole weld 12 mm-thick stainless steel plates autogenously and studied how to resolve the underfill issue. In another example, Matsumoto et al. [32] investigated high-power fiber laser welding on 12 mm thick high-strength steel for effects of laser focusing properties on weldability. To this end, two optics systems were used to provide different power density distributions and focus depths. Full penetration welds without weld defects were obtained with the 4 mm focus depth optics system at low welding speeds of 25–50 mm/s. They used high-speed video and X-ray transmission images to find that keeping

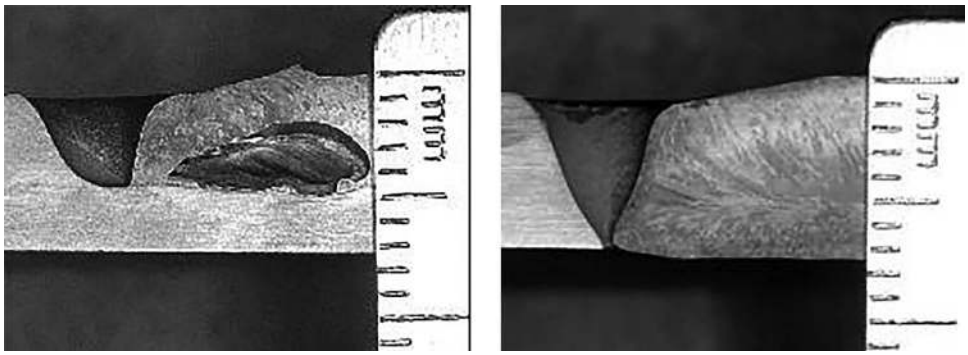

**Fig. 12 Gas trapping issue in partial keyhole; left: partial and right: complete**

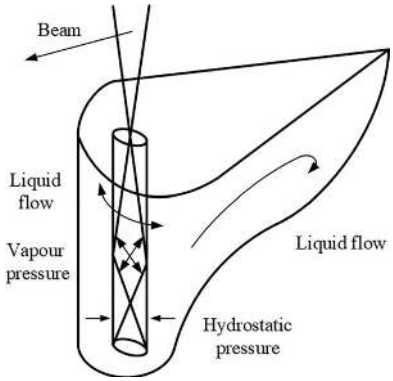


**Fig. 14 Laser keyhole principle [30]**

the power density within 50–120 kW/mm$^2$ maintains the keyhole shape stable. They concluded that focusing properties affected the weldability strongly during laser welding of the thick steel plate and that a long focus depth was particularly useful in producing sound welds. To overcome the fit-up issue, a common solution from process is to use a laser together with an arc to perform hybrid welding [33,34] that may be simply considered as arc melting the surface for the laser to initiate the interaction with the material.

*Issues with keyhole welding*: While the use of high temperature high pressure energy jet in PAW or high-power density laser or EB increases the penetrative capability, it may adversely affect the weld quality. One issue is to make sure that no gas is trapped (Figs. 11 and 12). Maintaining a continuously open keyhole serves this purpose well but the exiting energy (such as the efflux plasma in PAW as in Fig. 11), if still strong (high temperature high pressure), may detach some liquid metal away and cause irregular weld bead shape on the lower surface (as in PAW in Fig. 15). When significant amount of liquid metal is detached from the workpiece, the keyhole may not be filled after the energy jet moves forward. This causes cutting rather than joining. The solution is to maintain moderate heat input and pressure but this is challenging.

A successful method to address this challenging issue is to periodically open and close the keyhole [35–39] in PAW. It has been termed as quasi-keyhole. By opening the keyhole, the gases can escape and the needed full penetration through the entire thickness can be assured without gas trapping issue. By closing the keyhole, the metal detachment can be minimized to avoid possible cutting through; the weld bead on the lower surface can also be better controlled. That is, after the keyhole is closed, the pressure from the arc on the lower surface of the weld pool is much reduced; the shape of the weld pool surface on the lower surface is then controlled by the surface tension resulting in smoother weld contour. Of course, the period should be carefully selected and controlled. To this end, we can monitor the keyhole state and then adaptively adjust the current. Figure 11 shows different phenomena in partial and complete keyhole as indicated by the reduced amount of the reflected plasma and the existence of the efflux plasma for the complete keyhole. At the University of Kentucky, the keyhole state has been monitored from electrical signals that are determined by the reflected and efflux plasma [35–39] and been controlled using advanced model predictive controls [36,39]. While the pioneering works were conducted at the University of Kentucky, significant works [40–49] have also been done at Shandong University to analyze, sense, and control keyhole PAW process.

*A-TIG* [4]: In general, keyhole processes are violent and achieve deep penetration at the expenses of possible gas traps/porosities and irregular backside weld beads as above analyzed in addition to other issues including underfills, undercuts, high cooling rates. There are not many solutions for deep penetration without using a keyhole. One solution is the A-TIG that is exactly the same as GTAW except for applying a thin layer of activating flux on the area of arc application. The flux consists of elements that change the sign of the surface tension gradient coefficient from positive to negative. This changes the direction of the surface tension-driven fluid flow, from flowing from high temperature to lower temperature region to flowing from lower temperature to higher temperature region. This implies that the liquid flows on the weld pool surface from the edge toward the center where the temperature is supposed to be the highest and then flows down into the thickness direction. The heat is transported to penetrate the work-piece in the thickness direction such that the penetration is improved.

Although A-TIG avoids the issues associated with using a keyhole, adding flux into the weld pool may adversely affect the weld metallurgy and materials properties. The effectiveness in improving the penetration and minimizing adverse side effects both depend on the composition of the flux in relation to the materials to be joined. Effective flux is thus materials dependent and majority of the research focuses on finding and verifying effective flux (composition) [50–57]. Another manufacturing issue is that adding flux introduces an additional step and increases process variation sources.

**3.2 Friction Stir Welding.** There are many publications and review papers [58–61] for FSW. This process involves advancing a rotating pin/tool along the weld seam. The material in contact with the advancing rotating pin is plasticized due to the friction to become flowable. The flowable material is restricted by solids from all directions including a shoulder from the top and a backing from the bottom in addition to the pin and solid material from the sides. As the pin advances, the flowable material behind fills the space left. The friction can plasticize the material but cannot really melt the material as the friction reduces after plasticization. FSW is thus considered a solid-state welding process rather than a fusion process.

The most distinguished and apparent advantage of the FSW over fusion processes is its low heat input that in generally better assures materials properties for the welds and reduces the distortion. Another major advantage is its better weldability as the plasticized materials are likely to be well mixed such that dissimilar materials joining becomes easier. It has been successfully applied into joining

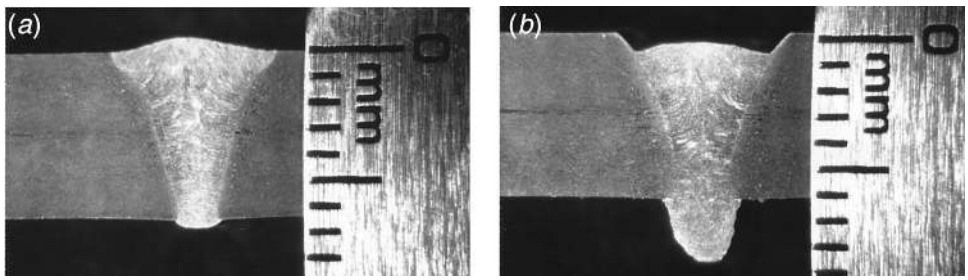


**Fig. 15 Illustration of keyhole PAW sensitivity. Beads on plate made at the same nominal conditions at slightly different travel speeds: (*a*) 2 mm/s and (*b*) 1.8 mm/s.**

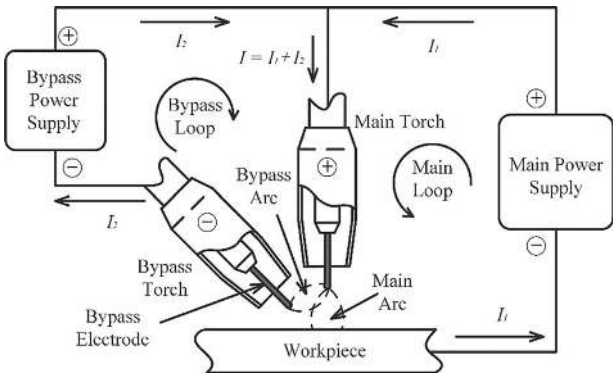


**Fig. 16 Double-electrode GMAW**

of many materials in particular light metals whose melting points are relatively low including 2XXX and 7XXX aluminum alloys that are not fusion weldable [62,63]. For example, Senthil et al. optimized process parameters to successfully weld AA6063-T6 pipes [64]; Mehri et al. [65] successfully welded 7075-T6 aluminum alloy (AA) thin sheet; Robe et al. [66] applied the rigid-ALE finite element approach that is capable of including a complex tool geometry to quickly obtain the quasi-periodic thermal state for dissimilar joining of 2XXX/7XXX aluminum alloys. As examples for dissimilar joining among light metals, Zhang et al. [67] joined AZ31/AM60 dissimilar Mg alloys using higher and lower rotation speeds (together with associated sets of parameters) to understand the effect of microstructure and texture distribution on mechanical properties and deformation behaviors; Abolusoro et al. [68] used FSW to join 6101-T6 and 7075-T651. However, when any steels are involved, the pin life becomes a concern.

We arguably classify FSW as a particular penetrative process in the sense that it achieves the goal of a penetrative process although it does not apply the energy from the top into the work-piece but from the sides. In particular, desirable properties for penetrative process include small energy beam and the capability to direct the heat through the thickness to be joined. Such properties were derived with the assumption that the heat is applied from accessible work-piece surface that is vertical to the inaccessible interfaces where heating is needed. The first result of these two properties is to generate weld that is uniform in the thickness direction. The heat transfer in the thickness direction is minimized. The second result is to minimize the heat input and its adverse heat input. For FSW, the first result is achieved by merging the tool into the entire thickness that needs to be joined. The resultant weld is considered uniform and the heat transfer in the thickness direction should be insignificant. For the second result expected from an ideal penetrative process, FSW does not achieve a narrow weld; however, the temperature is lower than the melting point and the heat input is considered minimal.

**3.3 Filling Processes.** In general, penetrative arc processes are much lower in productivity than filling processes. The reason is what needs to be penetrated is the work-piece while what needs to be melted to fill is wire. Wire is thin and can be heated directly by the arc effectively and quickly. Instead, penetrating a work-piece deeply must battle the heat transfer in other directions. Most importantly, the wire arc melting process, GMAW, and its variants can be easily automated and is very cost effective. Butt joints are thus often joined by using gap or groove to change (or shift) the problem from penetrating to filling, although gap and groove add complexity in joint preparation and introduce process variations.

*Alternating Current GMAW*: The major issue in benchmark GMAW is the uncontrollable/fixed heat proportion between the wire and work-piece. That makes that melting wire must add fixed amount of extra heat on the work-piece. We desire to provide just needed heat onto the work-piece and as much as possible heat on the wire to melt it at high speed. Another problem is that the wire has to be the anode in order to detach the droplet from the wire before it reaches the work-piece and the anode voltage drop is only ½ of the cathode voltage drop as found from uniquely designed experiments and experimental measurement system by Mendez at Colorado School of Mines and later at the University of Alberta [8,69].

The idea of the alternating current GMAW (AC GMAW) is to use the heat from the cathode to melt the wire faster and impose the anode to the work-piece to reduce the heat onto the work-piece. To this end, the wire is connected to the negative and the work-piece to the positive terminal of the power source. Of course, although this change in polarity increases heating the wire and reduces heating on the work-piece as desired, the droplet would not detach. To detach the droplet, the polarity is reversed such that the wire becomes the anode. As such, the polarity of the electricity is alternating and the GMAW process becomes AC GMAW. AC GMAW has been studied for various applications [70–75] focusing on finding right parameters and welding procedures for different materials and joint designs.

Alternating current GMAW can increase the heat on the wire and this increase can be adjustable but only within a relatively small range. Because droplet detaching is a dynamic process and does not occur right after the polarity changes, there is a time period from the polarity switch to actual detachment. The need for the wire to be the anode for each detachment has a minimal time. In addition, in GMAW, the metal transfer frequency (number of droplets detached per second) is relatively high such that each polarity changing period must be relatively small. The proportion of the time for the wire being the cathode is limited. As such, the adjustment range of the heat proportion is not desirably wide. The cost is the increased complexity, of the equipment and its use, and the increased parameters.

*Bypass GMAW or double-electrode GMAW* [76–80]: In all conventional arc welding processes, the same current flows through the electrode and work-piece. The ratio of the heats distributed on them is only determined by the ratio of the voltage drops. In benchmark GMAW, the power imposed by the arc on the wire to melt the wire is $IV_{\text{anode}}$ and the power directly imposed by the arc on the work-piece is $IV_{\text{cathode}}$. The voltage drops $V_{\text{anode}}$ and $V_{\text{cathode}}$ are materials dependent constants and for steel $V_{\text{cathode}} \approx 2V_{\text{anode}}$ [8,69]. Because the current is the same, their power ratio is not changeable.

The principle of the bypass GMAW can be explained using the non-consumable double-electrode GMAW shown in Fig. 16 where a second torch, referred to as bypass torch, is added. It holds a tungsten electrode and places the tip of the electrode to the vicinity of the main arc established between the wire and work-piece. The added bypass electrode is in the atmosphere of the arc plasma (main arc body) such that the path between it and wire is conductive. As such, when another power source is added as the second/bypass power source that is connected to the wire and bypass torch/electrode as shown in the figure, another loop is formed from the second/bypass power source (positive terminal), to the wire, to the bypass/second electrode and to the bypass/second power source (negative terminal). This second loop is parallel with the main loop that starts from the main power source (positive terminal), to the wire, to the work-piece, and to the main power source (negative terminal) and is referred to as the main loop in the figure. It has been shown that, when the wire speed is given, $I_2$ can be increased to reduce $I_1$ to reduce the heat input.

The bypass GMAW has been widely studied in welding [81–85] and additive manufacturing (AM) [86–88]. The bypass electrode can also be a continuously fed wire and the number of the bypass electrodes/wires/loops can be more than one [89–93]. In all cases, desirable spray transfer is much easily obtained and guaranteed at low base metal currents and the process is thus suitable also sheet metal welding that often requires short-circuiting transfer based processes which are not always preferred due to the lower productivity [94]. Efforts have been made to provide robust controls to assure

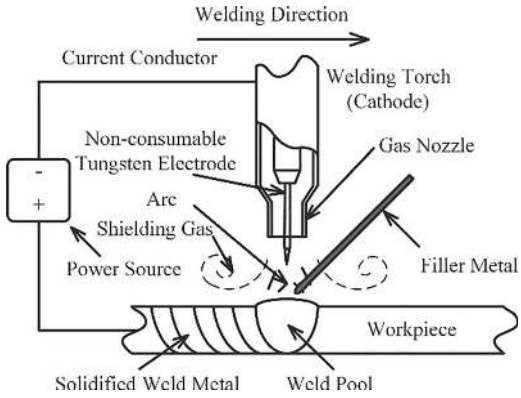


**Fig. 17 Cold-wire GTAW**

process stability [95–97] and desired separate controls of the heat input and wire melting speed.

Increased complexity is the major drawback of the DE-GMAW process. Indeed, the complexity due to increased number of torches that hold the bypass electrode/wire reduces the acceptance to more industrial applications.

*Other GMAW based methods*: There are other process innovations to improve the GMAW as a filling process. One method is the ice GMAW [98] that adds cold wire directly into the weld pool. Additional wire is thus added without increasing the heat input into the work-piece. Another method is the controlled short-circuit processes. When the wire is in short circuiting with the work-piece, the arc extinguishes such that the resistive heat is the only energy in the process. Since the resistive heat is proportional to the resistance and the resistance increases as the current passing area reduces, the resistive heat is almost all applied on the wire rather than on the work-piece. As such, the heat melting the wire is increased without an increase of the heat directly imposed on the work-piece. The challenge is that spatters are easily generated when the arc is re-ignited periodically. Effective technologies have been developed and commercialized to control the re-ignition of the arc to reduce or eliminate the production of spatters. Surface tension control [99–101] and cold metal transfer [102,103] are among these successful ones.

*GTAW based filling process*: GTAW is typically required for critical applications, although it is generally considered much slower than GMAW. This is because the heat in GTAW can be precisely controlled. In GMAW, the wire speed is set and the wire is fed at a given speed. To maintain the process to be stable, the current is continuously adjusted such that the wire feeding and melting are balanced. The arc and heat supplied, as well as their distribution, are subject to changes. In GTAW, the electrode is not melted and it is easy to maintain a constant distance from the work-piece. The current will be controlled at the desired level rather than be dictated to maintain the process stability. As such, many critical applications require GTAW especially in nuclear applications despite the relatively large thickness.

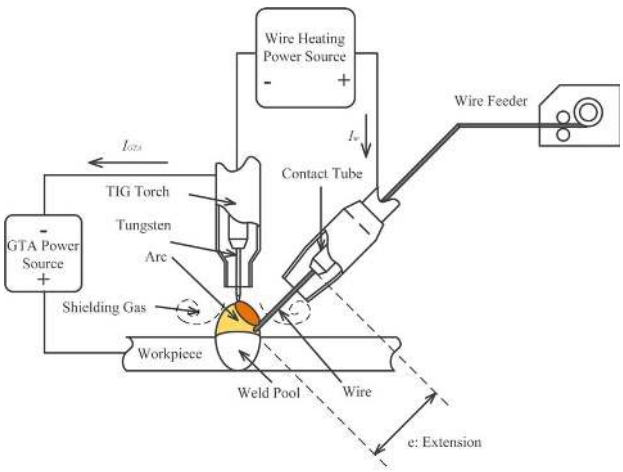


**Fig. 18 Hot-wire GTAW**

Since GTAW is incapable of penetrating a great thickness, typically limited to 3 mm only, groove has be made and be filled also using GTAW by adding filler. The benchmark GTAW filling process is GTAW with cold wire as shown in Fig. 17. In this process, the base metals are melted by the anode heat and cold wire/rod is added into the weld pool and melted by absorbing the heat from the hot liquid of the weld pool.

Hot-wire GTAW [104] is an improved process (Fig. 18) where the wire and work-piece are separately connected to the two terminals of an added power sources in series. The current flows from the wire to the work-piece and then returns back to the added power source. Because of the small diameter and the use of relatively high wire current, the wire can be heated by the resistive heat to an elevated temperature when it enters the weld pool. The heat needed to absorb from the weld pool to melt it is reduced. The wire can thus be added at a faster speed. Due to the reduction in the need for heat absorbed from the weld pool, the weld pool can be reduced to add the same amount of wire.

## 4 Numerical Analysis of Fluid Dynamics

The pre-design results in a welding problem that uses a selected process to make welds on a designed joint (Fig. 3). To design the welding procedure/welding parameters (design in Fig. 3), advanced welding manufacturing optimizes a defined cost function. This requires using predictive models to predict the outcome generated by welding parameters. Since optimization has been well developed, for the design related issues this paper will focus on the predictive models. Due to the complexity of the problem, these predictive models will be numerical models. This section will be devoted to numerical models for fluid dynamics for the weld pool and Sec. 5 will be on the structural analysis results.

**4.1 Introduction.** For fusion welding, the key physical phenomena include heat transfer, fluid flow, electromagnetics when an arc is used, phase transformations, and stress and distortion. For solid-state welding (e.g., friction stir welding), the main phenomena include stress and deformation, heat transfer, and phase transformations (particularly dynamic recrystallization). Physics-based models of welding processes and materials are based on the numerical solution to mathematical equations (typically partial differential equations) that govern those physical phenomena considered.

Weld modeling is inherently complex due to a variety of factors such as high nonlinearity, broad spectrum of spatial and temporal scales involved, and abrupt change in material constitutive behavior from solid to liquid due to melting and vice versa due to solidification. Due to such complexity, a comprehensive model of welding process that takes into account all the key physical phenomena does not currently exist in the literature. The literature models can be approximately divided into two main categories based on the treatment of solid and liquid materials. The first category, treating the material as viscous fluid, is widely used to model weld pool dynamics in arc, laser, hybrid laser-arc, and electron beam welding as well as friction stir welding. On the other hand, the second category treats the material as solid to model the formation of residual stresses and distortion. For ease of reference, the first and second categories are termed as fluid analysis and structure analysis, respectively. The fluid analysis is critically assessed in this section and the structure analysis is reviewed in Sec. 5.

The fluid analysis has been traditionally focused on understanding the weld pool dynamics. Over the past four decades, the weld pool analysis has evolved from simple 2D simulations [105] to

sophisticated 3D simulations involving droplet transfer [106,107]. Perhaps not surprisingly, the weld pool analysis has been rapidly extended to simulate AM processes such as wire arc additive manufacturing, laser-directed energy deposition, and laser-powder bed fusion as these AM processes share many of the same physical phenomena as the fusion welding processes [108,109]. The weld pool models input material properties and welding parameter to calculate the temperature distribution, molten pool geometry, and liquid metal flow field inside the pool. In addition to the weld pool simulation, the fluid analysis has also been applied to model the heat transfer and material flow during friction stir welding [59].

It is noted that in the literature of weld mechanics (i.e., the second category of structure analysis), it is a common practice to calculate the spatial and temporal temperature profiles using a heat conduction simulation without direct consideration of molten metal flow [110]. The temperature profiles (or thermal cycles) are then used as thermal loads in the weld stress and distortion simulation. These heat conduction models generally rely on "artificial" heat flux distributions (e.g., double-ellipsoid distribution in Sec. 5.2) to fit some experimental data (e.g., nugget dimensions). Moreover, the calculated temperature profiles by solving heat conduction only can be inaccurate. For example, Svensson et al. found the heat conduction equation to be inadequate in representing experimental cooling curves [111]. Arrizubieta et al. found that the heat conduction simulation significantly overestimated the transient temperature distribution and resulted in less accurate prediction of molten pool geometry compared with the heat transfer and fluid flow simulation [112].

In this section, we will briefly review the current status of fluid analysis for welding processes including fusion welding and friction stir welding. First, the theoretical background is presented with a focus on the boundary conditions and material properties. Second, representative results of fluid analysis in the literature are highlighted. Lastly, the major research gaps and needs are discussed.

**4.2 Mathematical Formulations.** The fluid analysis is essentially based on the numerical solution of governing conservation equations for mass continuity, momentum conservation, and energy conservation. These equations are well documented in the literature [113] and are thus not repeated here. For illustration of the various solution variables (or degrees of freedom), the governing equation of energy conservation is given as

$$\frac{\partial h}{\partial t} + (\mathbf{v} \cdot \nabla)h = \frac{1}{\rho}(\nabla \cdot \lambda \nabla T) \tag{3}$$

where $h$ is the enthalpy, $t$ is the time, $\mathbf{v}$ is the velocity of molten metal, $\nabla$ is the vector differential operator, $T$ is the temperature, $\rho$ is the density, and $\lambda$ is the thermal conductivity. In this equation, the classic enthalpy-porosity method is used to capture the position of solid/liquid (S/L) interface during melting and solidification. Numerical solution of these governing conservation equations with appropriate boundary conditions and material properties results in the temperature ($T$) and fluid flow ($\mathbf{v}$) fields.

*Quasi-steady-State versus transient Simulation*: Solution to the governing conservation equations such as Eq. (3) can be done either in a global coordinate system attached to the stationary workpiece or in a local coordinate system attached to the moving heat source (arc, laser, or electron beam). The latter, first used in the Rosenthal solutions of heat conduction equation to calculate the quasi-steady-state temperature distribution during welding, has been utilized by several highly efficient weld pool models [106]. However, these quasi-steady-state weld pool models cannot consider the weld start and stop. On the other hand, transient weld pool models readily consider the weld start, heat source traveling, and weld stop albeit at the expense of high computational time [114].

*Weld pool surface*: In some special cases such as autogenous gas tungsten arc welding, the weld pool surface can remain flat [113]. The weld pool surface location is thus known beforehand and there is no need to track the pool surface position. However, in general, the pool surface is highly curved due to a variety of factors such as arc pressure, surface tension, droplet transfer, and recoil pressure from vaporization. In such conditions, the pool surface position is unknown beforehand and must be directly determined in the simulation.

There are two groups of numerical methods for determining the position of weld pool surface which is also known a free surface. The first group, called interface capturing, is based on minimization of the total surface energy in a static condition and it is usually used in conjunction with the aforementioned quasi-steady-state weld pool simulation [106]. In addition to being computationally efficient, the first group uses boundary fitted grid that allows an accurate application of boundary conditions at the weld pool surface. However, it is difficult to consider the breakup and coalescence of molten metal using this group of methods. The second group, interface tracking, uses fixed grids to track the weld pool surface position. The most widely used method in the second group is the volume-of-fluid (VOF) method [115] that solves an additional conservation equation of fluid fraction, as shown below:

$$\frac{\partial F}{\partial t} + \nabla \cdot (\mathbf{v}F) = 0 \tag{4}$$

where $F$ is the fluid volume fraction. The fluid volume fractions of neighboring cells are used to construct the surface position using algorithms such as the piecewise linear interface calculation [115]. As the surface position is not precisely given, very fine grids are necessary to ensure numerical accuracy when applying the boundary conditions.

*Boundary conditions*: For solution of the velocity field, a key boundary condition is the shear stress tangential to the weld pool surface due to surface tension gradient, also known as the Marangoni shear stress. The surface tension of molten metal depends on temperature and composition especially with respect to surface active elements such as sulfur (see A-TIG in Sec. 3). Currently, the most widely used equations for surface tension are those developed by Sahoo et al. [116]. To illustrate the general form of these equations, the surface tension as a function of temperature and sulfur concentration in the molten iron (Fe) is given as

$$\frac{\partial \gamma}{\partial T} = A - R\Gamma \ln(1 + Ka_S) - \frac{Ka_i}{(1 + Ka_S)} \frac{\Gamma(\Delta H^o - \Delta \overline{H}_S^M)}{T} \tag{5}$$

where $\gamma$ is the surface tension, $R$ is the universal gas constant, $a_S$ is the activity of sulfur, and $A$, $\Gamma$, $K$, $\Delta H^o$, and $\Delta \overline{H}_S^M$ are constants for the Fe-S system. Strictly speaking, this equation is only valid for molten iron although it has been used to calculate the surface tension of molten steels and stainless steels due to the lack of data for those alloy systems.

For solution of energy conservation equation, the most important boundary condition is the heat input from the heat source, which is commonly prescribed as a spatial function of heat flux (e.g., Gaussian distribution). The use of such boundary condition greatly simplifies the treatment of the interaction between heat source and weld pool. Specifically, the arc plasma flow and heat transfer does not need treated directly in the weld pool model. While this approach works reasonably well for laser heat input, it may require significant experimental calibration for arc heat input. Research is ongoing to integrate arc and weld pool models together where the heat flux from the arc does not need prescribed beforehand [107].

*Keyhole*: The shape of the keyhole within the weld pool can be readily calculated by considering the molten metal free surface subjected to a pressure. For laser and electron beam welding, such surface pressure comes from the recoil pressure due to vaporization of alloying elements. For PAW, the pressure results from the plasma jet. An additional complexity arises due to the enhanced transfer of laser beam energy to the liquid metal due to multiple reflections and absorptions on the keyhole wall. For instance, Simonds et al. experimentally measured the laser absorptance for laser spot welding of 316 L stainless steel [117]. The efficiency value was found to be around 30% for conduction mode and the value increased to 90%

for keyhole mode. To simulate the multiple reflections and absorptions of laser beam on the keyhole wall, a ray tracing method was typically used, for example, see Bayat et al. [118].

*Material properties*: The basic properties needed for weld pool analysis are thermal conductivity, specific heat, and density as a function of temperature for molten metal and solid metal. Additionally, surface tension and viscosity are two other important material properties for molten metal. While such properties are available for some commonly used alloys (e.g., austenitic stainless steel 316 and nickel alloy 718), the material properties are typically not available as a function of composition. Hence, for weld pool simulation involving different metals (e.g., joining of stainless steel to mild steel in Fig. 1), interpolation may be needed to obtain the properties of weld metal mixed with stainless steel and mild steel.

Another complexity is the role of turbulence which can greatly enhance mixing inside the weld pool. A comprehensive understanding of the extent of turbulence in weld pool is still being established. A common practice is to treat the molten metal flow as laminar with thermal conductivity and viscosity enhanced to account the effect of turbulence [106].

In the fluid-based models of friction stir welding, the work-piece material is treated as a non-Newtonian viscous fluid. The material viscosity is defined as $\mu = (\sigma_f/\bar{\dot{\varepsilon}})$, where $\sigma_f$ is the flow stress and $\bar{\dot{\varepsilon}}$ is the effective strain rate that is determined as $\bar{\dot{\varepsilon}} = \sqrt{(2/3)\dot{\varepsilon}\cdot\dot{\varepsilon}}$ with $\dot{\varepsilon}$ being the strain rate tensor. The Zener–Hollomon relationship is commonly used to describe the constitutive behavior of the material [125]

$$\dot{\varepsilon}\exp\left(\frac{Q}{RT}\right) = A[\sinh(\alpha\sigma)]^n \tag{6}$$

where $Q$, $A$, $\alpha$, and $n$ are the material parameters, $R$ is the universal gas constant, and $T$ is the temperature.

**4.3 Representative Results for Fusion Welding.** Figure 19(*a*) shows the calculated temperature and velocity fields during gas metal arc welding of a fillet weld [106]. For clarity, only half of the work-piece is shown, since the weld is symmetric about the central longitudinal plane containing the welding direction. The simulation was performed using a quasi-steady-state weld pool model with boundary fitted grids, as illustrated by the curvilinear grid lines in the figure. The "static" surface profile was calculated by minimizing the total surface energy involving those from surface tension, gravity, and arc pressure. The arc plasma was not simulated and instead the arc heat input was prescribed as a Gaussian heat flux distribution. In Fig. 19(*a*), the temperature field is represented by the contours and the velocity field is depicted by the arrows. On the pool surface, the liquid metal flew from the center to the periphery driven by the Marangoni shear stress. Inside the pool and directly underneath the arc, the electromagnetic (Lorentz) force due to current flow drove the liquid metal downward.

Figure 19(*b*) shows the fluid flow field and temperature distribution on a transverse cross section during laser-GMA hybrid welding process of lap joint [114]. Similar to the model shown in Fig. 19(*a*), the arc plasma was not directly simulated, and instead the model prescribed an asymmetric distribution of arc heat and a cylindrical volumetric distribution of laser heat. Unlike the model in the previous figure, this transient simulation used VOF method to track the weld pool surface position. Droplets were introduced into the computational domain through the use of a velocity inlet boundary condition where the droplet temperature and velocity were defined. Figure 19(*b*) shows the molten metal distributed on both sides of the pool connected by a thin "bridge" in the center of the pool prior to the impingement of a droplet.

Figures 19(*c*) and 19(*d*) depict the calculated temperature and velocity fields, respectively, during laser-gas tungsten arc hybrid welding [107]. These results were obtained using a so-called unified model of arc plasma and weld pool. Due to the complexity, heat transfer and fluid flow within the work-piece were modeled separately from that outside of the work-piece and they were coupled through boundary conditions. The free surface was tracked by the level set method. These figures show the formation of keyhole and the arc plasma flow.

For laser welding, an early foundational work is the model developed by Kaplan to calculate the quasi-steady-state keyhole profile [120]. Nowadays, the transient evolution of keyhole and weld pool profiles can be readily computed by simulating free surface flow. For instance, Zhang et al. developed a transient, 3D model to simulate the dynamics of keyhole and molten pool during full penetration laser welding [119]. The free surface profile was captured using the VOF method and the multiple reflections and absorptions of the laser beam on the keyhole wall were calculated using a ray tracing algorithm. Figures 20(*a*)–20(*h*) shows a series of snapshots of the transient temperature fields and flow velocities on the central longitudinal cross section, where the laser traveled from left to the right. The open channel (or deep cavity) is the keyhole. Due to a fast traveling laser, the molten pool was very thin ahead of the keyhole and it had an elongated tail behind the keyhole.

The weld pool model can also readily simulate the formation of porosity due to keyhole collapse, which is a common defect in the deep penetration keyhole mode welding. Figure 21 shows the calculated flow patterns on a transverse cross section during hybrid laser arc welding (HLAW) [121]. The model was developed based on flow-3D, a commercial computational fluid dynamics (CFD) code. The existence of keyhole greatly enhances the heat transfer through the thickness direction, resulting in the deep penetration shown in Fig. 21(*c*). The keyhole is unstable and a trapped bubble is observed near the bottom of the pool due to the keyhole collapse from the middle height, as shown in Fig. 21(*b*).

In addition to predicting the temperature and velocity fields, the weld pool models are commonly integrated with other models to predict the microstructure and composition of the weld metal, residual stress, and distortion. Review of those simulations is provided in Sec. 5.

**4.4 Representative Results for Fluid-Based Analysis of Friction Stir Welding.** Friction stir welding, a solid-state joining process, involves material deformation and extrusion around the tool pin. Hence, it is appropriate to model the FSW process using the solid mechanics approach with elastic-plastic constitutive behavior. The solid mechanics models are typically prone to numerical divergence issues caused by the complex contact conditions as well as the severe plastic deformation. To improve convergence, the tool pin is commonly simplified as a smooth cylinder without the consideration of the tool thread feature [122].

Another group of FSW process models are the fluid-based models that treat the work-piece material as non-Newtonian viscous fluid. When compared with the solid mechanics models, the fluid-based models are more robust and efficient computationally and can more readily consider the tool thread feature. One of the early fluid-based models can be traced back to the quasi-steady-state model developed by Ulysse [123] which used a smooth pin without any thread and imposed a downward velocity on the pin surface to account for the effect of the thread on material flow. Recent fluid-based models have incorporated the threaded pin for both quasi-steady-state and transient simulations, as discussed in the following.

Colegrove and Shercliff developed a 3D quasi-steady-state model taking into account the complex tool geometry based on FLUENT, a commercial computational fluid dynamics code [124]. The calculated temperature and material flow fields around the threaded pin during FSW of an aluminum alloy are shown in Fig. 22(*a*). Yu et al. applied a dynamic mesh method, which combined both Lagrangian and Eulerian formulations, to capture the material flow induced by the rotational and translational motions of the threaded tool pin [125]. The flow pattern around the pin during friction stir processing of a magnesium alloy is shown in Fig. 22(*b*). The results calculated from the fluid-based models can be utilized further to assess other characteristics of FSW such as tool durability [126]. Figure 22(*c*) shows the thermal cycle

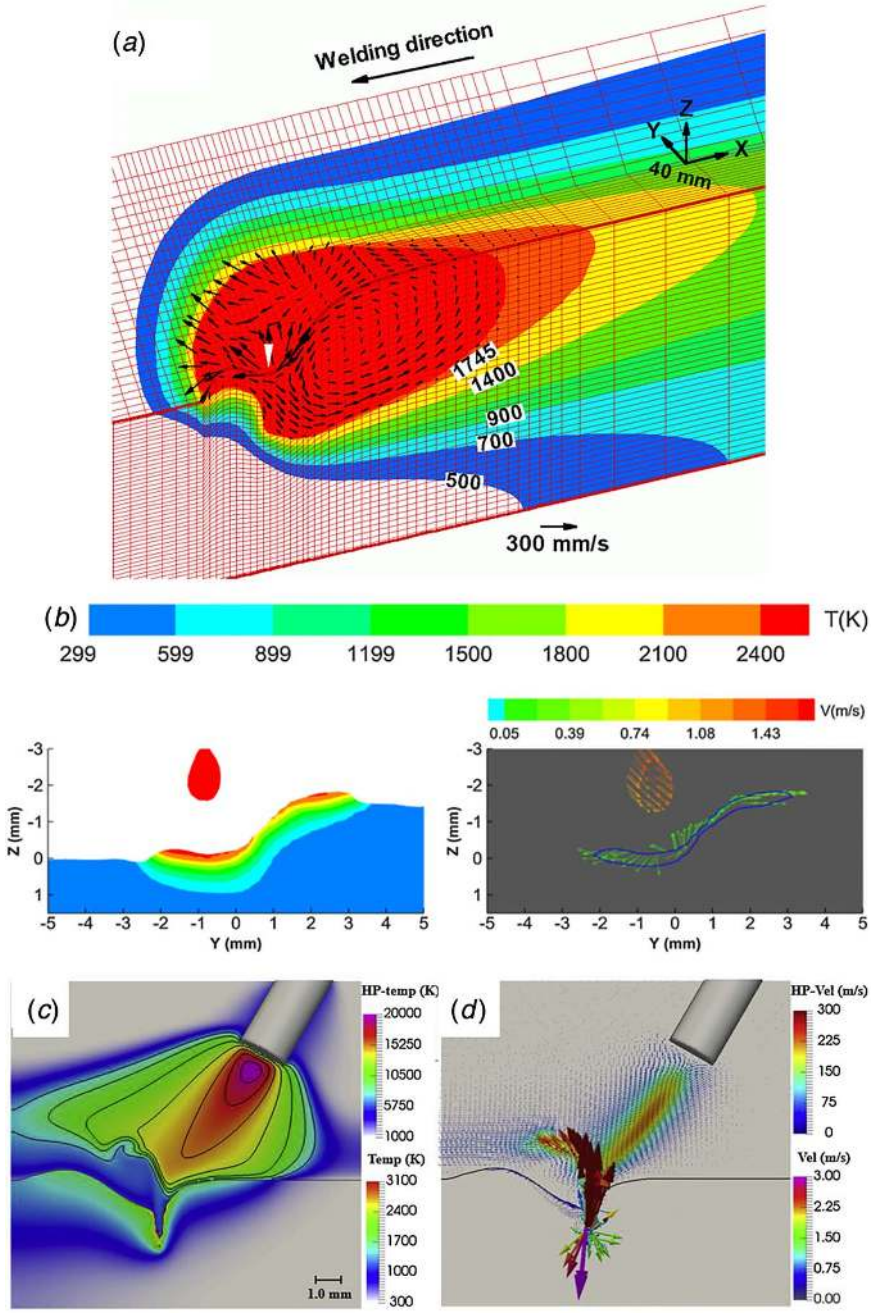


**Fig. 19 Representative results of computed temperature and velocity fields computed using (*a*) quasi-steady-state model [106] (Reprinted with permission from AIP Publishing © 2004), (*b*) transient model with volume of fluid method for free surface tracking (Reprinted with permission from Elsevier © 2017) [114], and (*c*) and (*d*) integrated model of arc plasma and weld pool [107] (Reprinted with permission from Elsevier © 2019)**

calculated for FSW of a mild steel. Such temperature information along with the shear stress on the tool pin was used to construct a tool durability index, defined as the ratio of the shear strength of the tool material and the maximum shear stress on the tool pin. Figure 22(*d*) shows the computed tool durability index as a function of tool rotation speed and should diameter. Such durability map can help guide the process optimization to ensure the tool durability.

**4.5 Summary of Status and Gaps.** The results from the fluid analysis presented previously show the utility of these models for understanding the temperature field and weld pool geometry for fusion welding and the material flow for friction stir welding. When integrated with other tools, the simulations can be used to predict a wide range of characteristics such as the weld metal composition due to dilution and vaporization, formation of defects (e.g., keyhole porosity), solidification grain size and texture, microstructure in the weld metal and heat-affected zone, and thermal stress and deformation. Therefore, the weld pool models are essential to the prediction of welding results in nominal conditions to decide how to use the tools toward an optimized design.

While there is a compelling need for the use of the weld pool models, the current use tends to be limited to academia. The following research gaps need addressed to enable the greater use of the weld pool models by industry practitioners as well as researchers.

- An improved understanding of the interaction between heat source and work-piece is needed. For instance, arc efficiency

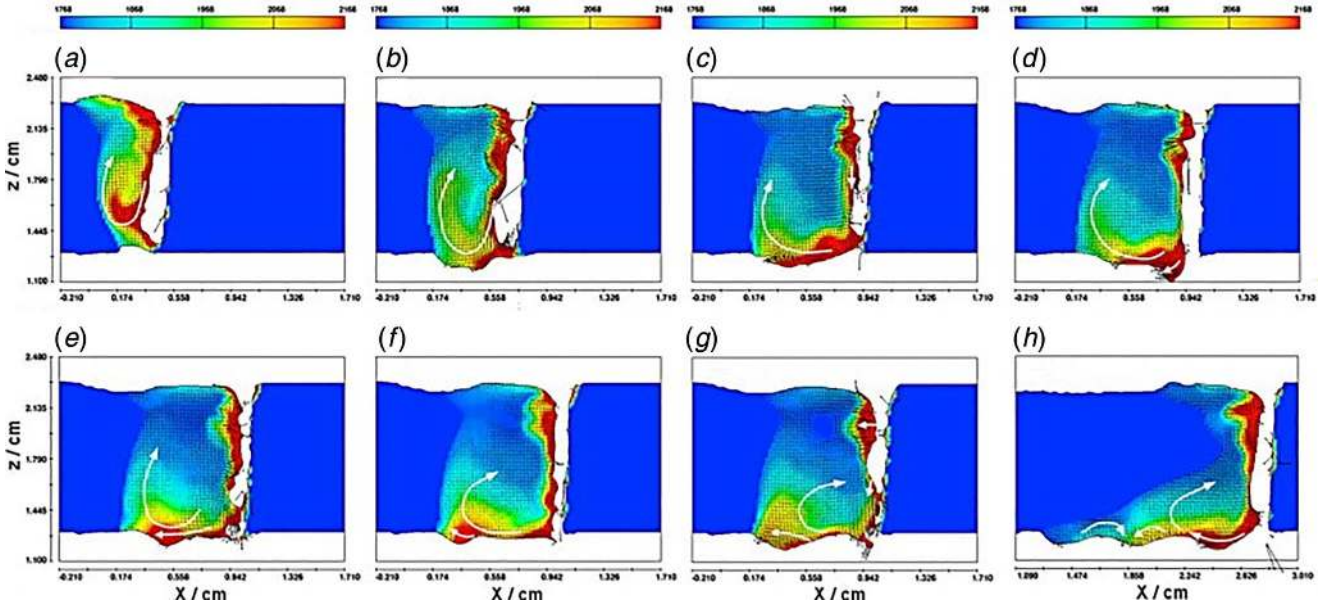


**Fig. 20 Calculated temperature and fluid flow fields during full penetration laser welding [119]: (*a*) $t = 0.295$ s, (*b*) $t = 0.45$ s, (*c*) $t = 0.57$ s, (*d*) $t = 0.615$ s, (*e*) $t = 0.625$ s, (*f*) $t = 0.63$ s, (*g*) $t = 0.64$ s, and (*h*) $t = 1.685$ s**

or laser absorptivity is an important parameter which value is often unavailable for the specific welding parameters and work-piece material. Fully integrating arc plasma model with the weld pool model, a challenging task, has the potential to address this issue. Experimental measurements should also be explored to generate such data.

- The material properties of molten metal such as surface tension and viscosity are needed as a function of chemical composition and temperature. Such properties can be essential to accurate prediction of the weld pool geometry in high-valued welding processes such as temper bead welding repair of reactor pressure vessel structures.
- Efficient ways to scale the weld pool model up to multi-pass and multilayer situation are needed. This is particularly important for wire arc additive manufacturing.

## 5 Numerical Analysis of Structures

When steel structures are constructed by welding, deformations and welding residual stresses could occur as a result of the localized high heat input and subsequent rapid cooling. The residual stresses and deformation can have an important influence upon welded structure performance such as strength, fatigue and cracking during service [127–129].

Numerical methods have been developed and used to predict and control weld residual stress and distortion for industrial uses [130,131]. The most accurate method, transient moving-arc thermo-elastic-plastic method, was developed to permit simulating the entire physical process of welding which includes metal deposition, melting/re-melting, larger deformation, strain hardening, and phase transformation [132–134]. Simplified methods such as lump-pass modeling method [135], traveling temperature function method [136,137], inherent-strain method [138–141], shrinkage force method, and local-to-global assemble method [142–144] were developed to provide a quick solution for predicting welding-induced distortions.

This section focuses on discussing the transient moving-arc thermo-elastic-plastic method and briefly introduces how to apply this modeling method to solve industrial problems related to weld residual stress and distortion. Figure 23 shows a typical process flow of simulating welding processes including fusion welding and solid-state welding. There are four major steps in the process flow: mesh generation, thermal analysis, microstructural analysis, thermomechanical analysis [145], which will be discussed in detail as follows.

As shown in Fig. 23, a welding simulation starts by collecting information which includes the geometry of welded structures, weld groove, weld macrographs, welding parameters, preheating temperature, interpass temperature, thermal-physical, and mechanical properties of base materials and filler materials as a function of temperature, and welding fixture and tooling [146]. The geometry of welded structures with a universal model format such as IGES or step will be imported to a finite element preprocessing software for mesh generation. The weld groove and weld macrographs will be used to create weld mesh. The weld parameters, preheating and interpass temperature, and the thermal-physical properties will be input to the thermal model to predict temperature. The welding fixture, tooling, and the mechanical properties will be converted to numerical boundary conditions and input to the thermomechanical model to predict weld residual stress and distortion.

**5.1 Weld Mesh Generation.** Finite element meshing for welding simulation is special since the weld area needs very fine mesh to capture the large temperature and stress gradient and the area far away from the weld needs to be meshed coarsely to save the computational time. Figure 24 shows a weld mesh for a multipass butt joint which were automatically created based on an input weld groove and a weld macrograph with a python script working with ABAQUS/CAE. Each weld bead was digitized and input to the python script [147].

**5.2 Thermal Model.** An accurate numerical method to predict temperature field during welding is introduced in Sec. 4, numerical analysis of weld pool, which is based on CFD theory. Ideally, the predicted temperature field can be used as thermal loads in the weld stress and distortion simulation. Indeed, Anthony et al. [148] developed an integrated model to simulate arc plasma, filler wire transfer, and weld pool dynamics in a lap-fillet weld geometry to predict weld residual stress and distortion. However, this approach is impractical for a large and complex welded structure due to the complexity of numerical model and computational cost. Currently, CFD for weld pool simulation is limited to a small geometry. Therefore, a thermal model was developed based on heat transfer theory to predict temperature, residual stress, and distortion in which welding heat sources were modeled using

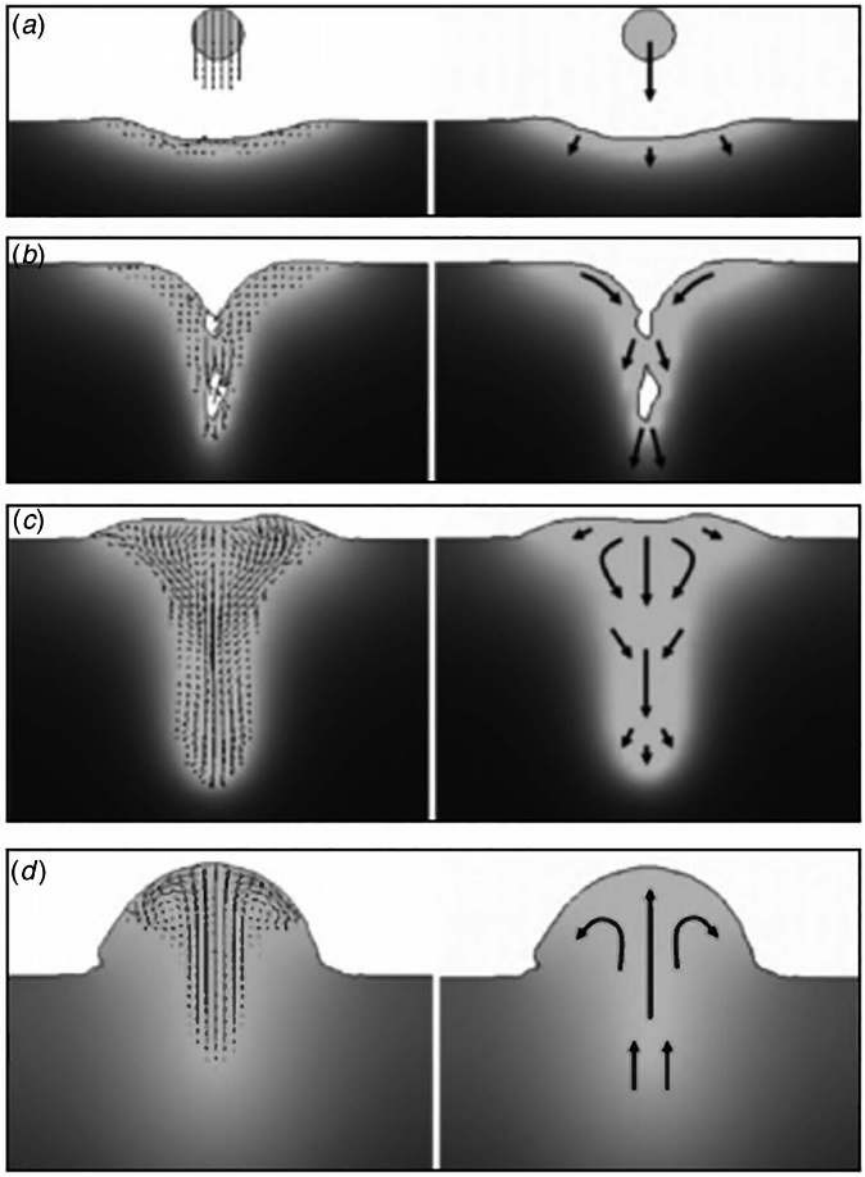


**Fig. 21 Calculated flow patterns illustrating the formation of keyhole porosity on a transverse section at four different welding times during hybrid laser-arc welding: (*a*) 0.84 s, (*b*) 0.95 s, (c) 1.03 s, and (*d*) 1.9 s [121]**

"artificial" heat flux distributions such as Goldak double ellipsoidal heat source model [149].

The three-dimensional transient heat transfer model is conducted to simulate arc welding process with the governing equation given as follows [147]:

$$\frac{\partial}{\partial x}\left(\frac{\partial T}{\partial x}\right)+\frac{\partial}{\partial y}\left(\frac{\partial T}{\partial y}\right)+\frac{\partial}{\partial z}\left(\frac{\partial T}{\partial z}\right)+q=\rho c\frac{\partial T}{\partial t} \tag{7}$$

where $q$ is the rate of internal volumetric heat generation, $T$ is temperature, $\lambda$ is thermal conductivity, $c$ is the specific heating capacity, $\rho$ is the material density, and $t$ is the time, respectively. All thermal-physical property ($\lambda$, $c$, $\rho$) should be input as a function of temperature.

*Arc welding heat source model*: Goldak et al.'s double ellipsoidal heat source model [149] has been widely used to simulate arc moving for fusion welding processes including GMAW, GTAW, submerged arc welding (SAW), and flux-cored arc welding (FCAW). In this model, heat flux at a point and a time is calculated as

$$q(x,y,z,t)=f\frac{6\sqrt{3}Q\eta}{abc\pi\sqrt{\pi}}e^{\frac{-3x^2}{a^2}}e^{\frac{-3y^2}{b^2}}e^{\frac{-3[z+vt]^2}{c^2}}$$
$$Q=IU \tag{8}$$

where $x$, $y$, and $z$ are the local coordinates, $a$, $b$, $c$ are the semi-axes of the ellipsoid as shown in Fig. 25, $f$ is a factor, $\eta$ is heat efficiency, $Q$ is the power, and $\nu$ is the traveling speed. Welding parameters and weld bead profiles can be input to this model to calculate heat flux for heat transfer analysis to predict temperature history. The approximated arc efficiency used in the model is 0.85 for GMAW, 0.65 for GTAW and FCAW, and 0.95 for SAW. Validation tests have been conducted to prove the temperature prediction accuracy with this model [149].

As an example, Fig. 26 shows the predicted distributions for a double-sided fillet weld with FCAW [142]. The base material is DH36 steel and the weld size for the fillet weld is 7.7 mm. The three-dimensional (3D) picture shows temperature distributions

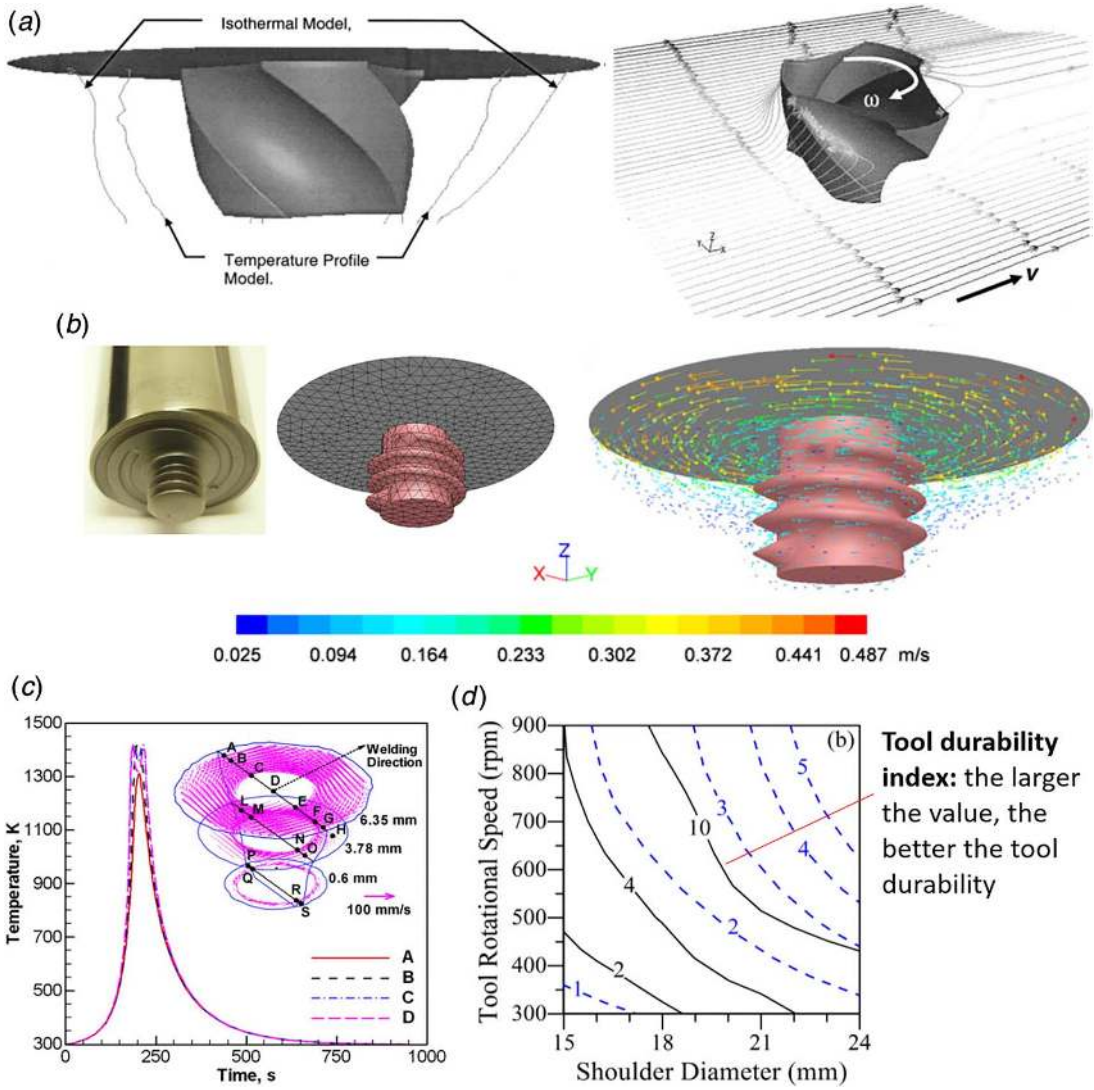


**Fig. 22 (*a*) Calculated temperature and material flow fields around the threaded pin during FSW of an aluminum alloy [124] (Reprinted with permission from Taylor & Francis © 2004), (*b*) flow pattern around the pin during friction stir processing of a magnesium alloy [125] (Reprinted by permission from Springer Nature © 2011), (*c*) thermal cycles, and (*d*) tool durability index for FSW of 1018 steel at two different welding speeds 1.05 mm/s (solid line) and 2.1 mm/s (dashed line) [126]**

during welding arc moving to near the end of a fillet weld. The two-dimensional (2D) pictures show a weld macrograph and a predicted fusion zone. The predicted fusion zone is very close to the macrograph, which proves the thermal model prediction is accurate.

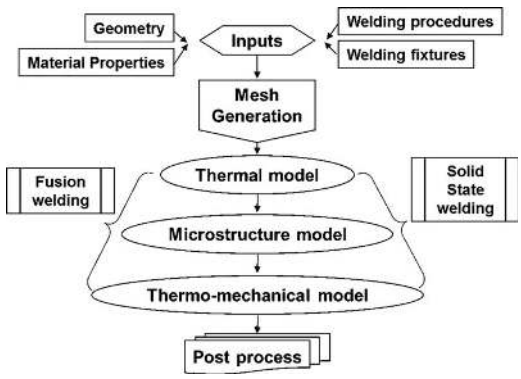


**Fig. 23 Welding simulation process flow**

*Laser welding heat source model*: Laser welding has two heat transfer modes: keyhole mode and conduction mode. For the keyhole laser welding mode, conical heat source model [150], as shown in Eq. (9), could be selected to calculate the volumetric heat flux. Laser is traveling in $z$ direction and $y$ is the plate thickness direction. The parameter $d$ which can be input a value from 0 to 1 controls heat distributions along the plate thickness direction. When $d$ is 0, the heat flux is zero on the plate bottom surface. The heat flux is a trapezoidal shape in the $x$–$y$ plane. When $d$ is 1, the heat flux does not vary along $y$ direction

$$q(x, y, z, t) = \frac{6f\eta Q}{abc\pi(1+d)} e^{-3(x^2/a^2)} \times \left(1 - \frac{(1-d)|y|}{b}\right) e^{-3(((z+vt)^2)/c^2)} \quad (9)$$

where $b$ is the weld penetration or the welded plate thickness.

For the conduction mode laser welding, the surface heat–flux distribution of the moving arc was considered as a Gaussian

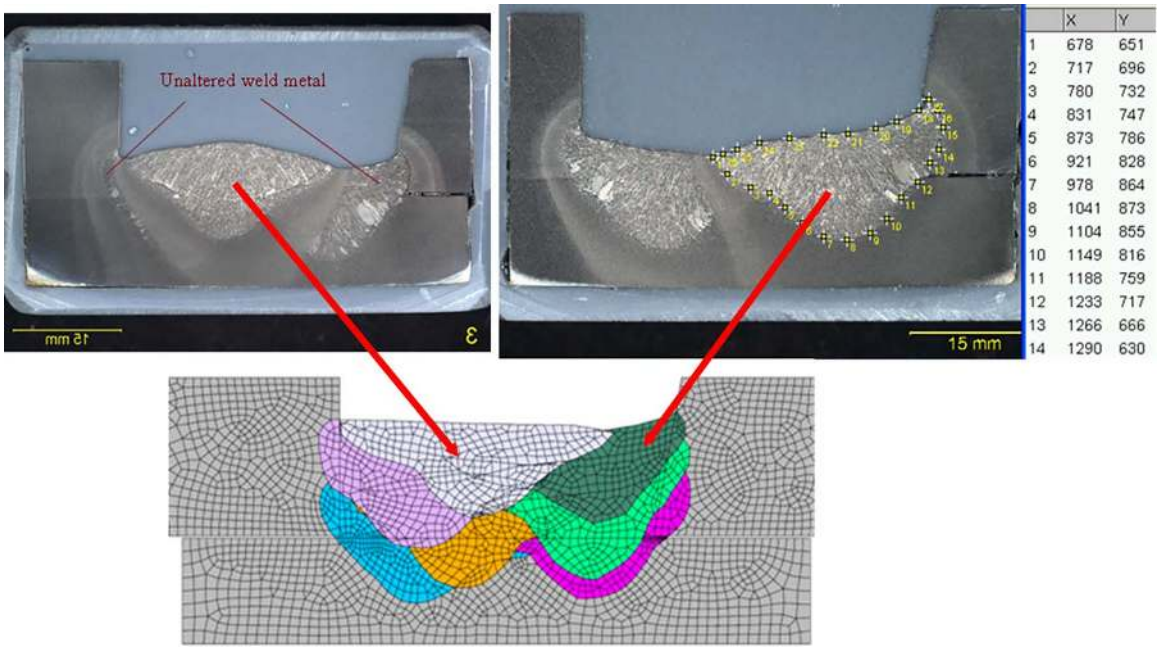


**Fig. 24 Automatic weld generation**

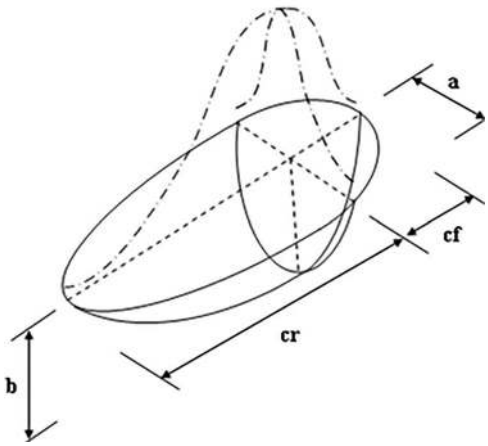


**Fig. 25 Parameters in Goldak's heat source model**

distribution [151] expressed by

$$q_s = \frac{3\eta Q}{\pi r^2} e^{(x^2+y^2+(z+vt)^2/(-r^2/3))} \tag{10}$$

where $r$ is effective radius of the heat source. This heat source model can also be used to calculate heat flux for autogenous GTAW.

*Hybrid laser arc welding heat source model*: For HLAW process, a combined Goldak and conical heat source model could be selected to predict the heat flux in which the Goldak heat source model is used to simulate arc welding and the conical heat source model is used to simulate laser welding [152]. The modified conical heat source model can also be used to model keyhole plasma arc welding [153].

As an example, Fig. 27 shows predicted temperature distributions in a HLAW weld of titanium alloys. The 3D picture show the temperature distribution when the heat sources move to near the end of the plate. Two cross sections were cut to check the fusion zone profile. The fusion zone at the cross section perpendicular to the

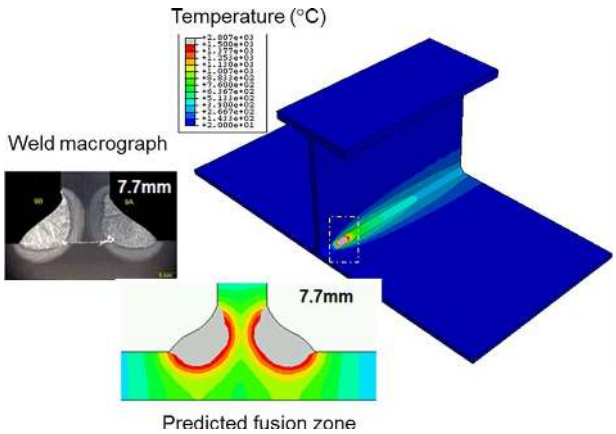


**Fig. 26 Predicted temperature distributions in a fillet weld**

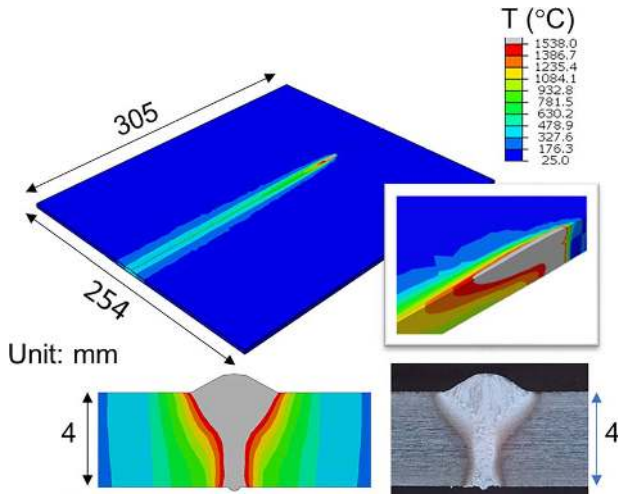


**Fig. 27 Predicted temperature distributions in a HLAW weld**

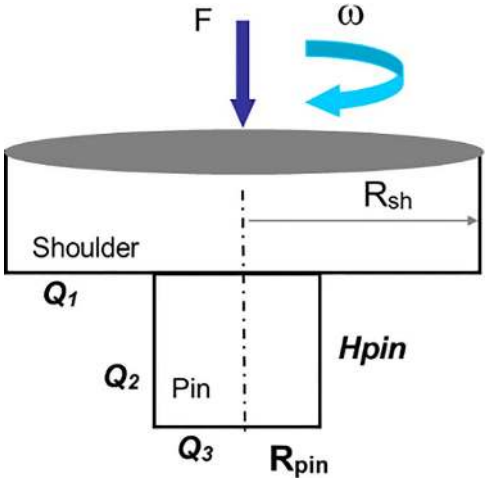


**Fig. 28 An idealized friction stir welding tool**

traveling direction is similar to the weld macrograph, which proves the thermal model is working. The fusion zone at the cross section along the traveling direction shows the typical shape for HLAW in which the top area has a longer fusion area welded with arc welding than the bottom area welded with laser welding.

*Friction stir welding heat source model*: FSW is a solid-state process in which heat is mainly generated from friction and plasticity. Figure 28 shows a FSW tool in which the pin has a cylindrical shape. During welding, the shoulder and pin will contact with weldment. Heat will be generated by friction on the contact surfaces. The total heat ($Q_t$) including friction induced heat from all three surfaces (shoulder surface, pin side surface, and pin bottom surface) and heat generation from plastic energy dissipation can be expressed as [154]

$$Q_t = \frac{2}{3}\pi\tau\omega(R_{sh}^3 + R_{pin}^2 H_{pin}) + \tau\dot{\varepsilon}^{pl} \tag{11}$$

where $\dot{\varepsilon}^{pl}$ is the plastic strain increment.

Surface heat flux calculated Eq. (12) is applied on the shoulder surface and body flux calculated with Eq. (13) is applied in the pin volume. Note that heat generation from plasticity is not explicitly included in Eqs. (12) and (13). Its effect is considered in determining the heating efficiency ($\eta$)

$$q_s(r, T) = \frac{3}{2\pi}0.75\eta Q_t \frac{r}{R_{sh}^3 - R_{pin}^3} \tag{12}$$

$$q_b(r, T) = \frac{0.25\eta Q_t}{\pi R_{pin}^2 H_{pin}} \tag{13}$$

As an example, Fig. 29 shows the predicted temperature distributions for an FSW butt joint of steel [154]. The left-hand picture shows the friction stir welding process and the right-hand picture shows the predicted temperature distributions. The maximum temperature is about 1200 °C at which steel becomes soft for tool stirring to form the joint.

*Heat loss*: Heat loss to the air and to the fixture at bottom of the case was considered by simulating heat convection and radiation. The heat loss by convection is calculated as follows:

$$q_c = h(T - T_0) \tag{14}$$

The heat loss by radiation is calculated as follows:

$$q_r = (T^4 - T_0^4) \tag{15}$$

where $T_0$ is the ambient temperature, $\varepsilon$ is the emissivity, and $\sigma$ is the Stefan–Boltzmann constant. The heat convection coefficient is temperature dependent, but it often inputs as constant for simplicity.

**5.3 Microstructural and Hardness Model.** The heat of welding causes changes in the microstructure and mechanical properties in the fusion zone and the HAZ. For steel welds, the resulting microstructure depends upon the chemical composition of the steel and the rate at which the steel is heated and cooled [155]. Ion et al. [156] and Kirkaldy and Venugopalan [157] developed general algorithms to predict the hardness resulted from welding. Kasuya et al. [158] developed a highly accurate prediction formula for the maximum hardness of the HAZ for understanding the properties of welded joint. Yu et al. [159] developed an effective neural network system to predict the HAZ hardness during bead-on-plate welding.

The microstructure model developed by Ashby et al. [156] has been implemented to predict the distribution of each individual phase such as ferrite, bainite, and martensite and the hardness map around the weld area [145]. Martensite is the most important phase in the microstructure distribution since martensitic transformation and the resulting hard and brittle phase can lead to cracking in the weld or HAZ. The degree of hardening in the HAZ is an important consideration determining the weldability of a low carbon and low alloy steel.

The carbon equivalent (CE) is a useful parameter in evaluating the influence of alloying additions on the weldability of the steel. The following equation is an empirical one recommended by the International Institute of Welding for calculating CE [160]:

$$\mathrm{CE} = C + \frac{\mathrm{Mn}}{6} + \frac{\mathrm{Cr} + \mathrm{Mo} + \mathrm{V}}{5} + \frac{\mathrm{Ni} + \mathrm{Cu}}{15} \tag{16}$$

where C is carbon, Mn is manganese, Cr is chromium, Mo is molybdenum, V is vanadium, Ni is Nickel, and Cu is copper. All the

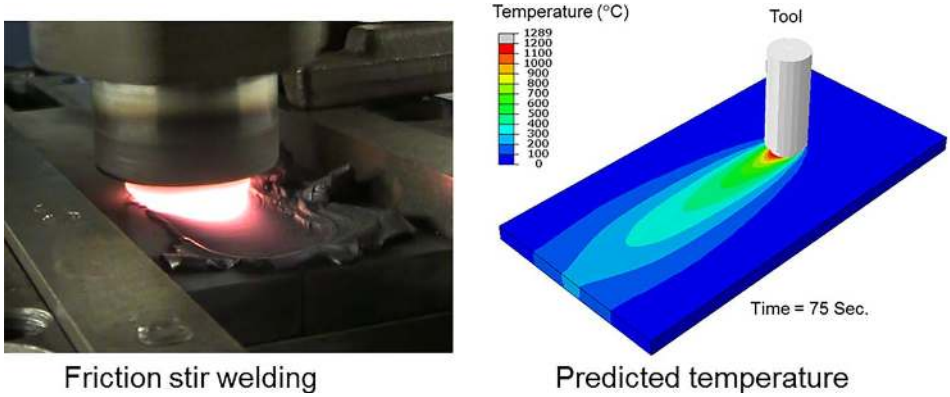


**Fig. 29 Predicted temperature distributions in a FSW weld**

composition is defined in weight percent.

The carbon equivalent can be used to relate to the following critical cooling rates:

$$\log \Delta t^{m}_{1/2} = 8.79\ \mathrm{CE} - 1.52$$
$$\log \Delta t^{b}_{1/2} = 8.84\ \mathrm{CE} - 0.74 \tag{17}$$

where $\Delta t^{m}_{1/2}$ is the critical time that gives a 50% martensite and 50% bainite structure, and $\Delta t^{b}_{1/2}$ is the time that gives a 50% of bainite and 50% ferrite structure. From the critical cooling rate, the final volume fraction of microstructure such as maternsite ($V_m$) can be calculated as the following:

$$V_m = \exp\left\{-0.69\left(\frac{\Delta t}{\Delta t^{m}_{1/2}}\right)^{2}\right\} \tag{18}$$

where $\Delta t$ is the transformation time.

The hardness can be calculated using the following empirical equation

$$H_m = 127 + 949C + 27\mathrm{Si} + 11\mathrm{Mn} + 8\mathrm{Ni} + 16\mathrm{Cr} + 21\log V' \tag{19}$$

where $H_m$ is the hardness of martensite, $V'$ is the cooling rate at 700 °C (°C/hr). The final hardness ($H$) at each point of the weld can be estimated using the rule of mixtures

$$H = \sum H_i V_i \tag{20}$$

where $i$ is a particular phase, and $H_i$ and $V_i$ are the hardness and volume fraction of that particular phase, respectively.

Based on the steel chemistry inputted from the user and the cooling rate calculated from the thermal analysis, Eqs. (17) through (20) predict the final volume fractions and hardness.

As an example, Fig. 30 shows the predicted temperature histories and hardness distributions for a bead-on-plate weld on a steel plate. Thermocouples (TCs) were used to measure temperature histories to validate the thermal model predictions. The line plots show that the predicted temperature histories agree with the experimental measurement. The predicted hardness shows that HAZ had much higher hardness than the weld, which is validated by experimental hardness measurement.

**5.4 Thermomechanical Model.** Fusion welding process includes major physics such as metal deposition, heat transfer, material melting/re-melting, solidification, and phase transformation. During this process, plastic strain is created before of nonuniform heating and cooling. Plastic strain will induce weld residual stress and distortion. It is important to model all the physical phenomena involved in welding process to predict weld residual stress and distortion accurately.

A thermomechanical-metallurgical model for fusion welding is illustrated in Fig. 31 for weld residual stress and distortion prediction. The model inputs are the predicted temperature history from the thermal model and the predicted microstructures from the microstructural model. The boundary conditions of the model are numerical constraints induced by welding fixture and tooling.

*Metal deposition* during fusion welding will be modeled by element death (deactivated) and birth (activated) technique or virtual element detection technique. In the element death–birth technique, weld elements are deactivated before welding and reactivated during welding. This technique often induces numerical convergence issues because of sudden changes of model stiffness matrix. Thus, the virtual element detection technique was developed in which weld elements are assumed to be deposited and assigned a minimal stiffness before welding and then changed to the true properties gradually during welding [161].

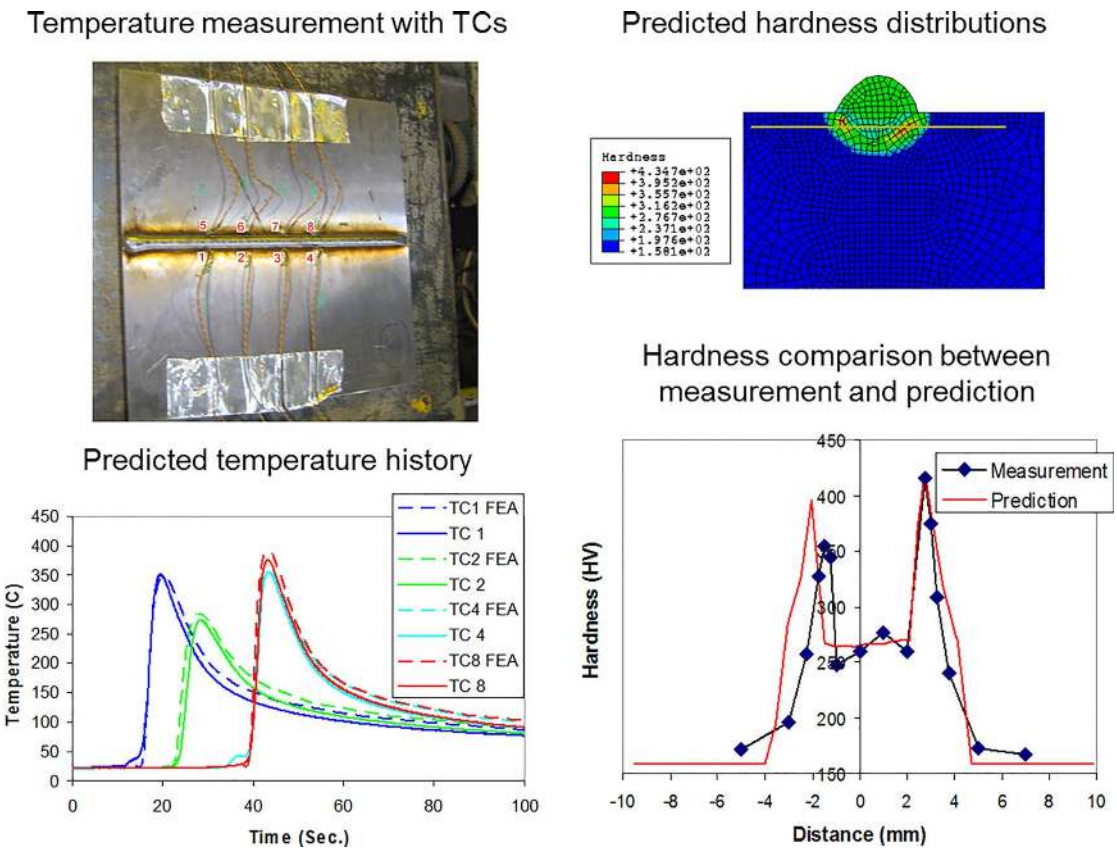


**Fig. 30 Predicted temperature histories and hardness distributions in a bead-on-plate weld**

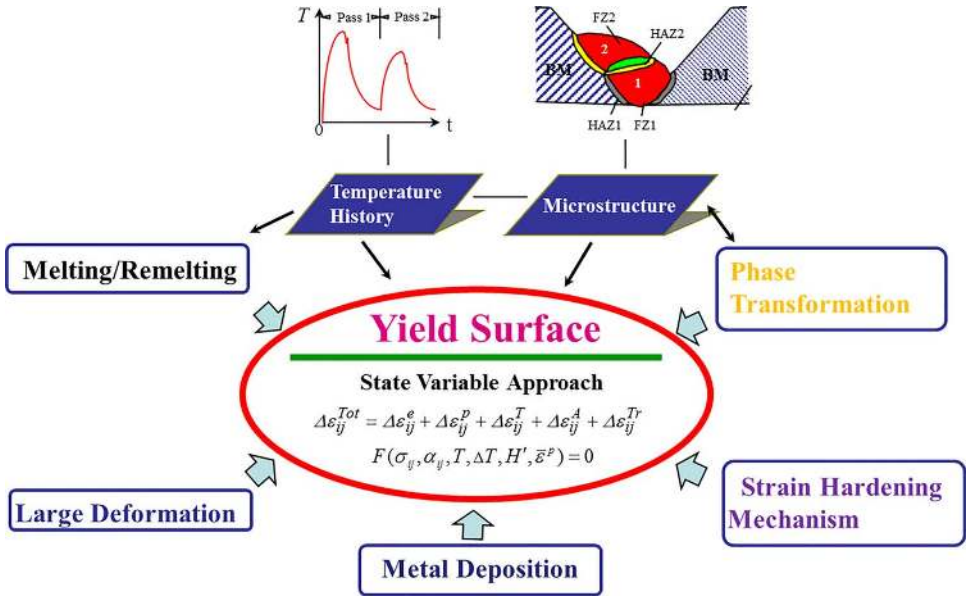


**Fig. 31 A thermomechanical-metallurgical model for fusion welding**

*Large deformation mechanism* is usually selected to predict welding induced distortion by modeling nonlinear geometry effect. If small deformation mechanism is selected, finite element analysis will not update the node coordinates during welding. Selecting large deformation mechanism is very important when a shell-element model is used to predict welding induced distortion. Without selecting large deformation mechanism, the shell-model predicted distortion would not predict distortion magnitudes correctly, especially during predicting buckling distortion for thin-plate structures [162].

*Strain hardening mechanism* models the yield strength increases as a result of repeated heating and cooling thermal cycles in multi-pass welding. There are three types of material hardening mechanisms: isotropic hardening, kinematic hardening, and combined isotropic-kinematic hardening. Mullins and Gunnars [163] modeled a multi-pass pipe welding of 316 stainless steel and found out that the isotropic hardening model gave the best overall agreement with experimental measurements. The combined hardening model gave good agreement for predictions of the hoop stress but tended to underestimate the magnitude of the axial stress. The kinematic hardening model consistently underestimated the magnitude of both the axial and hoop stress. However, this conclusion may not be general because of the limitation of weld residual stress measurement. In general, isotropic hardening could be selected for single-pass welding. For multi-pass welding, weld residual stress could be over predicted with isotropic hardening. A general rule is to use kinematic hardening or combined isotropic-kinematic hardening when the number of weld passes are larger than 3.

*Phase transformation mechanism* models the effect due to the microstructural changes of the material during the welding process. The changes in the microstructure of the material are a function of parameters such as the chemical composition of the material and the thermal cycles of the welding process. The effect of microstructural change will induce volumetric changes during the phase transformation, transformation plasticity, and yield hysteresis due to phase differences in the heating and cooling processes [164].

*Material melting modeling in fusion welding*: Most commercial finite element software were developed based on solid mechanics theory and cannot model material melting. When material is melted, strain and strain go to zero. During solidification, material strength is recovered. Tensile strain appears behind weld pool which induces hot cracking for certain materials such as 2024 high-strength aluminum. Since the material melting cannot be modeled in commercial software, large compressive strain was predicted in the weld pool and behind the weld pool. Therefore, weld hot cracking cannot be modeled without developing the modeling capability of material melting.

The unique phenomenon in welding is melting and re-melting. Strain and stress relief due to weld melting/re-melting effects is the key for modeling weld process. A thermo-elastic-plastic constitutive model was developed for weld simulation [165]. In this model, the rate form of the strains can be written as

$$\underset{\sim}{\dot{\varepsilon}}^{Tot} = \underset{\sim}{\dot{\varepsilon}}^{e} + \underset{\sim}{\dot{\varepsilon}}^{p} + \underset{\sim}{\dot{\varepsilon}}^{T} + \underset{\sim}{\dot{\varepsilon}}^{A} + \underset{\sim}{\dot{\varepsilon}}^{ph} \tag{21}$$

where $\underset{\sim}{\dot{\varepsilon}}^{Tot}$, $\underset{\sim}{\dot{\varepsilon}}^{e}$, $\underset{\sim}{\dot{\varepsilon}}^{p}$, $\underset{\sim}{\dot{\varepsilon}}^{T}$, $\underset{\sim}{\dot{\varepsilon}}^{A}$, $\underset{\sim}{\dot{\varepsilon}}^{ph}$ are the total, elastic, plastic, thermal, "annealing," and phase change strain rate tensors, respectively. The elastic, plastic, and thermal strains are defined in the classical sense. As required in welding process simulation, we postulate the existence of an "annealing strain," which is only important at near-melting temperatures. The "annealing strain" eliminates the history of prior straining above a reference temperature (such as at melting), $T_A$. For instance, once reaching melting temperature, all accumulated elastic and plastic strains $\underset{\sim}{\dot{\varepsilon}}^{e} + \underset{\sim}{\dot{\varepsilon}}^{p}$ and stresses should be vanished in the context of solid mechanics analysis procedures as the material transforms from solid to liquid states. To restore such a "virgin" state, the associated annealing strain $\underset{\sim}{\dot{\varepsilon}}^{A}$ can be expressed as

$$\underset{\sim}{\dot{\varepsilon}}^{A} = -\underset{\sim}{\dot{\varepsilon}}^{A}\left(\dot{T}, T, \underset{\sim}{\varepsilon}\right) \tag{22}$$

where $\underset{\sim}{\dot{\varepsilon}}^{A}$ is a function of temperature, its rate, and strain. Neglecting solid-state phase change effects for the present discussions, the stress strain relation may be written as

$$\underset{\sim}{\dot{\sigma}} = \underset{\approx}{E} : (\underset{\sim}{\dot{\varepsilon}}^{Tot} - \underset{\sim}{\dot{\varepsilon}}^{p} - \underset{\sim}{\dot{\varepsilon}}^{T} - \underset{\sim}{\dot{\varepsilon}}^{Ap}) \tag{23}$$

where $\underset{\approx}{E}$ is the temperature dependent elastic stiffness tensor, and we distinguish between plastic ($\dot{\varepsilon}^{Ap}$) and elastic ($\dot{\varepsilon}^{Ae}$) annealing strains.

For the annealing strains, we assume

$$\begin{aligned} \dot{\underset{\sim}{\varepsilon}}^A &= 0, && \text{for} \quad T < T_A \\ \dot{\underset{\sim}{\varepsilon}}^A &= \left(\frac{\dot{T}}{T_m - T}\right)^m \underset{\sim}{\varepsilon}^A, && \text{for} \quad T_A < T < T_m \end{aligned} \tag{24}$$

where $T_m$ is the material melting temperature, $T_A$ is the annealing temperature, and $m$ can be assumed to fit various material annealing behaviors.

*Special considerations in modeling FSW*: Compared with fusion welding, residual stresses in FSW joints are expected to be low due to a relatively low heat input. However, apart from the heat input, the force from the tool also plays an important role in the development of weld residual stresses. Analysis results and experimental measurement showed that due to the effect of the tool force, the longitudinal residual tensile stresses became smaller and were asymmetrically distributed at different sides of the weld center. The peak of the tensile residual stresses at the retreating side was lower than that at the advancing side [166]. The down force applied on the FSW tool significantly reduces residual stress. This is because the down force forges and extrudes the materials around tool to reduce the residual strain in weld which leads to the reduction of residual stress. Furthermore, the mechanical loads change the correlation of strain on top surface and bottom surface of sheet, which results in the change of distortion pattern [167].

**5.5 Numerical Modeling Applications.** Traditionally, engineering practices have not accounted for residual stress fields and material changes after welding in structural design calculations. A large safety factor was given during structure design to account for the uncertainties. This design approach increases structure weight, reduces fuel efficiency, and limits structure performance. An integrated computational material engineering approach was developed recently in which weld residual stress is predicted with the thermal model, the microstructural model, and the thermomechanical model [168,169].

In theory, the thermal-mechanical-metallurgical model should be a coupled model since interactions may exist between thermal, mechanical, and metallurgical effect. However, metallurgical model is often ignored during predicting weld residual stress and distortion for low carbon steels because martensite would not be produced in the welded joint [169]. For high-strength steels such as HY-80 and HY-100, metallurgical model has to be included since martensite microstructure phase will be formed in the welded joint. Phase transformation induced plasticity must be included to predict weld residual stress and distortion. Simulation results [170] revealed that the final residual stress and the welding distortion in low carbon steel do not seem to be influenced by the solid-state phase transformation. However, for the medium carbon steel, the final residual stresses and the welding distortion seem to be significantly affected by the martensitic transformation [171].

Numerical modeling of welding processes has been widely used in solving industrial problems related to weld residual stress and distortion. The following are example applications of numerical modeling:

- Identifying the root reason of the primary water stress corrosion cracking detected in Alloy 82/182 butt welds in several US nuclear plants [172].
- Understanding the mechanical and metallurgical reasons for the ductility-dip cracking and solidification cracking in a down-comer steel pipe and proposed a solution to mitigate the cracking [173]
- Simulating laser cladding manufacturing process for aero-engine repair [174]
- Predicting welding-induced distortion in thin structures [175] and heavy structures [176]
- Multiphysics modeling of a welded furnace roll for identifying failure root cause [177] and improving creep-fatigue life [178]
- Optimizing welding sequence of multi-pass welding of aircraft tie-downs for ship building application [179]
- Developing transient thermal tensioning technique to weld thin steel ship panel structures [180]

## 6 Challenges From Sensing and Dynamic Control

Using numerical simulations as the predictive models, the result from welding can be predicted. Optimized welding parameters/procedure can thus be designed. Since this design (Fig. 3) is done based on the nominal conditions and the welding/manufacturing conditions may deviate from the nominal conditions, the actual welding parameters will have to be adjusted, as analyzed in Sec. 6.1, to still obtain the desired welding results. This requires real-time sensing and dynamic control and welding processes make their sensing and control challenging. We will discuss the challenges in Sec. 6.2 and present directions for solutions in Sec. 6.3.

**6.1 Why and When Sensing and Controls Needed?** Manufacturing process can be considered a physical realization of the predictive model $o(\varpi/\kappa)$, i.e., using $\varpi$ to produce $o$ under given conditions $\kappa$. The design gives us $o(\varpi^*/\kappa^*) = o^*$. That is, if the actual welding conditions $\kappa$ are the same as the nominal conditions $\kappa^*$ under which we designed, then using the designed welding parameters, we will be able to produce the desired output from the welding manufacturing process, i.e., producing $o^*$.

Sensing and controls are needed if the actual $o$ significantly differ from $o^*$. Realistically, this typically occurs in two cases: (1) $\kappa \neq \kappa^*$, i.e., the actual manufacturing conditions deviate from the nominal conditions; (2) the predictive model $o(\varpi/\kappa)$ deviates from that used in design, i.e., the process has uncertainty. Another possible cause is that the actuation system is unable to follow commands $\varpi^*$ to actually produce welding parameters accurately. This is logically possible but for model actuation systems used in welding manufacturing it should not be a concern.

Predictive model $o(\varpi/\kappa)$ gives the relationship between $o$ and $\varpi$. In the relationship, $\kappa$ does not appear in the model but the model itself depends on $\kappa$. When $\kappa$ changes, the relationship between $o$ and $\varpi$ changes. Hence, if $\kappa$ deviates from $\kappa^*$ such that $\kappa = \kappa^* + \Delta\kappa$, using $\varpi^*$ will not make $o = o^*$, that is $o(\varpi^*/\kappa^* + \Delta\kappa) \neq o(\varpi^*/\kappa^*) = o^*$. To still make $o = o^*$ using $\varpi^*$, we must eliminate $\Delta\kappa$. However, this is often not realistic for manufacturing due to the cost constraints. A solution would be to find a $\Delta\varpi$ such that $o(\varpi^* + \Delta\varpi/\kappa^* + \Delta\kappa) = o(\varpi^*/\kappa^*) = o^*$.

Although we have used the relationship between $o$ and $\varpi$ given in the predictive model $o(\varpi/\kappa)$ to find $\varpi^*$ such that $o(\varpi^*/\kappa^*) = o^*$, the predictive model would not work well if $\kappa$ deviates from $\kappa^*$. $\kappa = \kappa^*$ is only implied; it determines the model but is not part of the model parameters whose change would not affect the accuracy of the model. As such, we only have predictive model $o(\varpi/\kappa^*)$ but do not have predictive model $o(\varpi/\kappa^* + \Delta\kappa)$. Mathematically solving $o(\varpi^* + \Delta\varpi/\kappa^* + \Delta\kappa) = o(\varpi^*/\kappa^*)$ becomes infeasible.

A method to find $\Delta\varpi$ is to first make a guess $\Delta\varpi^{(0)}$ and apply $\varpi^* + \Delta\varpi^{(0)}$ to weld. The resultant output $o^{(1)} = o(\varpi^* + \Delta\varpi^{(0)}/\kappa^* + \Delta\kappa)$ from the welding process should not be equal to $o^*$. At time $k$, we need to make a decision on how to adjust $\Delta\varpi$ to modify from the previous $\Delta\varpi^{(k-1)}$:

$$\Delta\varpi^{(k)} = \Delta\varpi^{(k-1)} + \gamma(o^{(k)} - o^*) \tag{25}$$

If $o$ and $\varpi$ are scalars, $\gamma$ is also a scalar. If increasing $\varpi$ increases $o$, the system has a positive gain. In this case, $\gamma$ should be negative. As a result, if $o^{(k)} > o^*$, $\Delta\varpi^{(k)}$ will be reduced from $\Delta\varpi^{(k-1)}$ to reduce the output such that $o^{(k+1)}$ due to the new welding parameters adjustment $\Delta\varpi^{(k)}$ will be closer than $o^{(k)}$ to $o^*$. This is the principle of feedback control. Assuming that the system is linear and static and the system gain is $G$, then one can simply select

$\gamma = -(1/G)$. If this is the case, then $\Delta\varpi^{(k)} = \Delta\varpi^{(k-1)} - ((o^{(k)} - o^*)/(G))$ or $\Delta\varpi^{(k)} - \Delta\varpi^{(k-1)} = -((o^{(k)} - o^*)/(G))$. As a result, $o^{(k+1)} - o^{(k)} = G(\Delta\varpi^{(k)} - \Delta\varpi^{(k-1)}) = -(o^{(k)} - o^*)$, that is, $o^{(k+1)} = o^*$. When the model is not accurately known, we will be unable to achieve $o^{(k+1)} = o^*$ but $o^{(k+1)} - o^*$ reduces as the nominal gain used to calculate $\gamma$ is closer to the actual gain $G$. The adjustment can continue for $o^{(k+2)}$ to get closer to $o^*$ than $o^{(k+1)}$.

Despite just using a simple linear static system as an example to illustrate, we can still see (1) an inaccurate predictive model makes solving $o(\varpi^* + \Delta\varpi/\kappa^* + \Delta\kappa) = o(\varpi^*/\kappa^*)$ to find the needed adjustment $\Delta\varpi$ to achieve the desired output infeasible; (2) however, if we can measure the process feedback (actual output) $o$, we can adjust the welding parameters gradually to finally achieve the desired output, that is, $o = o^*$ despite the inaccuracy in the model; (3) a more accurate model helps adjust the welding parameters to achieve the desired output faster.

As can be seen, the problem is that we do not have an accurate model. We above discussed the case where we have an accurate model during the manufacturing design under the given/implied nominal conditions but the model becomes inaccurate during manufacturing due to the deviations of manufacturing conditions from nominal ones. There is another case that the process itself has uncertainty, i.e., the process output differs each time despite the same welding parameters being applied. If this is case, we probably should have known about it when we design because we cannot find a $\varpi^*$ such that $o(\varpi^*/\kappa^*) = o^*$. We can only have that $P(o(\varpi^*/\kappa^*) - o^*)$ minimal where $P$ is a semi-positive definite function as the objective function to be minimized through optimizing $\varpi$. The good news is that the principle of feedback control as simply illustrated by Eq. (25) works despite the cause of the inaccuracy of the model.

**6.2 What Are the Challenges?** *Problem engineering*: The challenges first lie in that the outputs of our concern, i.e., $o$, are often not directly measurable during welding. As such, we typically pick those whose values are critical and are sensitive to the manufacturing conditions $\kappa$ and welding parameters $\varpi$ as the set of outputs for sensing and feedback control. In this way, we divide $o = (\{o^{(1)}\}^T, \{o^{(2)}\}^T)^T$ into two sets $o^{(1)}$ and $o^{(2)}$ for those that are critical and sensitive and those that are not, respectively. We can also divide $\varpi = (\{\varpi^{(1)}\}^T, \{\varpi^{(2)}\}^T)^T$ into two sets $\varpi^{(1)}$ and $\varpi^{(2)}$ for those that are needed to adjust $o^{(1)}$ and those that are not necessary.

Since welding parameters in $\varpi^{(2)}$ are not adjusted, we will use their values obtained from the design, that is, $\varpi^{(2)} = \{\varpi^{(2)}\}^*$ such that we can count them as part of the manufacturing conditions $\kappa^*$. Since only $\varpi^{(1)}$ will be adjusted, we can denote $\varpi^{(1)}$ as our new $\varpi$. Our new model may still be symbolically denoted as $o(\varpi/\kappa)$ and our control is still to determine $\varpi$ such that $o(\varpi^* + \Delta\varpi/\kappa^* + \Delta\kappa) = o^*$. (We assume that the values of $o^{(2)}$ achieved by adjustment $\Delta\varpi$ are still acceptable.) We may refer this as *problem engineering*. This is the first step in sensing and control that determines the *outputs and control variables of the feedback control system*. This is probably the primary challenge.

*Physical realizability of sensing—environment and unmeasurable issues:* The second step and challenge are to develop the ability to real-time measure the redefined system output $o$ such as the temperature distribution [181,182], weld pool geometry [183], weld penetration—measured by the depth of the weld pool [184] for partial penetration (incomplete penetration) and the width of the weld on the lower surface for full penetration [185] (complete penetration)—and the cooling rate [186]. There are three major challenges in sensing: poor environment of welding as such high temperature and extreme brightness, not being directly measurable such as the depth of the weld pool, and difficulty in correctly/effectively correlating the measurable phenomena to unmeasurable outputs.

Take arc welding and laser welding as example to illustrate the effect from the process/environment. For arc welding, the bright arc and smoke are major challenges in observing the process to take measurables that may link to the process output of concern. For GMAW process, possible spatters and increased smokes add additional challenges. For laser, strong metal vapors increase the difficulty to observe the process. Also, the fast speed and reduced size require the sensor to be faster with better resolution. This is also true for measuring some of the manufacturing conditions such as the weld seam and gap in laser welding.

Take the depth of the weld pool as example to illustrate the challenge from sensing unobservable output. In this case, what we are supposed to measure in real time is the depth of the weld pool that occurs underneath the work-piece. They may be measured using ultrasonic sensor or X-ray in real time but most time their applications in real time are difficult or difficult to be justified. As such, we have to find measurables that really have inherent relationship with it. This is not easy and is very much process dependent. We have to solve the problem case by case based on our in-depth knowledge of the process and cannot be guaranteed for success every time.

Finally, even if we can successfully find measurables that are inherently correlated to the outputs and measure them in real-time, successfully deriving the outputs from the measurables may still be challenging due to the complexity of the relationship. Often the time, finding the right information/features from the measurables is challenging and requires in-depth understanding of the process. The use of machine learning techniques [187] has reduced the dependence on in-depth understanding of the process and made extracting information from measurables easier.

*Dynamic modeling and control*: With the availability of real-time feedback $o^{(k)}$, a control algorithm $\Delta\varpi^{(k)} = \Delta\varpi^{(k-1)} + \gamma(o^{(k)} - o^*)$ can be implemented. However, designing its parameter $\gamma$ requires the model of the process. We have above illustrated briefly the dependence of an effective control algorithm on the accuracy of the model. Our first challenge is thus obtaining an as accurate as possible model. Uncertainties including deviations from nominal manufacturing conditions are the major issue in obtaining an accurate model. Nonlinearity/complexity of the relationship increases the challenge. Online real-time requirement discourages complex models such that models must be simplified to a degree that is suitable for real-time application. An effective dynamic control algorithm such as model predictive control [188] involves using the model to mathematically express the predicted outputs as functions of the control variables or their adjustments $\Delta\varpi$ and then optimize $\Delta\varpi$ such that the predicted output $o$ close to $o^*$. The real-time solutions of the optimized $\Delta\varpi$ becomes challenging as the complexity of these functions increases. In summary, the major challenge in modeling the process is to obtain a simplified (for real-time solution) yet accurate (for control quality) dynamic model of the process. This is also an art of problem engineering and is thus challenging. We have to balance between complexity and accuracy.

Fortunately, the model accuracy in most cases does not play a critical role for welding process feedback control except for affecting the control speed. Welding process in most cases with particular concerns are stable and the processes may still run if no adjustments on the control variables are made. The consequence would be just producing outputs $o$ that are no equal to $o^*$. For an unstable process, the process would not run if no appropriate adjustments are made. For our concerns with stable welding processes, a more accurate model helps the control system to more effectively make adjustments to approach $o^*$ more quickly with more desirable trajectory.

The major challenge in control algorithm design arises from the dynamics of the process that makes the output not fully respond to the control adjustments immediately. As such, when making a control adjustment decision, the effects, from control adjustments applied at different previous times, and from proposed future control adjustments to be applied at different future times, on the outputs at different future times need to be taken into consideration. A good solution is thus not intuitive. A good news is that control system design is a branch of applied mathematics. With contributions from applied mathematicians, researchers, and engineers,

effective yet relatively easily understandable control algorithms and design methods have been developed.

In **Summary**, the most challenging issue is the *problem engineering* that converts a real world problem into a problem that can be solved using an engineering approach, that is, defining a control system with its outputs and control variables specified as well as the desired outputs specified. We then must assure that the control system defined has a *physical realizability*, i.e., all the feedback of the outputs can be obtained from the physical process and all the control variables can be implemented in the physical process/system. In practice, the challenge lies in the ability to obtain the feedback information from the physical process due to the environment of welding process and the unobservability of some outputs. After the control system becomes realizable, the problem reduces to designing a control algorithm.

For *problem engineering*, it requires a lot of physics analysis and engineering trade-off and there is no general guidance to success. For *physical realizability* of sensing, it is process and application dependent, i.e., particular processes create particular environmental challenges to observe them and particular outputs/requirements determine what we need from the process. We first briefly discuss general guidance to scientific methods involved and review specific efforts in Sec. 6.3 accordingly.

**6.3 Effective Methods.** *Deep learning versus hand engineering*: Assume some output in $o$ is an output whose feedback is needed but it is not directly measurable. Assume that we have overcome the environmental issues to obtain the real-time observation of relevant phenomena $\Xi$ from the welding process. Our task now is to derive this output in $o$ from $\Xi$. Assume that we have conducted the needed analysis to make sure that $\Xi$ does contain all the information needed to determine this output in $o$. To be simple, we assume that the problem is to determine $o$ from $\Xi$.

Our challenge here is how to actually obtain a mathematical mapping

$$o = v(\Xi) \tag{26}$$

from available experimental data pairs $(o(k), \Xi(k))(k = 1, \ldots, N)$. It is challenging because $\Xi$ is in general complex and we do not know how we should characterize/parametrize $\Xi$ such that we can correlate their characteristic parameters to $o$. Conventional methods are to study into the process/phenomena/mechanisms to propose a set of characteristic parameters $\theta$, develop algorithms to calculate $\theta$ from $\Xi$, and then use $(o(k), \theta(k))(k = 1, \ldots, N)$ to fit a model

$$o = u(\theta) \tag{27}$$

If the accuracy is satisfactory, the model is accepted; if not, study again to propose another set of $\theta$ and develop algorithms to calculate it. It is referred to as hand engineering [187] and is a labor-extensive trial-and-error method. The success is not guaranteed even if $\Xi$ is adequate.

The progress in machine learning, in particular in deep learning [187], has made it possible to directly relate $\Xi$ to $o$ without the need to first propose a set of characteristic parameters $\theta$. Basically, the mapping structure becomes much more complex to allow right, relevant characteristics be automatically extracted directly from $\Xi$. This becomes possible because the progress in deep learning has been made the convergence of optimization, of large networks with large number of parameters to optimize, realistic. As such, human hand engineering [187] is replaced by mathematical optimization to best fit $o = v(\Xi)$ to the available data pairs $(o(k), \Xi(k))(k = 1, \ldots, N)$. The success becomes easier and the only major requirement is to make sure that $\Xi$ indeed contains adequate information to determine $o$.

For welding process sensing, $\Xi$ is often images from the welding process. For such type of phenomena—image, the convolutional neural networks (CNNs) [187] have been found to be effective to extract characteristics from images. There have been successful applications of CNNs to use deep learning method to interpret $\Xi$ in the form of images to determine unobservable $o$ [189–193].

*Dynamic modeling*: We now assume that we have identified our outputs and inputs/control variables and can obtain the feedback for the outputs. We have denoted them as $o$ and $\varpi$ and will now denote them as $y$ and $u$ for the convention in control literature, i.e., $y = o$ and $u = \varpi$.

A system is linear if the superposition principle applies [194]. For digital control of our concern, we can model the process using a difference equation

$$\begin{aligned} y[k] = &-A_1 y[k-1] \ldots - A_n y[k-n] \\ &+ B_1 u[k-1] \ldots - B_n u[k-n] \end{aligned} \tag{28a}$$

Or a state space description

$$\left.\begin{aligned} x[k+1] &= Ax[k] + Bu[k] \\ y[k] &= Cx[k] \end{aligned}\right\} \tag{28b}$$

These two forms of model can be converted and $A_j's$, $B_j's$, and $A$, $B$, $C$ are model parameters. If the systems are nonlinear, we denote

$$y[k] = h(y[k-1], \ldots, \ y[k-n], \ u[k-1]), \ldots u[k-n]) \tag{29a}$$

$$\left.\begin{aligned} x[k] &= f(x[k-1], u[k-1]) \\ y[k] &= g(x[k]) \end{aligned}\right\} \tag{29b}$$

The mathematic format/structure of nonlinear functions $f$, $g$, $h$ (including linear) can be any including artificial neural networks, fuzzy systems, and neurofuzzy systems. The methods to fit these nonlinear (including linear) functions from experimental data are dependent on the specific mathematic structure and have typically been developed from applied mathematicians. In general, if functions are linear, the model parameters can be solved from experimental data analytically; if are nonlinear, iterative optimizations will be involved.

*Dynamic control*: A challenge in designing a control system is to select the structure of the control algorithm. Each particular control algorithm requires a preferred model structure and the designing method varies. However, the model predictive control [188] can provide a conceptually uniform solution to make control algorithm design an easier job. To be illustrative, we use model (29*b*) to derive the following predictions made at time $k$:

$$\left.\begin{aligned} \hat{x}[k+1/k] &= f(x[k], u[k]) \\ &= f_1(x[k], u[k]) = f_1(x[k], U) \\ \hat{x}[k+2/k] &= f(\hat{x}[k+1/k], u[k+1]) \\ &= f(f_1(x[k], u[k]), \ u[k+1]) \\ &= f_2(x[k], u[k], u[k+1)) = f_2(x[k], U) \\ &\ldots\ldots \\ \hat{x}[k+M/k] &= f_M(x[k], U) \end{aligned}\right\} \tag{30}$$

where $U$, including $u[k]$, $u[k+1]$, …, $u[k+M]$, is the set of current and future control actions to be determined. Often the case we can choose $u[k] = u[k+1] = u[k+M]$. In such a case

$$\hat{x}[k+j/k] = f_j(x[k], u[k]) \tag{31}$$

Since $x[k]$ is supposed to be the available feedback that can be obtained from the process output measurement, the predicted future state is really just a function of the control action $u[k]$ to be determined. The model predictive control can be specified as to find $u[k]$ that minimizes the difference between the predicted future state with the desired $x^*[k+j]$ which can be derived from $o^*$. That is

$$\begin{aligned} \min_{u[k]} \sum_{j=1}^{M} &(f_j(x[k], u[k]) - x^*[k+j])^2 \\ &+ \lambda(u[k] - u[k-1])^2 \end{aligned} \tag{32a}$$

or

$$\min_{u[k]} \sum_{j=1}^{M} (g(f_j(x[k], u[k])) - y^*[k+j])^2 + \rho(u[k] - u[k-1])^2 \quad (32b)$$

where the term $\lambda(u[k] - u[k-1])^2$ and $\rho(u[k] - u[k-1])^2$ with $\lambda > 0$, $\rho > 0$ penalize the change in the control. For most welding processes control problems, this unconstraint optimization will be adequate due to the penalty term $\lambda(u[k] - u[k-1])^2$ or $\rho(u[k] - u[k-1])^2$. If the dynamic model is linear, an analytic solution will be obtained. Otherwise, ways are needed to make the optimization can be solved online.

## 7 Sensing and Control

We review the existing efforts that address the challenges analyzed in Sec. 6.2 and those that solve problems along the directions identified in Sec. 6.3.

**7.1 Sensing.** *Weld seam tracking*: Weld seam is the most important information for a successful welding manufacturing. Welding must be done at the right positions to join metals. The most direct method to find the weld seam appears to be using machine vision, in particular vision using a structured light [195]. The arc is bright but the spectrum is relatively board [196]. This is similar to the radiation of the extremely bright plume in laser welding that consists of metallic vapors and plasma generated and ejected from the keyhole. Within a narrower range of wavelength, the intensity of the radiation of the arc and laser plume will be reduced. On the other hand, the bandwidth of the illumination laser is less than hundredth of a nanometer. To further reduce the effect from the radiation, the structured laser is typically projected a few millimeters ahead of the front edge of the weld pool, referred to as preview. Since the radiation, either from the arc or the laser plume, decays cubically in distance, the effect from the radiation is further reduced. By using a narrow band optical filter in front of the camera, the projected laser stripe can be clearly viewed despite the arc and laser plume. When there is angle between the camera view and laser stripe, the distortion of the laser stripe by the surface geometry such as the joint groove or gap can be viewed in the image and be processed relatively easily to determine the position and geometry of the groove if the surface is not shinning. There have been many improvements in algorithms for quicker and more accurate detection [197–200].

Through-the arc seam tracking, Ref. [201], is often a preferred method because it uses the arc characteristic/signals without an additional sensor. It is to spin, rotate, or scan the arc to generate a motion of the arc in relation to the weld seam transversely. This is apparent to work for GTAW process since the voltage is proportional to the distance between the tungsten electrode and the work-piece surface. The peak of the scan voltage corresponds to the bottom of the work-piece surface that is the seam. However, the arc may blow such that the accuracy is reduced. To overcome this issue, a non-transfer plasma arc/jet which is not bendable has been invented [202,203] to more accurately sense the weld seam and groove geometry. For GMAW, the tip of the wire (a terminal of the arc) varies. The arc voltage can no longer represent the distance from the contact tip (whose position does not vary) and thus can no longer be used to find the bottom of the work-piece from a scan. However, for GMAW, when the contact-tip-to-work distance increases, the current will be reduced. The current waveform can thus be used to analyze the weld seam [201]. However, for butt joint with a small gap, the accuracy is not sufficient such that the more expensive and less convenient structured-light method would need to be used.

*Weld pool boundary*: Despite the specific purposes that may vary from application to application, a general interest persistently exists that we wish to see what are happening during welding. We first wish to see what humans can see and visual views of the welding process are thus often the first to consider. Human welders are capable of observing the welding process to extract the needed information to make appropriate adjustments so that they can adapt to the changes in the welding manufacturing conditions. Human welders can see where the weld seam is despite the arc radiation. Human welders can see the weld pool (boundary) and its variation. Human welders can also see the 3D weld pool surface. However, all these and other information human welders can see are not easily obtained using machines/sensors. Special requirements are needed for sensors to be capable of sensing what are occurring during welding especially arc and laser welding.

Arc radiation is the first apparent obstacle for sensors to observe the scenes/objects during arc welding process. Arc is too bright in comparison with other objects of our interest such as the weld pool boundary and the joint groove/weld seam. A smart method was proposed by Richardson and Gutow by installing a camera to observe the weld pool area co-axially from above the tungsten [204]. This method is referred to as co-axial view of the weld pool and tungsten blocks the majority of the arc radiation from reaching the co-axial camera. Clear weld pool images were obtained. To observe from other directions, a direct solution is to use another light source to illuminate the objects of our interest that is even brighter than the arc radiation. This appears to be impossible but using a laser, which is theoretically single color/wavelength, as the illumination source can make this possible. The energy of the arc radiation spreads in an extremely wide range [205,206] but the band pass optical filters with the Full Width-Half Max less than 10 nm are standard commercial products available off out shelf for various wavelengths of lasers. As such, the energy passing to the imaging sensor of a camera from the object as the reflection of the illumination laser can be much greater than that of the arc radiation. This results in the structured-light method by projecting the laser as a stripe across the joint approximately transversely ahead of the weld pool [207], probably as the most effective way to sense the joint groove/gap for seam tracking. To effectively reduce the effect from the arc radiation, the laser stripe is a typically projected to the groove with a distance of a few millimeters from the front edge of the weld pool. To further increase the illumination, the laser is focused, projected as a dot, and scanned across the groove/joint [208].

The kind of machine vision methods that uses an illumination light source is referred to as active vision [209]. While the above technologies take advantage of the wide spreading characteristic of the arc energy spectral distribution, another method has been based on a different principle—using an illumination light whose power is even much greater than that of the arc radiation, but just during its pulse [210]. This method used a pulsed laser whose duration is in nanoseconds. As a result, although the average power of the laser is 7 mW, the peak power during the pulse is 70 kW [210], which is much greater than that of the arc radiation. To sense the reflections from the objects to this laser, the shutter of the camera is synchronized with the pulse of the laser [210]. As a result, the arc radiation is completely removed from the image [210]. Image as shown in Fig. 32 can be obtained [210]. Using this technology, the weld pool boundary can be clearly observed [210] where the dark area is the weld pool which specularly reflects the illumination laser such that such reflection is not collected to the imaging sensor of the camera; the bright area is due to the diffuse reflections of the laser from the solid metal which is insensitive to the view angle. Using the technology, the boundary has been clearly monitored, processed, and modeled for process control [210–214].

Another method to view the weld pool is to use an Ultra Dynamic Range™ technology. Cameras have been commercialized by Visible Welding Inc. using this technology to provide vibrant full color viewing of the arc and molten metal at the same time.[2] Figure 33 shows clear images observed from the cameras.

[2]https://visiblewelding.com/

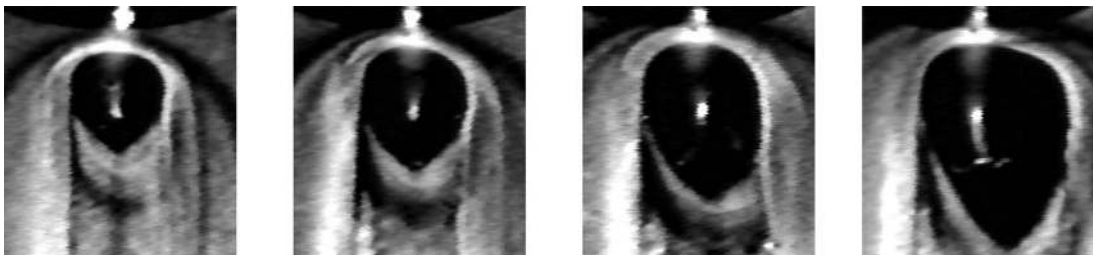

**Fig. 32 Images of the weld pool boundary using a synchronized pulsing illumination laser and camera—images acquired during studies in Refs. [210–213]**

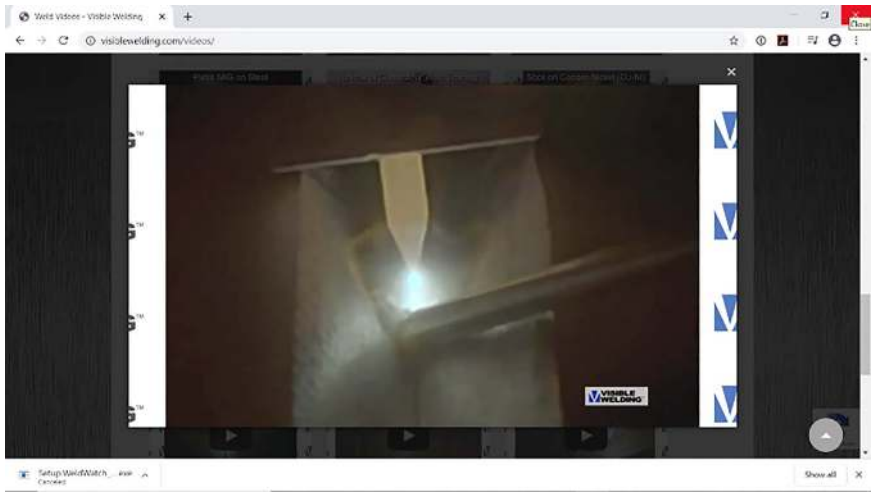

**Fig. 33 Image of weld pool and arc captured by a camera using the Ultra Dynamic Range™ technology of Visible Welding Inc. (downloaded from open video sources at https://visiblewelding.com/videos/)**

3D weld pool surface can provide more information about the welding process for its feedback control. The University of Kentucky has projected a laser dot matrix on the weld pool surface and intercepted the reflections from the weld pool surface to calculate 3D weld pool surface based on the reflection law in real time [215,216]. However, the device and algorithm are still too complex for an easy implementation in manufacturing environment.

*Laser process*: Seam tracking is a major issue in laser welding due to the small diameter of the laser beam. Typical signals to monitor a laser process are from sound, light, electricity and heat [217–223]. Lee and Na [220] developed a visual sensor without auxiliary light source and preview distance. They developed an effective image processing algorithm to directly extract the molten pool and locate the weld seam, which is critical for the highly precise pulsed laser edge welding. Compared with the traditional vision sensor for seam tracking, this novel vision sensor effectively reduced the tracking error and is suitable for micro-welding of small parts. In order to solve the problems of low tracking accuracy and high detection noise of weld seam deviation in high-power narrow gap laser welding, Gao et al. [217] used a Sage–Husa adaptive Kalman filter (AKF)-embedded Elman neural network to detect the weld seam position. First, a high-speed near-infrared imaging acquisition system was designed to collect the infrared images from the molten pool and surrounding region. Then, the state and measurement equations for the weld seam position were established based on an eigenvector derived from the weld seam position variable, which was in turn derived from the collected near-infrared image sequence. In another study, Shao et al. [219] proposed a seam measurement method based on vision sensor to measure different wavelength of laser for space weld seam of narrow butt joint in laser welding. The corresponding image processing algorithm has been developed to extract the centerline of the red laser stripes as well as the seam features. Ancona et al. [224] studied the $CO_2$ laser-induced plasma's optical signal emitted during welding of AISI 304 stainless steel and determined electron temperatures of the various chemical species that compose the plasma plume simultaneously by use of related emission lines.

Process monitoring becomes even more critical for laser welding because of the much increased process complexity. This is particularly true for laser keyhole welding, a major penetrative process available to manufacturers. As demonstrated by You et al. [225], in keyhole laser welding process, a plume consisting of metallic vapors and plasma (ionized gas) is generated within the keyhole through laser–material interaction and ejected from the keyhole. This plume has abundant information about the process and its characteristics vary with laser and gas. For example, for $CO_2$ laser welding, the plume constituents change from the emission of neutral metal atoms to also including plasma when the shielding gas changes from helium to argon or nitrogen. During fiber laser welding, the plume is in the state of weakly ionized plasma. In addition, the laser process is quick and highly dynamic involving radiation, molten pool, keyhole, plume, spatters, and fast cooling and it is thus prone to process instability, cracking, undercuts, underfills, porosity, keyhole closure, and incomplete penetration.

Complexity in laser welding requires various sensing capabilities for different process characteristics/signals. You et al. [225] introduced six commonly used sensors, as summarized in the following. *Photodiode sensors* are simple/easy to use and the costs are relatively low such that multiple sensors of different wavebands can be used to monitor different signals including plasma radiation, laser reflection, and thermal emission. The sensors are ultraviolet and visible (200–750 nm) for plasma radiation, then increase the waveband to 1070 nm for fiber laser and 1030 nm for disc laser for laser reflection, and to (1100−1700 nm) for infrared radiation.

*Visual sensors*/images can acquire more comprehensive and detailed information due to the increased information from dimensions/resolutions. They can directly observe the process not only for visible but also for infrared information. They can also observe the process with auxiliary/illumination lights. Most of the visual sensors for weld pool monitoring and weld seam tracking discussed above with arc welding as example can be directly applied to laser welding. *Spectrometer* detects line spectra from the plume/plasma and the electron temperature of different elements can be calculated from the relative intensity of the line spectra. It was found that for aluminum welding, the occurrence of conspicuous weld defects (such as undercuts and burns-through) can be predicted not only from just the overall radiation intensity but also from the increase in aluminum spectral line intensity. Some weld defects were found to be closely correlated to certain features in acoustic emission such as the intensity of certain frequency or the oscillation amplitude of certain frequency components. However, noncontact *acoustical sensors* that are suitable for industrial/manufacturing applications are subject to the interference of environmental noises and intelligent algorithms are thus needed to improve their accuracy and robustness. *Pyrometer* provides cost-effective solutions to monitor and analyze the dynamic changes in the temperature as a result of laser processing. *Plasma charge sensor* uses an electrical circuit with a gap as a circuit element in the loop. The sensor is designed such that the plasma (ionized gas that is conductive) reflected from the keyhole fills the gap. If the keyhole is fully open, part of the plasma escapes from the bottom of the work-piece; otherwise the plasma fully reflects to the gap. The conductance of the gap changes with the plasma and determines the sensor output (electrical signal). Hence, keyhole state determines the plasma reflection and thus the output of the sensor.

Effectively using multiple process signals is important for the high-speed keyhole laser welding process to operate desirably. This requires advanced sensor fusion and accurate process modeling. Because of the complexity, efforts have been focused fusion of signals from a relatively small number of information sources. There are reports on integration/fusion of photodiode and acoustic signals, of multiple visual (NIR, visible and auxiliary illumination) sensor signals/images, of photodiode sensor and visual sensor signals, of photodiode and plasma charge sensor signals, etc. The use of machine learning in advanced sensor fusion will be discussed below.

*Friction stir welding process* [226]: Weld seam in FSW may also be monitored using a visual sensor like in arc and laser welding. At Vanderbilt University, a method similar to through-the-arc seam tracking in arc welding has been developed [227] by weaving the FSW tool back-and-forth perpendicular to the direction of travel during welding. During this process, the force and torque signals are monitored. Analysis shows that the weld seam can be detected from these signals and experimental results demonstrate that the weaving most likely does not reduce weld quality.

For process monitoring [228], force and torque have been added to FSW together with other common welding process information including temperature, acoustic emission, imaging, etc., as FSW is a mechanical processing where forces are the inputs and play major roles in determining the quality of the produced welds. Su et al. simultaneously monitored the tool torque, traverse force and axial force during FSW [228]. Rather than direct monitoring using load cell or rotating component dynamometer, an indirect but cost-effective method is used that monitors output torques of the servo motors and main spindle three-phase AC induction motor inside the FSW machine. The values of the traverse force, axial force, and tool torque were determined from different welding conditions and were used to analyze the process. Mehta et al. independently proposed a similar method that measures the torque and the traverse force by monitoring the current and power transients of the electrical motors driving the rotational and linear motions of the FSW tool, respectively [229]. In Ref. [230], the torque is evaluated as a means of in-process sensing of tool wear in friction stir welding of metal matrix composites (MMC).

Temperatures at the tool shoulder–work-piece interface can be used to analyze and feedback control the FSW process. Current methods are subject to restrictions on spatial and temporal resolutions. To improve the temperature measurement, Fehrenbacher et al. [231] placed two thermocouples in through holes right at the interface of the tool including one at the tool pin-work-piece interface. This allows the sheaths to be in direct contact with the material and the measurement to reflect dynamic temperature variations at the shoulder and pin within a single rotation of the tool. They found that highest temperatures occur at the shoulder interface between the advancing side and trailing edge of the tool, but closer to the advancing side.

For methods that are less FSW process specific, machine vision has been used to monitor the weld surface during FSW to detect/analyze the weld quality/defects. Bhat at al. used discrete wavelet transforms to analyze images from FSW to extract useful features that are correlated to and can be used to predict good and defective welds [232]. The obtained features were fed to a support vector machine based classification model to classify the welds, good or defective, and obtained 99% accuracy using Gaussian kernel. Ultrasonic detection has been used to detect materials discontinuity for weld joint penetration depth in fusion welding. Tarraf et al. [233] reported the use of guided ultrasonic waves to inspect weld quality in similar aluminum and dissimilar aluminum/magnesium alloys joints made by FSW. In Ref. [234], the propagation characteristics of ultrasonic weld-guided waves in FSW haves been comprehensively investigated.

**7.2 Machine Learning.** The University of Kentucky Welding Research Laboratory [189] has used machine learning method to solve the challenge in interpreting observed welding phenomena to predict the unobservable weld penetration which occurs underneath the work-piece. They believed that the penetration state is related to the residual oscillation of the weld pool. However, conventional methods to monitor the oscillation of the weld pool are to analyze arc length/voltage waveforms. The drawback is that the time period needed to collect the signals must be sufficient and relatively long. To detect the penetration rapidly, they analyzed the reflection from an oscillating pool to projected laser dot matrix and found that the patterns of the reflection images are correlated to the oscillation, thus the weld penetration. Unfortunately, extracting the relevant patterns from the reflection images that can be used to accurately predict the penetration is challenging. To solve this difficulty, they proposed to use the raw images as the input of a CNN whose output is the state of the penetration. An automated robotic GTAW process has been used to generate a large quantity of raw data needed to train the CNN. In addition, the data size was enlarged using data augmentation. A six-layer convolutional neural network trained with a modified mini-batch gradient descent method leaded to a final testing accuracy of 90.7%. A voting mechanism based on three continuous images increased the classification accuracy to 97.6%.

The physics must exist to assure $o = v(\Xi)$ or the results of the learning, despite how deep it is and how large the date used is, will not be valid. In the effort above, the physics is the correlation between the pool oscillation and weld penetration and the correlation between the reflection image patterns and pool oscillation. In another effort [190] at the University of Kentucky, the information source is the weld pool and the arc. For welding of relatively shin sheet, the weld pool boundary can indicate the weld penetration in a certain degree, while it may not be true for welding of relatively thick plates due to the increased deviation in heat transfer. Many previous studies have confirmed this effectiveness for welding of thin sheets. Weld pool images can provide more information on the welding process than the boundary which is just part of the information from the weld pool. In this effort, weld pool and arc were simultaneously imaged as $\Xi$ by a camera directly from the welding process without an auxiliary light or any other artificial stimulations. Although such images are more difficult to process,

more relevant information (than just the weld pool boundary) has been captured. This is an advance toward a better physics mechanism to assure $o = v(\Xi)$. Of course, the difficulty in processing images to obtain features is no longer a matter when directly using a deep leaning method. As such, they established an end-to-end CNN as the structure for $v$ and trained the parameters in $v$. Testing experiments demonstrated 92.70% as the classification accuracy. In order to increase the accuracy and training speed, a transfer learning approach based on residual neural network (ResNet) was developed. This ResNet-based model was pretrained on ImageNet dataset to process a better feature extracting ability and its fully connected layers were modified based on own dataset. Experiments showed that the transfer learning approach decreases the training time and increased the prediction accuracy to 96.35%.

Oak Ridge National Laboratory [191] recently developed a novel framework, referred to as DeepWelding, to use deep learning methods to improve the accuracy in monitoring weld penetration in GTAW process. They used optical images from multisource in multiple types as the input of the framework. To improve the accuracy in predicting unseen data collected from different experimental settings, they combined multiple neural networks. They set an example to use machine learning method to interpret information from multiple sources with possible redundancy to assure the adequacy of the input information.

In an effort by Zhang et al. [235], laser process is monitored using a multiple-sensor system consisting of an auxiliary illumination visual sensor, an ultraviolet and visible band visual sensor system, a spectrometer, and two photodiodes. Features are extracted from these signals using respective processing algorithms. To fuse these features from different information sources/sensors to predict the welding process state, a deep learning framework based on stacked sparse autoencoder has been established. It was found that this proposed sensor fusion framework achieves higher accuracy and better robustness in determining the process state than backpropagation neural network, support vector machine, and random forest.

There are a number of other recent works that used deep learning to solve different problems in welding process monitoring and defects detection [192,193]. While the above efforts used deep learning with a CNN, the machine learning can also be done in simpler ways such as using a support vector machine [236]. Literature search uncovered three publications using such conventional machine learning methods in FSW [237–239] but none of them used deep learning approaches.

**7.3 Dynamic Modeling and Controls.** Proportional-integral-derivative (PID) control is probably the simplest feedback control algorithm and has been widely used in industry and manufacturing. Its three parameters can be tuned following rules of thumb without an explicit need for a process model. This method has also been used in welding process control. Li et al. [240] used a PID controller to control the penetration in a novel process—bypass SAW which is formed by adding a GMAW torch into the SAW process to bypass part of the total current. In this process, the penetration is controlled by the base metal current and the base metal current can be adjusted by adjusting the bypass current when the wire feed speed is given. A penetration model has been established to correlate the penetration depth to the base current. Through sensing the base metal current, the bypass wire speed has been adjusted by a PID control algorithm to change the bypass current. Experiments have been done on DH36 square butt joints to verify the effectiveness of the proposed method including the PID controller. In Ref. [241], Huang et al. proposed a novel approach to tune the parameters of a PID controller for control of an AC shield metal arc welding process. Their novel approach was to use the genetic algorithm to optimize PID parameters and through simulation to evaluate the performance of the output. They compared the performance using their tuned PID controller with those tuned by using the classical Ziegler–Nichols tuning rules.

*Model predictive control*: MPC is considered the only advanced control algorithm that has gained wide industrial applications [242]. There is no exception for welding process control. In welding process control using a model predictive control method, the earliest publication records date back to 1996 to 2000 [243–246]. Model predictive control has recently gained more attention from welding research community. Unfortunately, literature search does not uncover any existing application of MPC in laser welding process control. The lack of dynamic model for complex keyhole process may be responsible.

Liu and Zhang [247] used an innovative 3D vision sensing system to sense the 3D weld pool surface and extracted three characteristic parameters from the surface to estimate weld joint penetration. However, the relationship between these parameters and weld joint penetration as proven to be nonlinear. As such, a neurofuzzy system has been established as a nonlinear mapping to correlate them. The problem was analyzed leading to the need for the control of a dynamic system with the penetration, as measured by the backside width of the weld bead, as the output and the welding speed and current as the inputs. To establish the needed dynamic model, experiments were conducted. A dynamic linear model was first constructed and the modeling result was analyzed. The linear model was then improved by incorporating a nonlinear operating point modeled by an adaptive neurofuzzy inference system. To assure that the weld pool just changes gradually, they used a model predictive control for the predicted penetration to follow a smooth trajectory to reach the desired value. In addition, the change in the control increment was penalized. Welding experiments confirmed the effectiveness of the developed model predictive control in achieving the desired weld penetration.

While the penetration was controlled in Ref. [247] as the single output concerned, Liu and Zhang also controlled the 3D weld pool surface as parameterized by their three characteristic parameters including the width, length and convexity of the weld pool surface [248]. Again, the innovative vision system in Ref. [247] was used to measure the 3D weld pool surface. The dynamic response of these characteristic parameters to welding current and speed as control variables was modeled for two-inputs three-outputs system. Based on the identified dynamic model, a predictive control algorithm was developed to control the process to assure these three characteristic parameters of the weld pool surface be maintained about their desired values. It is possible to control three outputs using two inputs because the outputs are not fully independent.

Anzehaee and Haeri [249] engineered a GMAW process control problem as to use wire melting rate, work-piece heat input, and diameter of the detached droplets as the control variables (control system inputs) to control heat and mass transfer to work-piece. They proposed, developed, and implemented a two-layer controller with PI and MPC in cascade. This allowed them to be able to incorporate constraints on the process variables, improve dynamic performance of the closed-loop system and decrease the interaction level.

Zou et al. [250] considered the monitoring and control of weld penetration in pulsed gas metal arc welding (GMAW-P). GMAW-P is the major arc process for high quality high productivity for welding manufacturing. However, this process is much more complex than GTAW where most penetration monitoring and control studies concentrate to. To find an innovative yet simple solution, they noted that during the peak current period, the arc voltage changes as the weld pool surface is increasingly depressed. This change is believed to be related to the weld penetration. The penetration may also be related to the average voltage during the peak current period. They may thus be used together to monitor the weld pool surface and estimate the depth of the weld pool penetration. In this study, they further proposed to use the relative fluctuation coefficient (C-RF) of weld pool surface by combining these two signals to predict the depth of the weld pool. As such, this coefficient was feedback controlled to control the penetration in the complex GMAW-P. The process is complex and manufacturing condition varies. They thus used the model predictive control to achieve a robust control and estimated the model parameters to make the MPC to be adaptive. Experiments verified that uniform weld penetration depth was produced by the adaptive MPC.

Sartipizadeh and Haeri [251] used the model predictive control to control the droplet transfer frequency in GMAW. We have repeatedly stated that GMAW is a highly productive arc welding process. However, its quality depends on a number of factors, one of which is the transfer of the melted wire from the wire into the weld pool as droplets. While the droplet transfer can indeed be real-time measured, it must use a high-speed camera that is expensive and difficult to use during continuous operation of GMAW process where smoke and spatters are unavoidable. To avoid this challenge, they utilized the hybrid property of the GMAW process to indirectly control the frequency. They obtained a mixed logical dynamical model by considering the hybrid act during droplet detachment. They then designed a nonlinear model predictive controller with variable control and prediction horizons. Their computer simulations verified that their controller improved the quality of the welds.

Model predictive control has also been used to control FSW process at Vanderbilt University. To this end, they first established [252] two different models for MPC to evaluate: (1) a first-order plus dead time (FOPDT) model and (2) a hybrid heat source model that combines the heat source method and a 1D discretized thermal model of the FSW tool. They determined their parameters from experimental data. They found the FOPDT model matches the post-startup-transient data better while the hybrid heat source model is expected to have superior temperature control during the startup transient. In Ref. [253], two models were used to develop respective MPC controllers and the performances were compared against two well-tuned PID controllers. At quasi-steady-state conditions, all four controllers controlled the temperature within 2 deg C around the setpoint without large disturbances. The FOPDT based MPC controller is found superior to the hybrid heat source model based MPC with regard to modeled-disturbance rejection and setpoint changes and competitive with well-tuned PID controllers. During the initial traverse, the hybrid heat source based MPC and PID controller with regulator gains were able to control temperature within 5 °C of the setpoint. However, the FOPDT based MPC and PID controller with servo gains could not maintain satisfactory temperature control. It is apparent that the MPC performance depends on the accuracy of the model used.

*Adaptive control*: We have discussed that a more accurate model helps achieve better feedback control performance. MPC is supposed to be a robust control that is more forgiving for the model accuracy but the above work suggested that it is still model accuracy dependent. Adaptive control is to online identify the dynamic model such that the effect from manufacturing conditions variations on the model accuracy can be reduced. Using the real-time identified model parameters in the control algorithm, which can be a model predictive control, a pole-placement algorithm, or other algorithms that explicitly use process dynamic models. Adaptive control has been used in many fields including welding process control. We note that adaptive control has been used in welding community to refer to feedback control although the feedback control algorithm parameters actually do not change. In this paper, adaptive control is the same in control literature involving changes in control algorithm parameters.

Hardt at MIT with his graduate students Doumanidis, Suzuki, and Song are considered the pioneers using adaptive control to welding process [254–258]. Zhang and Kovacevic at the University of Kentucky continued the efforts in using adaptive control theory to solve welding process problems. In Ref. [243], they addressed the control of a nonminimum-phase plant with variable large orders and delays. They were concerned with the control of the backside bead width of the weld which measures the state of the full penetration. They analyzed popular adaptive control algorithms in literatures and found that the generalized predictive control proposed by Kwon et al. [259] to be promising for their application that adjusts the current and arc length to control the frontside and backside width of the weld bead. To further improve the performance, they made the algorithm to be adaptive and developed an adaptive generalized predictive decoupling control scheme. To decouple their nonminimum-phase multivariable plant, they also proposed a predictive decoupling algorithm. Experiments confirmed the effectiveness of their developed control system.

In Ref. [243], the sensor measured behind the weld pool. While the requirement on the sensor is reduced, a system delay is introduced. For the control to be more real time, they later used a high shutter speed camera with synchronized laser pulse illumination to sense the weld pool boundary clearly and used the boundary to estimate the backside width. While in Ref. [243] they used the current and arc length as the control variables, they replaced the arc length by the travel speed to improve the effectiveness of the adjustment. Due to the improvement in the sensor promising for higher control speed, the modeling accuracy became bottle neck such that ignorance of nonlinearity became a major issue. They found that the correlation between any output and input depends on the value of another input. This cross coupling implies that a nonlinearity exists in the process being controlled [244]. A neurofuzzy model was thus used to model this nonlinear dynamic process. Based on the dynamic fuzzy model, a predictive control system was developed [244]. Experiments confirmed the effectiveness of the developed control system in achieving the desired fusion state despite the different disturbances.

Doumanidis is credited for the scan welding technique that can effectively control the thermal processing of work-pieces. However, this is a complex welding process requiring advanced control to function well. In Ref. [260], Doumanidis and Kwak implemented this process using a robotic plasma arc welding system. They used infrared pyrometry to sense for the thermal scanning. They also used laser profilometry feedback to monitor and control the material transfer under gas metal arc welding. The dynamics of the weld profile geometry (i.e., the bead width and reinforcement height) were modeled by fitting from experimental data. A multivariable adaptive control system has been developed to effectively control the bead profile during multiple pass weld joining, orbital welding, coating hardfacing, and rapid manufacturing methods.

Adaptive control has been more increasingly used to address control challenges recently. In Ref. [261], Wu et al. developed a model-free adaptive control (MFAC) system to control the weld penetration in variable polarity plasma arc welding (VPPAW) based on extreme learning machine. This is a process that is typically used to weld aluminum and alloys in keyhole mode. In their work, a flexible visual sensor was developed to monitor the characteristic parameters of the keyhole at the lower surface of the work-piece. These characteristic parameters include the length, width, and area of the keyhole. Analysis of experimental data suggested that the keyhole characteristic parameters are nonlinearly correlated to the backside width of the weld that measures the weld penetration needing to be accurately controlled. To acquire accurate feedback, an extreme learning machine method has been applied to predict the backside bead weld. With the availability of the process feedback, a novel MFAC has been developed. Closed-loop experiments verified the effectiveness of the MFAC system in simultaneously adjusting the welding current and plasma gas flowrate to control the VPPAW process for obtaining a full-penetrated weld under various initial welding conditions and disturbances. For laser welding of large structures, an adaptive control system has been developed by Zhang et al. [262] to address the varying gap issue. They established an adaptive filling model to adjust process parameters. In particular, a precision 3D laser sensor was used to measure the gap and mismatch and an adaptive parameters table was designed as an adaptive controller based on an optimal back-propagation neural network (BPNN). Experimental results verified the ability of the developed adaptive control system to continuously adjust the parameters in real time despite the variation in the gap and mismatch. Adaptive control has also been studied for torque control in FSW [263]. Welding high melting point alloys and MMC experiences an accelerated rate of tool wear. The performance of the torque control is affected by the tool wear as part of the process dynamics. Through estimating the probe radius, the torque control becomes adaptive. It is found that the torque is controlled effectively while a change in system dynamics is experienced, as would be expected with adaptive control.

## 8 Conclusion Remarks and Future Directions

Process innovation is undoubtfully a most crucial direction toward more effective welding manufacturing. Improvement in desirable properties is often accompanied with increased inconvenience, complexity, unreliability, cost, safety concern, etc., in operation, equipment, etc. Better process innovation roots from good understanding of process physics and essences and is an area that needs endless efforts/improvements. Equipment manufacturers play a critical role in making process innovations to usable processes by addressing accompanied issues.

Numerical analysis will undoubtfully play an increasingly important role in most effectively using available processes for more effective welding manufacturing. The physics involved in welding manufacturing is complex but is well governed by physical laws and constraints. Increased computational power and improved ways of solutions are increasingly improving our capabilities to obtain accurate understanding and prediction of the process phenomena and outcomes toward improved design of welding manufacturing.

Abilities to sense and adapt to process conditions provide an assurance to actually produce the result from welding manufacturing as expected/predicted by the design. The basic welding phenomena such as the radiations and common demands to know what happen underneath the work-piece are the physics imposing the fundamental challenges for sensing and adaptation. The increased variety of innovative processes with various properties but different physics/operations adds to the challenges. Sensors and signals that can be used are available to all of us and the key to address these challenges is how to select the most relevant sensors and signals. Increasing the number of sensors and signals increases the side effects and compromises quality of the solutions. Selecting the most relevant, and just needed, sensors and signals is the right direction. Machine learning provides an effective and efficient way to assure extracting useful feedback from selected signals. Model predictive control provides an effective method for welding engineers to use the extracted feedback to adapt to changed conditions in a scientific way.


## Acknowledgment

The authors thank their colleagues and graduate students, at the University of Kentucky, Edison Welding Institute, the Ohio State University, and Korean Advanced Institute of Science and Technology, who directly and indirectly contributed the works reviewed in this paper. Professor Suck-Joo Na also thanks L. J. Zhang, J. Ning, and C. H. Wang at Xi'an Jiaotong University School of Materials Science and Engineering for helping collect and sort out materials used in this paper for seam tracking in laser welding.


## Conflict of Interest

There are no conflicts of interest.

## References


[1] AWS D1.3/D1.3M:2018, 2018, *An American National Standard: Structural Welding Code—Sheet Steel*, 6th ed., American Welding Society, Miami, FL.
[2] Welding Handbook, 2007, *Volume 3—Welding Processes Part 2*, 9th ed., American Welding Society, Miami, FL.
[3] Welding Handbook, 2004, *Volume 2—Welding Processes Part 1*, 9th ed., American Welding Society, Miami, FL.
[4] Paskell, T., LUndin, C., and Castner, H., 1997, "GTAW Flux Increases Weld Joint Penetration," Weld. J., **76**(4), pp. 57–62.
[5] Howse, D. S., and Lucas, W., 2000, "Investigation Into Arc Constriction by Active Fluxes for Tungsten Inert Gas Welding," Sci. Technol. Weld. Joi., **5**(3), pp. 189–193.
[6] Lu, S. P., Fujii, H., Sugiyama, H., Tanaka, M., and Nogi, K., 2002, "Weld Penetration and Marangoni Convection With Oxide Fluxes in GTA Welding," Mater. Trans., **43**(11), pp. 2926–2931.
[7] Chen, S. J., Jiang, F., Lu, Y. S., and Zhang, Y. M., 2014, "Separation of Arc Plasma and Current in Electrical Arc—An Initial Study," Weld. J., **93**(7), pp. 253s–261s.
[8] Soderstrom, E. J., Scott, K. M., and Mendez, P. F., 2011, "Calorimetric Measurement of Droplet Temperature in GMAW," Weld. J., **90**(4), pp. 77S–84S.
[9] Ogino, Y., and Hirata, Y., 2015, "Numerical Simulation of Metal Transfer in Argon Gas-Shielded GMAW," Weld. World, **59**(4), pp. 465–473.
[10] Hu, J., and Tsai, H. L., 2006, "Effects of Current on Droplet Generation and Arc Plasma in Gas Metal Arc Welding," J. Appl. Phys., **100**(5), p. 053304.
[11] Nguyen Van, A., Tashiro, S., Van, B., and Tanaka, M., 2017, "Development of Plasma-MIG Hybrid Welding Process," J. Japan Weld. Soc., **35**(2), pp. 132–136.
[12] Ton, H., 1975, "Physical Properties of the Plasma-MIG Welding Arc," J. Phys. D Appl. Phys., **8**(8), pp. 922–933.
[13] AWS, 1973, *Recommended Practices for Plasma-Arc Welding—AWS C5.1-73 an American National Standard*, American Welding Society, Miami, FL.
[14] Zhang, S. B., and Zhang, Y. M., 2001, "Efflux Plasma Charge-Based Sensing and Control of Joint Penetration During Keyhole Plasma Arc Welding," Weld. J., **80**(7), pp. 157S–162S.
[15] Jarvis, B. L., and Ahmed, N. U., 2000, "Development of Keyhole Mode Gas Tungsten Arc Welding Process," Sci. Technol. Weld. Joi., **5**(1), pp. 1–7.
[16] Lathabai, S., Jarvis, B. L., and Barton, K. J., 2001, "Comparison of Keyhole and Conventional Gas Tungsten arc Welds in Commercially Pure Titanium," Mater. Sci. Eng. A Struct. Mater., **299**(1–2), pp. 81–93.
[17] Lohse, M., Fuessel, U., Schuster, H., Friedel, J., and Schnick, M., 2013, "Keyhole Welding With CF-TIG (Cathode Focussed GTA)," Weld. World, **57**(5), pp. 735–741.
[18] Feng, Y., Luo, Z., Liu, Z., Li, Y., Luo, Y., and Huang, Y., 2015, "Keyhole Gas Tungsten Arc Welding of AISI 316L Stainless Steel," Mater. Des., **85**, pp. 24–31.
[19] Liu, Z., Fang, Y., Cui, S., Luo, Z., Liu, W., Liu, Z., Jiang, Q., and Yi, S., 2016, "Stable Keyhole Welding Process With K-TIG," J. Mater. Process. Technol., **238**, pp. 65–72.
[20] Liu, Z., Fang, Y., Cui, S., Yi, S., Qiu, J., Jiang, Q., Liu, W., and Luo, Z., 2017, "Keyhole Thermal Behavior in GTAW Welding Process," Int. J. Therm. Sci., **114**, pp. 352–362.
[21] Cui, S., Liu, Z., Fang, Y., Luo, Z., Manladan, S. M., and Yi, S., 2017, "Keyhole Process in K-TIG Welding on 4 mm Thick 304 Stainless," J. Mater. Process. Technol., **243**, pp. 217–228.
[22] Liu, Z., Fang, Y., Qiu, J., Feng, M., Luo, Z., and Yuan, J., 2017, "Stabilization of Weld Pool Through Jet Flow Argon Gas Backing in C-Mn Steel Keyhole TIG Welding," J. Mater. Process. Technol., **250**, pp. 132–143.
[23] Liu, Z., Fang, Y., Cui, S., Yi, S., Qiu, J., Jiang, Q., Liu, W., and Luo, Z., 2017, "Sustaining the Open Keyhole in Slow-Falling Current Edge During K-TIG Process: Principle and Parameters," Int. J. Heat Mass Transfer, **112**, pp. 255–266.
[24] Fan, W., Ao, S., Huang, Y., Liu, W., Li, Y., Feng, Y., Luo, Z., and Wu, B., 2017, "Water Cooling Keyhole Gas Tungsten Arc Welding of HSLA Steel," Int. J. Adv. Manuf. Technol., **92**(5–8), pp. 2207–2216.
[25] Fei, Z., Pan, Z., Cuiuri, D., Li, H., Wu, B., Ding, D., Su, L., and Gazder, A. A., 2018, "Investigation Into the Viability of K-TIG for Joining Armour Grade Quenched and Tempered Steel," J. Manuf. Process., **32**, pp. 482–493.
[26] Li, X., Gong, B., Deng, C., and Li, Y., 2018, "Failure Mechanism Transition of Hydrogen Embrittlement in AISI 304 K-TIG Weld Metal Under Tensile Loading," Corros. Sci., **130**, pp. 241–251.
[27] Fang, Y., Liu, Z., Cui, S., Zhang, Y., Qiu, J., and Luo, Z., 2017, "Improving Q345 Weld Microstructure and Mechanical Properties With High Frequency Current Arc in Keyhole Mode TIG Welding," J. Mater. Process. Technol., **250**, pp. 280–288.
[28] Bachmann, M., Gumenyuk, A., and Rethmeier, M., 2016, "Welding With High-Power Lasers: Trends and Developments," Phys. Procedia, **83**, pp. 15–26.
[29] Svenungssona, J., Choqueta, I., and Kaplanb, A. F. H., 2015, "Laser Welding Process—A Review of Keyhole Welding Modelling," Phys. Procedia, **78**, pp. 182–191.
[30] Stanciu, E. M., Păvălache, A. C., Dumitru, G. M., Dontu, O. G., Besnea, D., and Vasile, I. M., 2010, "Mechanism of Keyhole Formation in Laser Welding, The Romanian Review Precision Mechanics," Opt. Mechatron., **20**(38), pp. 171–176.
[31] Zhang, M. J., Tang, K., Zhang, J., Mao, C., Hu, Y., and Chen, G., 2018, "Effects of Processing Parameters on Underfill Defects in Deep Penetration Laser Welding of Thick Plates," J. Adv. Manuf. Technol., **96**(1–4), pp. 491–501.
[32] Matsumoto, N., Kawahito, Y., Nishimoto, K., and Katayama, S., 2017, "Effects of Laser Focusing Properties on Weldability in High-Power Fiber Laser Welding of Thick High-Strength Steel Plate," J. Laser Appl., **29**(1), p. 012003.
[33] Bunaziv, I., Dørum, C., Nielsen, S. E., Suikkanen, P., Ren, X., Nyhus, B., Eriksson, M., and Akselsen, O. M., 2020, "Laser-arc Hybrid Welding of 12- and 15-mm Thick Structural Steel," Int. J. Adv. Manuf. Technol., **107**(5–6), pp. 2649–2669.
[34] Liu, L. M., and Hao, X. F., 2009, "Improvement of Laser Keyhole Formation With the Assistance of Arc Plasma in the Hybrid Welding Process of Magnesium Alloy," Opt. Lasers Eng., **47**(11), pp. 1177–1182.
[35] Zhang, Y. M., and Liu, Y. C., 2003, "Modeling and Control of Quasi-Keyhole Arc Welding Process," Control Eng. Pract., Award Winning Applications-2002 IFAC World Congress, **11**(12), pp. 1401–1411.
[36] Lu, W., Zhang, Y. M., and Lin, W.-Y., 2004, "Nonlinear Interval Model Control of Quasi-Keyhole Arc Welding Process," Automatica, **40**(5), pp. 805–813.
[37] Lu, W., Zhang, Y. M., and Emmerson, J. E., 2004, "Sensing of Weld Pool Surface Using Non-Transferred Plasma Charge Sensor," Meas. Sci. Technol., **15**(5), pp. 991–999.

[38] Lu, W., and Zhang, Y., 2006, "Robust Sensing and Control of the Weld Pool Surface," Meas. Sci. Technol., **17**(9), pp. 2437–2446.
[39] Zhang, Y. M., and Liu, Y. C., 2007, "Control of Dynamic Keyhole Process," Automatica, **43**(5), pp. 876–884.
[40] Li, Y., Wang, L., and Wu, C., 2019, "Simulation of Keyhole Plasma Arc Welding With Electro-Magneto-Thermo-Hydrodynamic Interactions," Int. J. Adv. Manuf. Technol., **101**(9–12), pp. 9–12.
[41] Jia, C. B., Liu, X. F., Wu, C. S., and Lin S. B., 2018, "Stereo Analysis on the Keyhole and Weld Pool Behaviors in K-PAW With Triple CCD Cameras," J. Manuf. Process., **32**, pp. 754–762.
[42] Zhang, G., Wu, C., and Chen, J., 2018, "Single CCD-Based Sensing of Both Keyhole Exit and Weld Pool in Controlled-Pulse PAW," Weld. World, **62**(2), pp. 377–383.
[43] Zhang, G. K., Chen, J., and Wu, C. S., 2017, "Simultaneous Sensing of Weld Pool and Keyhole in Controlled-Pulse PAW The Behaviors of the Keyhole and the Weld Pool in Plasma Arc Welding Can be Used to Indicate Weld Quality," Weld. J., **96**(3), pp. 95s–103s.
[44] Liu, Z. M., Wu, C. S., Liu, Y. K., and Luo, Z., 2015, "Keyhole Behaviors Influence Weld Defects in Plasma Arc Welding Process," Weld. J., **94**(9), pp. 281s–290s.
[45] Liu, Z. M., Liu, Y. K., Wu, C. S., and Luo, Z, 2015, "Control of Keyhole Exit Position in Plasma Arc Welding Process," Weld. J., **94**(6), pp. 196s–202s.
[46] Liu, Z. M., Wu, C. S., and Chen, M. A., 2014, "Experimental Sensing of the Keyhole Exit Deviation From the Torch Axis in Plasma Arc Welding," Int. J. Adv. Manuf. Technol., **71**(5–8), pp. 1209–1219.
[47] Liu, Z. M., Wu, C. S., and Chen, J., 2013, "Sensing Dynamic Keyhole Behaviors in Controlled-Pulse Keyholing Plasma Arc Welding," Weld. J., **92**(12), pp. 381S–389S.
[48] Liu, Z. M., and Wu, C. S., 2013, "Visualization of Dynamic Keyhole Behavior in Waveform-Controlled Plasma Arc Welding," Weld. World, **57**(5), pp. 719–725.
[49] Liu, Z. M., Wu, C. S., and Chen, M. A., 2012, "Visualizing the Influence of the Process Parameters on the Keyhole Dimensions in Plasma Arc Welding," Meas. Sci. Technol., **23**(10), p. 105603.
[50] Chandrasekhar, N., and Vasudevan, M., 2010, "Intelligent Modeling for Optimization of A-TIG Welding Process," Mater. Manuf. Processes, **25**(11), pp. 1341–1350, Article Number: PII 931352672.
[51] Sharma, P., and Dwivedi, D. K., 2019, "A-TIG Welding of Dissimilar P92 Steel and 304H Austenitic Stainless Steel: Mechanisms, Microstructure and Mechanical Properties," J. Manuf. Process., **44**, pp. 166–178.
[52] Pandey, C., Mahapatra, M. M., Kumar, P., and Saini, N., 2018, "Dissimilar Joining of CSEF Steels Using Autogenous Tungsten-Inert Gas Welding and Gas Tungsten Arc Welding and Their Effect on Delta-Ferrite Evolution and Mechanical Properties," J. Manuf. Process., **31**, pp. 247–259.
[53] Vidyarthy, R. S., and Dwivedi, D. K., 2018, "Microstructural and Mechanical Properties Assessment of the P91 A-TIG Weld Joints," J. Manuf. Process., **31**, pp. 523–535.
[54] Vora, J. J., and Badheka, V. J., 2017, "Experimental Investigation on Microstructure and Mechanical Properties of Activated TIG Welded Reduced Activation Ferritic/Martensitic Steel Joints," J. Manuf. Process., **25**, pp. 85–93.
[55] Arivazhagan, B., and Vasudevan, M., 2015, "Studies on A-TIG Welding of 2.25Cr-1Mo (P22) Steel," J. Manuf. Process., **18**, pp. 55–59.
[56] Gu, Y., Deng, Z., Shi, Y., Li, G., and Zhang, G., 2019, "Process and Performance of Cu/W Dissimilar Metal Welded by A-TIG Arc Spot Welding," Rare Metal Mater. Eng., **48**(3), pp. 947–952.
[57] Li, C., Shi, Y., Gu, Y., and Yang, F., 2017, "Effect of Oxide on Surface Tension of Molten Metal," RSC Adv., **7**(85), pp. 53941–53950.
[58] Mishra, R. S., and Ma, Z. Y., 2005, "Friction Stir Welding and Processing," Mater. Sci. Eng. R Rep., **50**(1–2), pp. 1–78.
[59] Nandan, R., DebRoy, T., and Bhadeshia, H. K. D. H., 2008, "Recent Advances in Friction-Stir Welding—Process, Weldment Structure and Properties," Prog. Mater. Sci., **53**(6), pp. 980–1023.
[60] Ma, Z. Y., 2008, "Friction Stir Processing Technology: A Review," Metall. Mater. Trans. A, **39A**(3), pp. 642–658.
[61] Liu, F. C., Hovanskib, Y., Miles, M. P., Sorensena, C. D., and Nelson, T. W., 2018, "A Review of Friction Stir Welding of Steels: Tool, Material Flow, Microstructure, and Properties," J. Mater. Sci. Technol., **34**(1), pp. 39–57.
[62] Soundararajan, V., Valant, M., and Kovacevic, R., 2006, "Overview of R&D Work in Friction Stir Welding at SMU," Metall. Mater. Eng., **12**(4), pp. 275–295.
[63] Arbegast, W. J., 2006, "Friction Stir Welding After a Decade of Development—Its Not Just Welding Anymore," Weld. J., **85**(3), pp. 28–35.
[64] Senthil, S. M., Parameshwaran, R., Ragu Nathan, S., Bhuvanesh Kumar, M., and Deepandurai, K., 2020, "A Multi-Objective Optimization of the Friction Stir Welding Process Using RSM-Based-Desirability Function Approach for Joining Aluminum Alloy 6063-T6 Pipes," Struct. Multidiscip. Optim.
[65] Mehri, A., Abdollah-zadeh, A., Habibi, N., Hajian, M., and Wang, J. T., 2020, "The Effects of Rotational Speed on Microstructure and Mechanical Properties of Friction Stir-Welded 7075-T6 Thin Sheet," J. Mater. Eng. Perform., **29**(4), pp. 2316–2323.
[66] Robe, H., Claudin, C., Bergheau, J.-M., and Feulvarch, E., 2019, "R-ALE Simulation of Heat Transfer During Friction Stir Welding of an AA2xxx/AA7xxx Joint on a Large Process Window," Int. J. Mech. Sci., **155**, pp. 31–40.
[67] Zhang, J. L., Chen, X., Xia, D., Huang, G., Tang, A., Jiang, B., and Pan, F., 2020, "Improving Performance of Friction Stir Welded AZ31/AM60 Dissimilar Joint by Adjusting Texture Distribution and Microstructure," Mater. Sci. Eng. A Struct. Mater., **778**, p. 139088.
[68] Abolusoro, O. P., Akinlabi, E. T., and Kailas, S. V., 2020, "Tool Rotational Speed Impact on Temperature Variations, Mechanical Properties and Microstructure of Friction Stir Welding of Dissimilar High-Strength Aluminium Alloys," J. Braz. Soc. Mech. Sci. Eng., **42**(4), p. 176.
[69] McIntosh, C., and Mendez, P. F., 2017, "Experimental Measurements of Fall Voltages in Gas Metal Arc Welding," Weld. J., **96**(4), pp. 121S–132S.
[70] Scotti, A., and Monteiro, L. S., 2012, "A Methodology for Parameterization of the AC MIG/MAG Process," Soldagem Inspecao, **17**(3), pp. 271–277.
[71] Arif, N., and Chung, H., 2014, "Alternating Current-Gas Metal Arc Welding for Application to Thin Sheets," J. Mater. Process. Technol., **214**(9), pp. 1828–1837.
[72] Arif, N., and Chung, H., 2015, "Alternating Current-Gas Metal Arc Welding for Application to Thick Plates," J. Mater. Process. Technol., **222**, pp. 75–83.
[73] Kiran, D. V., Cheon, J., Arif, N., Chung, H., and Na, S.-J., 2016, "Three-Dimensional Finite Element Modeling of Pulsed AC Gas Metal Arc Welding Process," Int. J. Adv. Manuf. Technol., **86**(5–8), pp. 1453–1474.
[74] Ikram, A., and Chung, H., 2017, "The Effect of EN Ratio and Current on Microstructural and Mechanical Properties of Weld Joined by AC-GMAW on Square Groove Butt Joints," Appl. Sci., **7**(3), p. 261.
[75] Ikram, A., Arif, N., and Chung, H., 2016, "Design of an Induction System for Induction Assisted Alternating Current Gas Metal Arc Welding," J. Mater. Process. Technol., **231**, pp. 162–170.
[76] Zhang, Y. M., and Li, K. H., 2016, "Arc Welder and Related System," U.S. Patent No. 9,233,432.
[77] Zhang, Y. M., and Chen, J. S., 2013, "Systems and Methods to Modify Gas Metal Arc Welding and Its Variants," U.S. Patent No. 8,563,896.
[78] Zhang, Y. M., and Chen, J. S., 2012, "Systems and Methods to Modify Gas Metal Arc Welding and Its Variants," U.S. Patent No. 8,278,587.
[79] Li, K. H., Chen, J. S., and Zhang, Y. M., 2007, "Double-Electrode GMAW Process and Control," Weld. J., **86**(8), p. 231S.
[80] Zhang, Y. M., Jiang, M., and Lu, W., 2004, "Double Electrodes Improve GMAW Heat Input Control," Weld. J., **83**(11), pp. 39–41.
[81] Lu, Y., Chen, S., Shi, Y., Li, X., Chen, J., Kvidahl, L., and Zhang, Y. M., 2014, "Double-Electrode Arc Welding Process: Principle, Variants, Control and Developments," J. Manuf. Process., **16**(1), pp. 93–108.
[82] Shi, Y., Zhang, G., Huang, Y., Lu, L., Huang, J., and Shao, Y., 2014, "Pulsed Double-Electrode GMAW-Brazing for Joining of Aluminum to Steel," Weld. J., **93**(6), pp. 216s–224s.
[83] Shi, Y., Shao, L., Huang, J., and Gu, Y., 2013, "Effects of Si and Mg Elements on the Microstructure of Aluminum-Steel Joints Produced by Pulsed DE-GMA Welding-Brazing," Mater. Sci. Technol., **29**(9), pp. 1118–1124.
[84] Huang, J., He, X., Guo, Y., Zhang, Z., Shi, Y., and Fan, D., 2017, "Joining of Aluminum Alloys to Galvanized Mild Steel by the Pulsed DE-GMAW With the Alternation of Droplet Transfer," J. Manuf. Process., **25**, pp. 16–25.
[85] Zhou, X., Zhang, G., Shi, Y., Zhu, M., and Yang, F., 2017, "Microstructures and Mechanical Behavior of Aluminum-Copper Lap Joints," Mater. Sci. Eng. A Struct. Mater., **705**, pp. 105–113.
[86] Yang, D., Wang, G., and Zhang, G., 2017, "A Comparative Study of GMAW- and DE-GMAW-Based Additive Manufacturing Techniques: Thermal Behavior of the Deposition Process for Thin-Walled Parts," Int. J. Adv. Manuf. Technol., **91**(5–8), pp. 2175–2184.
[87] Yang, D., and Zhang, G., 2017, "Deposition Time and Thermal Cycles of Fabricating Thin-Wall Steel Parts by Double Electrode GMAW Based Additive Manufacturing," 2016 International Conference on Biomaterials, Nanomaterials and Composite Materials (CBNCM 2016) Book Series: MATEC Web of Conferences 88: 01007, Chengdu, China, Nov. 4–6.
[88] Yang, D., He, C., and Zhang, G., 2016, "Forming Characteristics of Thin-Wall Steel Parts by Double Electrode GMAW Based Additive Manufacturing," J. Mater. Process. Technol., **227**, pp. 153–160.
[89] Lu, Y., Zhang, Y., and Kvidahl, L., 2013, "Heat Input Reduction in Fillet Welding Using Bypass and Gap," Weld. J., **92**(12), pp. 390s–400s.
[90] Li, K. H., Zhang, Y. M., Xu, P., and Yang, F. Q., 2008, "High-Strength Steel Welding With Consumable Double-Electrode Gas Metal Arc Welding," Weld. J., **87**(3), pp. 57s–64s.
[91] Li, K., and Zhang, Y. M., 2008, "Consumable Double-Electrode GMAW Part II: Monitoring, Modeling, and Control," Weld. J., **87**(2), pp. 44s–50s.
[92] Li, K., and Zhang, Y. M., 2008, "Consumable Double-Electrode GMAW Part I: The Process," Weld. J., **87**(1), pp. 11s–17s.
[93] Shi, Y., Liu, X., Zhang, Y., and Johnson, M., 2008, "Analysis of Metal Transfer and Correlated Influences in Dual-Bypass GMAW of Aluminum," Weld. J., **87**(9), pp. 229s–236s.
[94] Li, K., and Zhang, Y. M., 2007, "Metal Transfer in Double-Electrode Gas Metal Arc Welding," ASME J. Manuf. Sci. Eng., **129**(6), pp. 991–999.
[95] Lu, Y., Chen, J., and Zhang, Y., 2015, "Dynamic Model of Consumable Double-Electrode Submerged Arc Welding Process," ASME J. Manuf. Sci. Eng., **137**(2), p. 021001.
[96] Lu, Y., Chen, J. S., Zhang, Y. M., and Kvidahl, L., 2014, "Predictive Control Based Double-Electrode Submerged Arc Welding for Fillet Joints," J. Manuf. Process., **16**(4), pp. 415–426.
[97] Li, K., and Zhang, Y., 2010, "Interval Model Control of Consumable Double-Electrode Gas Metal Arc Welding Process," IEEE Trans. Autom. Sci. Eng., **7**(4), pp. 826–839.
[98] ESAB. THE ICE™ ADVANTAGE. https://www.esab.ca/ca/en/automation/process-solutions/saw/saw-ice/index.cfm, Accessed August 16, 2020.
[99] Parks, J. M., and Stava, E. K., 1991, Apparatus and Method of Short Circuiting Arc Welding, U.S. Patent #5,003,154.

[100] Stava, E. K., 1992, System and Method of Short Circuiting Arc Welding, U.S. Patent #5,148,001.
[101] Stava, E. K., 1993, "A New, Low-Spatter Arc Welding Machine," Weld. J., **72**(1), pp. 25–29.
[102] Pickin, C. G., Williams, S. W., and Lunt, M., 2011, "Characterisation of the Cold Metal Transfer (CMT) Process and Its Application for Low Dilution Cladding," J. Mater. Process. Technol., **211**(3), pp. 496–502.
[103] Feng, J., Zhang, H., and He, P., 2009, "The CMT Short-Circuiting Metal Transfer Process and Its Use in Thin Aluminium Sheets Welding," Mater. Des., **30**(5), pp. 1850–1852.
[104] Silwal, B., Walker, J., and West, D., 2019, "Hot-Wire GTAW Cladding: Inconel 625 on 347 Stainless Steel," Int. J. Adv. Manuf. Technol., **102**(9–12), pp. 3839–3848.
[105] Oreper, G. M., Szekely, J., and Eager, T. W., 1986, "The Role of Transient Convection in the Melting and Solidification in Arc Weldpools," Metall. Trans. B, **17B**(4), pp. 735–744.
[106] Zhang, W., Kim, C.-H., and DebRoy, T., 2004, "Heat and Fluid Flow in Complex Joints During Gas Metal Arc Welding—Part II: Application to Fillet Welding of Mild Steel," J. Appl. Phys., **95**(9), pp. 5220–5229.
[107] Chen, X., Mu, Z., Hu, R., Liang, L., Murphy, A. B., and Pang, S., 2019, "A Unified Model for Coupling Mesoscopic Dynamics of Keyhole, Metal Vapor, Arc Plasma, and Weld Pool in Laser-Arc Hybrid Welding," J. Manuf. Process., **41**, pp. 119–134.
[108] DebRoy, T., Wei, H. L., Zuback, J. S., Mukherjee, T., Elmer, J. W., Milewski, J. O., Beese, A. M., Wilson-Heid, A., De, A., and Zhang, W., 2018, "Additive Manufacturing of Metallic Components—Process, Structure and Properties," Prog. Mater. Sci., **92**, pp. 112–224.
[109] Cook, P. S., and Murphy, A. B., 2020, "Simulation of Melt Pool Behaviour During Additive Manufacturing: Underlying Physics and Progress," Addit. Manuf., **31**, p. 100909.
[110] Goldak, J. A., and Akhlaghi, M., 2005, *Computational Welding Mechanics*, Springer, New York.
[111] Svensson, L., Gretoft, B., and Bhadeshia, H., 1986, "An Analysis of Cooling Curves From the Fusion Zone of Steel Weld Deposits," Scand. J. Metall., **15**(2), p. e103.
[112] Arrizubieta, J. I., Lamikiz, A., Klocke, F., Martínez, S., Arntz, K., and Ukar, E., 2017, "Evaluation of the Relevance of Melt Pool Dynamics in Laser Material Deposition Process Modeling," Int. J. Heat Mass. Tran., **115**(Part A), pp. 80–91.
[113] Zhang, W., Roy, G. G., Elmer, J. W., and DebRoy, T., 2003, "Modeling of Heat Transfer and Fluid Flow During Gas Tungsten Arc Spot Welding of Low Carbon Steel," J. Appl. Phys., **93**(5), pp. 3022.
[114] Gao, X. S., Wu, C. S., Goecke, S. F., and Kügler, H., 2017, "Numerical Simulation of Temperature Field, Fluid Flow and Weld Bead Formation in Oscillating Single Mode Laser-GMA Hybrid Welding," J. Mater. Process. Technol., **242**(5), pp. 147–159.
[115] Youngs, D. L., 1982, "Time-Dependent Multi-Material Flow With Large Fluid Distortion," *Numerical Methods for Fluid Dynamics*, K. W. Morton, and M. J. Baines, eds., Academic Press, Reading, UK.
[116] Sahoo, P., DebRoy, T., and McNallan, M., 1988, "Surface Tension of Binary Metal—Surface Active Solute Systems Under Conditions Relevant to Welding Metallurgy," Metall Trans B, **19**(3), pp. 483–491.
[117] Simonds, B. J., Sowards, J. W., Hadler, J., Pfeif, E., Wilthan, B., Tanner, J., Harris, C., Williams, P. A., and Lehman, J., 2018, "Dynamic and Absolute Measurements of Laser Coupling Efficiency During Laser Spot Welds," Proc. CIRP, **74**, pp. 632–635.
[118] Bayat, M., Mohanty, S., and Hattel, J. H., 2019, "Multiphysics Modelling of Lack-of-Fusion Voids Formation and Evolution in IN718 Made by Multi-Track/Multi-Layer L-PBF," Int. J. Heat Mass Transfer, **139**, pp. 95–114.
[119] Zhang, L. J., Zhang, J. X., Gumenyuk, A., Rethmeier, M., and Na, S. J., 2014, "Numerical Simulation of Full Penetration Laser Welding of Thick Steel Plate With High Power High Brightness Laser," J. Mater. Process. Technol., **214**, pp. 1710–1720.
[120] Kaplan, A., 1994, "A Model of Deep Penetration Laser Welding Based on Calculation of the Keyhole Profile," J. Phys. D Appl. Phys., **27**(9), pp. 1805–1814.
[121] Cho, J. H., and Na, S. J., 2009, "Three-Dimensional Analysis of Molten Pool in GMA-Laser Hybrid Welding," Weld. J., **88**(2), pp. 35–43.
[122] Guerdoux, S., and Fourment, L., 2009, "A 3D Numerical Simulation of Different Phases of Friction Stir Welding," Model. Simul. Mater. Sci., **17**(7), pp. 1–32.
[123] Ulysse, P., 2002, "Three-Dimensional Modeling of the Friction Stir-Welding Process," Int. J. Mach. Tool Manuf., **42**(14), pp. 1549–1557.
[124] Colegrove, P. A., and Shercliff, H. R., 2004, "Development of Trivex Friction Stir Welding Tool Part 2—Three-dimensional Flow Modelling," Sci. Technol. Weld. Joi., **9**(4), pp. 352–361.
[125] Yu, Z., Zhang, W., Choo, H., and Feng, Z., 2012, "Transient Heat and Material Flow Modeling of Friction Stir Processing of Magnesium Alloy Using Threaded Tool," Metall. Mat. Trans. A, **43**(2), pp. 724–737.
[126] De, A., Bhadeshia, H. K. D. H., and DebRoy, T., 2014, "Friction Stir Welding of Mild Steel: Tool Durability and Steel Microstructure," Mater. Sci. Technol., **30**(9), pp. 1050–1056.
[127] Brust, F. W., Hill, M. R., and Yang, Y. P., 2018, *Welding Handbook*, 10th ed., Vol. 1, American Welding Society, Miami, FL.
[128] Brust, F. W., Dodds, R. H., Hobbs, J., Stoltz, B., and Wells, D., 2019, "Weld Residual Stress and Fracture Behavior of NASA Layered Pressure Vessels," Proceedings of the ASME 2019 Pressure Vessels & Piping Conference, PVP2019-94021, July 14–19, San Antonio, TX.
[129] Dong, P., and Brust, F. W., 2000, "Welding Residual Stresses and Effects on Fracture in Pressure Vessel and Piping Components: A Millennium Review and Beyond," J. Pressure Vessel Technol., **122**(3), pp. 329–338.
[130] Feng, Z., 2005, *Processes and Mechanisms of Welding Residual Stress and Distortion*, Woodhead Publishing, Cambridge, UK.
[131] Michaleris, P., 2011, *Minimization of Welding Distortion and Buckling. Modelling and Implementation*, Woodhead Publishing, Cambridge, UK.
[132] Yang, Y. P., Brust, F. W., Zhang, J., Cao, Z., Dong, Y., Nanjundan, A., Varol, I., and Jutla, T., 2000, "Weld Modeling Procedures Development of Lap Joint," International Conference on Computer Engineering and Science, in Advances in Computational Engineering & Sciences, S. N. Atluri and F. W. Brust, eds., Los Angeles, CA, Aug. 21–25, Tech Science Press, pp. 708–713.
[133] Yang, Y. P., Brust, F. W., Cao, Z., Dong, Y., and Nanjundan, A., 2002, "Welding-Induced Distortion Control Techniques in Heavy Industries," Proceedings of the 6th International Conference on Trends in Welding Research, in Trends in Welding Research, Pine Mountain, GA, Apr. 15–19, pp. 844–849.
[134] Yang, Y. P., Jamshidinia, M., Boulware, P., and Kelly, S., 2017, "Prediction of Microstructure, Residual Stress, and Deformation in Laser Powder Bed Fusion Process," Comput. Mech., **61**(5), pp. 599–615.
[135] Yang, Y. P., Brust, F. W., and Kennedy, J. C., 2002, "Lump-Pass Welding Simulation Technology Development for Shipbuilding Applications," ASME Pressure Vessels and Piping Conference, in PVP2002-1105, Vancouver, British Columbia, Canada, Aug. 4–8, pp. 47–54.
[136] Sun, Y., Li, D., Zhang, Z., Yan, D., and Shi, Q., 2011, "Establishment of Traveling Temperature Function Method and Its Application on Welding Distortion Prediction of Cylindrical and Conical Aluminum Alloy Structures," Acta Metall. Sin., **47**, pp. 1403–1407.
[137] Sun, Y., Shi, Q., Sun, K., Chen, G., and Meng, L., 2012, "Process Optimization to Control Welding Distortion of High Speed Train Roof by High Efficiency Numerical Simulation," Proceeding of the 9th International Conference on Trends in Welding Research, Chicago, IL, June 4–8, pp. 401–407.
[138] Ueda, Y., and Yuan, M. G., 1993, "Prediction of Residual Stress in Butt Welded Plates Using Inherent Strain," ASME J. Eng. Mater. Technol., **115**(4), pp. 417–423.
[139] Wang, J., Yuan, H., Ma, N., and Murakawa, H., 2016, "Recent Research on Welding Distortion Prediction in Thin Plate Fabrication by Means of Elastic FE Computation," Mar. Struct., **47**, pp. 42–59.
[140] Wang, J., Yi, B., and Zhou, H., 2018, "Framework of Computational Approach Based on Inherent Deformation for Welding Buckling Investigation During Fabrication of Lightweight Ship Panel," Ocean Eng., **157**, pp. 202–210.
[141] Zhou, H., and Wang, J., 2018, "Accurate FE Computation for Out-of-Plane Welding Distortion Prediction of Fillet Welding With Considering Self-Constraint," J. Ship Prod. Des., **35**(4), pp. 317–327.
[142] Yang, Y. P., and Athreya, B. P., 2012, *A Local-to-Global Assembling Method to Predict Distortion*, AWS Professional Program in FABTECH Show, Las Vegas, NV.
[143] Yang, Y. P., Castner, H., and Kapustka, N., 2011, "Development of Distortion Modeling Methods for Large Welded Structures," Trans. Soc. Naval Architects Mar. Eng., **119**, pp. 645–653.
[144] Yang, Y. P., and Athreya, B. P., 2013, "An Improved Plasticity-Based Distortion Analysis Method for Large Welded Structures," J. Mater. Eng. Perform., **22**(5), pp. 1233–1241.
[145] Yang, Y. P., Zhang, W., Gan, W., Khurana, S., Xu, J., and Babu, S., 2008, "Online Software Tool for Predicting Weld Residual Stress and Distortion," Proceedings of 2008 ASME Pressure Vessels and Piping Division Conference, PVP2008-61123, Vol. 6: 279–288, Chicago, IL.
[146] Yang, Y. P., Zhang, W., Bohr, J., and Kimchi, M., 2009, "Development of Online Weld Modeling Tool for Automotive Applications," Proceeding of International Automotive Body Congress (IABC), Nov. 4–5, Troy, MI.
[147] Zhang, W., and Yang, Y. P., 2009, "Development and Application of On-Line Weld Modeling Tool," Weld. World, **53**(1/2), pp. 67–75.
[148] Anthony, B. M., Nguyen, V., Feng, Y., David, G. T., and Dayalan, G., 2017, "A Desktop Computer Model of the Arc, Weld Pool and Workpiece in Metal Inert Gas Welding," Appl. Math. Model., **44**, pp. 91–106.
[149] Goldak, J., Charkravarti, A., and Bibby, M., 1984, "New Finite Element Model for Welding Heat Sources," Metall. Trans., **15B**, pp. 300–305.
[150] Balasubramanian, K. R., Suthakar, T., Sankaranarayanasamy, K., and Buvanashekaran, G., 2012, "Finite Element Analysis of Heat Distribution in Laser Beam Welding of AISI 304 Stainless Steel Sheet," Int. J. Manuf. Res., **7**(1), pp. 42–58.
[151] Li, P., Fan, Y., Zhang, C., Zhu, Z., Tian, W., and Liu, A., 2018, "Research on Heat Source Model and Weld Profile for Fiber Laser Welding of A304 Stainless Steel Thin Sheet," Adv. Mater. Sci. Eng., **2018**, p. 5895027.
[152] Kik, T., and Górka, J., 2019, "Numerical Simulations of Laser and Hybrid S700MC T-Joint Welding," Materials (Basel), **12**(3), p. 516.
[153] Wu, C. S., Wang, H. G., and Zhang, Y. M., 2006, "A New Heat Source Model for Keyhole Plasma Arc Welding in FEM Analysis of the Temperature Profile," Weld. J., **85**, pp. 284s–291s.
[154] Yang, Y. P., 2015, "Developing Friction Stir Welding Process Model for ICME Application," J. Mater. Eng. Perform., **24**(1), pp. 202–208.
[155] Zhang, W., Elmer, J. W., and DebRoy, T., 2005, "Integrated Modeling of Thermal Cycles, Austenite Formation, Grain Growth and Decomposition in the Heat Affected Zone of Carbon Steel," Sci. Technol. Weld. Joi., **10**(5), pp. 574–582.
[156] Ion, J. C., Easterling, K. E., and Ashby, M. F., 1984, "A Second Report on Diagrams of Microstructure and Hardness for Heat-Affected Zones in Welds," Acta Metall., **32**(11), pp. 1949–1962.

[157] Kirkaldy, J. S., and Venugopalan, D., 1983, "Prediction of Microstructure and Hardness Ability in Low Alloy Steels, Phase Transformation in Ferrous Alloys," Proc. Int. Conf. 4–6.
[158] Kasuya, T., Yurioka, N., and Okumura, M., 1995, "Methods for Predicting Maximum Hardness of Heat-Affected Zone and Selecting Necessary Preheat Temperature for Steel Welding," Nippon Steel Tech. Rep., **4**, pp. 7–14.
[159] Yu, L., Nakabayashi, Y., Sasa, M., Itoh, S., Kameyama, M., Hirano, S., Chigusa, N., Saida, K., Mochizuki, M., and Nishimoto, K., 2011, "Neural Network Prediction of Hardness in HAZ of Temper Bead Welding Using the Proposed Thermal Cycle Tempering Parameter (TCTP)," ISIJ Int., **51**(9), pp. 1506–1515.
[160] Oates, W. R., and Saitta, A. M., 1998, *Welding Handbook, Vol. 4 (Materials and Applications—Part 2)*, 8th ed., American Welding Society.
[161] Brust, F. W., Dong, P., and Zhang, J., 1997, "A Constitutive Model for Welding Process Simulation Using Finite Element Methods," *Advances in Computational Engineering Science*, S. N. Atluri, and G. Yagawa, eds., Tech Science Press, pp. 51–56.
[162] Yang, Y. P., and Dong, P., 2012, "Buckling Distortions and Mitigation Techniques for Thin-Section Structures," J. Mater. Eng. Perform., **21**(2), pp. 153–160.
[163] Mullins, J., and Gunnars, J., 2009, "Influence of Hardening Model on Weld Residual Stress Distribution," Research Report of Inspecta Technology AB, Stockholm, Sweden. https://www.osti.gov/etdeweb/servlets/purl/963513
[164] Payares-Asprino, M. C., Katsumoto, H., and Liu, S., 2008, "Effect of Martensite Start and Finish Temperature on Residual Stress Development in Structural Steel Welds," Weld. J., **87**(11), pp. 279s–289s.
[165] Yang, Y. P., Dong, P., and Zhang, J., 2000, "A Hot-Cracking Mitigation Technique for Welding High-Strength Aluminum Alloy," Weld. J., **79**(1), pp. 9s–17s.
[166] Li, T., Shi, Q., and Li, H. K., 2007, "Residual Stresses Simulation for Friction Stir Welded Joint," Sci. Technol. Weld. Joi., **12**(8), pp. 664–670.
[167] Yan, D., Shi, Q., and Wu, A., 2009, "Numerical Analysis on the Functions of Stir Tool's Mechanical Loads During Friction Stir Welding," Acta Metall. Sin., **45**, pp. 994–999.
[168] Gou, G., Yang, Y. P., and Chen, H., 2014, "An ICME Approach for Optimizing Thin Welded Structure Design," Engineering, **6**(13), pp. 936–947.
[169] Yang, Y. P., and Gould, J., 2014, "ICME Application in Designing Welded Structures," Thermal Process Modeling: Proceedings From the Fifth International Conference on Thermal Process Modeling and Computer Simulation, Orlando, FL, June 16–18, pp. 209–216.
[170] Deng, D., 2009, "FEM Prediction of Welding Residual Stress and Distortion in Carbon Steel Considering Phase Transformation Effects," Mater. Des., **30**(2), pp. 359–366.
[171] Zhou, H., Zhang, Q., Yi, B., and Wang, J., 2020, "Hardness Prediction Based on Microstructure Evolution and Residual Stress Evaluation During High Tensile Thick Plate Butt Welding," Int. J. Naval Arch. Ocean Eng., **12**, pp. 146–156.
[172] Brust, F. W., and Yang, Y. P., 2002, "Weld Residual Stresses and Cracking in Bimetallic Hot Leg Nuclear Weld," ASME Pressure Vessels and Piping Conference, Aug. 4–8, 2002, Vancouver, British Columbia, Canada.
[173] Yang, Y. P., Babu, S., Vaze, S., Kikel, J., and Dewees, D., 2008, "Crack Mitigation During Buttering and Cladding of A Low Alloy Steel Pipe," Proceedings of the 8th International Conference on Trends in Welding Research, June 2–6, 2008, Pine Mountain, GA.
[174] Yang, Y. P., and Babu, S. S., 2010, "An Integrated Model to Simulate Laser Cladding Manufacturing Process for Engine Repair Applications," Weld. World, **54**(9–10), pp. r298–r307.
[175] Yang, Y. P., Brust, F. W., Fzelio, A., and McPherson, N., 2004, "Weld Modeling of Thin Structures With VFT Software," ASME Pressure Vessels and Piping Conference, July 25–29, 2004, San Diego, CA.
[176] Yang, Y. P., Brust, F. W., and Cao, Z., 2003, "Virtual Fabrication Technology Weld Modeling Tool and Its Applications in Distortion Predictions," ASME Pressure Vessels and Piping Conference, July 20–24, 2003, Cleveland, OH.
[177] Yang, Y. P., and Mohr, W. C., 2015, "Finite Element Creep-Fatigue Analysis of a Welded Furnace Roll for Identifying Failure Root Cause," J. Mater. Eng. Perform., **24**(11), pp. 4388–4399.
[178] Yang, Y. P., and Mohr, W. C., 2016, "Multiphysics Modeling of a Welded Furnace Roll for Improving Creep-Fatigue Life," Weld. J., **95**(11), pp. 431s–441s.
[179] Huang, T. D., Rucker, H. J., and Yang, Y. P., 2019, "An ICME Modeling Application for the Optimization of Tie-Down Weld Sequence in Ship Production," J. Ship Prod. Des., **35**(2), pp. 190–197.
[180] Yang, Y. P., Dull, R., Conrardy, C., Porter, N., Dong, P., and Huang, T. D., 2008, "Transient Thermal Tensioning and Numerical Modeling of Thin Steel Ship Panel Structures," J. Ship Prod., **24**(1), pp. 37–49.
[181] Nagarajan, S., Banerjee, P., Chen, W. H., and Chin, B. A., "Control of the Welding Process Using Infrared-Sensors," IEEE Trans. Rob. Autom., **8**(1), pp. 86–93.
[182] Sreedhar, U., Krishnamurthy, C. V., Balasubramaniam, K., Raghupathy, V. D., and Ravisankar, S., 2012, "Automatic Defect Identification Using Thermal Image Analysis for Online Weld Quality Monitoring," J. Mater. Process. Technol., **212**(7), pp. 1557–1566.
[183] Xiao, X., Liu, X., Cheng, M., and Song, L., 2020, "Towards Monitoring Laser Welding Process via a Coaxial Pyrometer," J. Mater. Process. Technol., **277**, p. 116409.
[184] Wu, S. J., Gao, H. M., Zhang, W., and Zhang, Y. M., 2018, "Measurement of Calibrated Recursive Analytic in the Gas Tungsten Arc Weld Pool Model," Weld. J., **97**(4), pp. 108–119.
[185] Zhang, Y. M., Wu, L., Walcott, B. L., and Chen, D. H., 1993, "Determining Joint Penetration in GTAW With Vision Sensing of Weld-Face Geometry," Weld. J., **72**(10), pp. 463s–469s.
[186] Doong, J. L., Wu, C. S., and Hwang, J. R., 1991, "Infrared Temperature Sensing of Laser-Welding," Int. J. Mach. Tools Manuf., **31**(4), pp. 607–616.
[187] LeCun, Y., Bengio, Y., and Hinton, G., 2015, "Deep Learning," Nature, **521**(7553), pp. 436–444.
[188] Rawlings, J. B., Mayne, D. Q., and Diehl, M. M., 2018, *Model Predictive Control: Theory, Computation, and Design*, 2nd ed., Nob Hill Publishing, LLC, Madison, WI.
[189] Li, C., 2018, "Weld Penetration Identification Based on Convolutional Neural Network," Ph.D. dissertation, University of Kentucky Department of Electrical and Computer Engineering. https://uknowledge.uky.edu/cgi/viewcontent.cgi?article=1137&context=ece_etds
[190] Jiao, W.H., Wang, Q.Y., Cheng, Y.C., and Zhang, Y.M., 2020, "End-to-End Prediction of Weld Penetration: A Deep Learning and Transfer Learning Based Method," J. Manuf. Process.
[191] Feng, Y., Chen, Z., Wang, D., Chen, J., and Feng, Z., 2020, "DeepWelding: A Deep Learning Enhanced Approach to GTAW Using Multisource Sensing Images," IEEE Trans. Ind. Inform., **16**(1), pp. 465–474.
[192] Sassi, P., Tripicchio, P., and Avizzano, C. A., 2019, "A Smart Monitoring System for Automatic Welding Defect Detection," IEEE Trans. Ind. Electron., **66**(12), pp. 9641–9650.
[193] Zhang, Z., Wen, G., and Chen, S., 2019, "Weld Image Deep Learning-Based On-Line Defects Detection Using Convolutional Neural Networks for Al Alloy in Robotic Arc Welding," J. Manuf. Process., **45**, pp. 208–216.
[194] Chen, C.-S., 2013, *Linear Systems Theory and Design*, 4th ed., Oxford University Press, New York.
[195] Agapakis, J. E., Katz, J. M., Koifman, M., Epstein, G. N., Friedman, J. M., Eyring, D. O., and Rutishauser, H. J., 1986, "Joint Tracking and Adaptive Robotic Welding Using Vision Sensing of the Weld Joint Geometry," Weld. J., **65**(11), pp. 33–41.
[196] Weglowski, M. S., 2008, "Modeling and Analysis of the Arc Light Spectrum in GMAW," Weld. J., **87**(8), pp. 212S–218S.
[197] Yu, J. Y., Kim, J. I., and Na, S. J., 2003, "Influence of Reflected Arc Light on Vision Sensors for Automatic GTAW Systems," Weld. J., **82**(2), pp. 36S–42S.
[198] Gao, X. D., Mo, L., Wen, O., and Katayama, S., 2013, "Neural Network Model for Recognizing Joint Offset During Fiber Laser Welding," Weld. J., **92**(9), pp. 251S–257S.
[199] Xue, B., Chang, B., Peng, G., Gao, Y.J., Tian, Z.J., Du, D., and Wang, G.Q., 2019, "A Vision Based Detection Method for Narrow Butt Joints and a Robotic Seam Tracking System," Sensors, **19**(5), p. 1144.
[200] Lei, T., Wang, W., Rong, Y., Xiong, P., and Huang, Y., 2020, "Cross-lines Laser Aided Machine Vision in Tube-to-Tubesheet Welding for Welding Height Control," Opt. Laser Technol., **121**, p. 105796.
[201] Na, S.-J., 2008, *Real-Time Weld Process Monitoring*, Y. Zhang, ed., Woodhead Publishing, Cambridge, UK.
[202] Lu, W., Zhang, Y. M., and Emmerson, J., 2007, "Adaptive Non-Transferred Plasma Charge Sensor and Its Applications," ASME J. Manuf. Sci. Eng., **129**(1), pp. 180–189.
[203] Zhang, Y. M., Li, P. J., and Zhang, S. B., 2002, "Apparatus, System, and Related Method for Sensing a Characteristic of a Workpiece in an Automated Process," U.S. Patent No. 6,437,281.
[204] Richardson, R., and Gutow, D., 1983, "Coaxial Arc Weld Pool Viewing for Process Monitoring and Control," Weld. J., **63**(3), pp. 43–50.
[205] Węglowski, M. S., 2007, "Investigation on the Arc Light Spectrum in GTA Welding," J. Achiev. Mater. Manuf. Eng., **20**, p. 519–522.
[206] Li, P. J., and Zhang, Y. M., 2000, "Analysis of an Arc Light Mechanism and Its Application in Sensing of the GTAW Process," Weld. J., **79**(9), pp. 2525-s.
[207] Kiddee, P., Fang, Z., and Tan, M., 2016, "An Automated Weld Seam Tracking System for Thick Plate Using Cross Mark Structured Light," Int. J. Adv. Manuf. Technol., **87**(9–12), pp. 3589–3603.
[208] Xu, P., Xu, G., Tang, X., and Yao, S., 2008, "A Visual Seam Tracking System for Robotic Arc Welding," Int. J. Adv. Manuf. Technol., **37**(1–2), pp. 70–75.
[209] Xiong, J., and Zou, S., 2019, "Active Vision Sensing and Feedback Control of Back Penetration for Thin Sheet Aluminum Alloy in Pulsed MIG Suspension Welding," J. Process. Control, **77**, pp. 89–96.
[210] Kovacevic, R., Zhang, Y. M., and Ruan, S., 1995, "Sensing and Control of Weld Pool Geometry for Automated GTA Welding," ASME J. Manuf. Sci. Eng., **117**(2), pp. 210–222.
[211] Kovacevic, R., and Zhang, Y. M., 1997, "Real-Time Image Processing for Monitoring of Free Weld Pool Surface," ASME J. Manuf. Sci. Eng., **119**(2), pp. 161–169.
[212] Kovacevic, R., Zhang, Y. M., and Li, L., 1996, "Monitoring of Weld Joint Penetrations Based on Weld Pool Geometrical Appearance," Weld. J., **75**(10), pp. 317s–329s .
[213] Zhang, Y. M., Kovacevic, R., and Li, L., 1996, "Characterization and Real-Time Measurement of Geometrical Appearance of the Weld Pool," Int. J. Mach. Tools Manuf., **36**(7), pp. 799–816,
[214] Wu, C. S., Wang, L., Ren, W. J., and Zhang, X. Y., 2014, "Plasma Arc Welding: Process, Sensing, Control and Modeling," J. Manuf. Process., **16**(1), pp. 74–85.
[215] Zhang, Y. M., Song, H. S., and Saeed, G., 2006, "Observation of a Dynamic Specular Weld Pool Surface," Meas. Sci. Technol., **17**(6), pp. L9–L12.
[216] Zhang, W., Wang, X., and Zhang, Y., 2013, "Analytical Real-Time Measurement of a Three-Dimensional Weld Pool Surface," Meas. Sci. Technol., **24**(11), p. 115011.
[217] Gao, X., You, D., and Katayama, S., 2012, "Seam Tracking Monitoring Based on Adaptive Kalman Filter Embedded Elman Neural Network During High-Power Fiber Laser Welding," IEEE Trans. Ind. Electron., **59**(11), pp. 4315–4325.

[218] Zhou, G., Xu, G., and Gu, X., 2016, "Research on Evaluating Laser Welding Quality Based on Two-Dimensional Array Ultrasonic Probe," Int. J. Adv. Manuf. Technol., **84**(5–8), pp. 1717–1723.
[219] Shao, W. J., Huang, Y., and Zhang, Y., 2018, "A Novel Weld Seam Detection Method for Space Weld Seam of Narrow Butt Joint in Laser Welding," Opt. Laser Technol., **99**, pp. 39–51.
[220] Lee, S. K., and Na, S. J., 2002, "A Study on Automatic Seam Tracking in Pulsed Laser Edge Welding by Using a Vision Sensor Without an Auxiliary Light Source," J. Manuf. Syst., **21**(4), pp. 302–315.
[221] Eriksson, I., Gren, P., and Powell, J., 2010, "New High-Speed Photography Technique for Observation of Fluid Flow in Laser Welding," Opt. Eng., **49**(10), 100503.
[222] Eriksson, I., Powell, J., and Kaplan, A. F. H., 2011, "Measurements of Fluid Flow on Keyhole Front During Laser Welding," Sci. Technol. Weld. Joi., **16**(7), pp. 636–641.
[223] Zhang, Y. X., Zhang, N. F., You, D. Y., Gao, X. D., and Katayama, S. J., 2019, "High-Power Disk Laser Welding Statuses Monitoring Based on Analyses of Multiple-Sensor Signals," J. Manuf. Process., **41**, pp. 221–230. Na 12.
[224] Ancona, A., Spagnolo, V., Lugarà, P. M., and Ferrara, M., 2001, "Optical Sensor for Real-Time Monitoring of $CO_2$ Laser Welding Process," Appl. Opt., **40**(33), pp. 6019–6025.
[225] You, D. Y., Gao, X. D., and Katayama, S., 2015, "Review of Laser Welding Monitoring," Sci. Technol. Weld. Joi., **19**(3), pp. 181–201, 2014.
[226] Mishra, D., Roy, R. B., Dutta, S., Pal, S. K., and Chakravarty, D., 2018, "A Review on Sensor Based Monitoring and Control of Friction Stir Welding Process and a Roadmap to Industry 4.0," J. Manuf. Process., **36**, pp. 373–397.
[227] Fleming, P. A., Hendricks, C. E., Cook, G. E., Wilkes, D. M., Strauss, A. M., and Lammlein, D. H., 2010, "Seam-Tracking for Friction Stir Welded Lap Joints," J. Mater. Eng. Perform., **19**(8), pp. 1128–1132.
[228] Su, H., Wu, C. S., Pittner, A., and Rethmeier, M., 2013, "Simultaneous Measurement of Tool Torque, Traverse Force and Axial Force in Friction Stir Welding," J. Manuf. Process., **15**(4), pp. 495–500.
[229] Mehta, M., Chatterjee, K., and De, A., 2013, "Monitoring Torque and Traverse Force in Friction Stir Welding From Input Electrical Signatures of Driving Motors," Sci. Technol. Weld. Joi., **18**(3), pp. 191–197.
[230] Prater, T., Gibson, B., Cox, C., Cook, G. E., Strauss, A., and Longhurst, W., 2015, "Evaluation of Torque as a Means of In-Process Sensing of Tool Wear in Friction Stir Welding of Metal Matrix Composites," Ind. Rob. Int. J., **42**(3), pp. 192–199.
[231] Fehrenbacher, A., Schmale, J. R., Zinn, M. R., and Pfefferkorn, F. E., 2014, "Measurement of Tool-Workpiece Interface Temperature Distribution in Friction Stir Welding," ASME J. Manuf. Sci. Eng., **136**(2), p. 021009.
[232] Bhat, N. N., Kumari, K., Dutta, S., Pal, S. K., and Pal, S., 2015, "Friction Stir Weld Classification by Applying Wavelet Analysis and Support Vector Machine on Weld Surface Images," J. Manuf. Process., **20**(Part 1), pp. 274–281.
[233] Tarraf, J., Mustapha, S., Fakih, M. A., Harb, M., Wang, H., Ayoub, G., and Hamade, R., 2018, "Application of Ultrasonic Waves Towards the Inspection of Similar and Dissimilar Friction Stir Welded Joints," J. Mater. Process. Technol., **255**, pp. 570–583.
[234] Wang, Y. S., Gao, T., Liu, D., Sun, H. Miao, B., and Qing, X., 2020, "Propagation Characteristics of Ultrasonic Weld-Guided Waves in Friction Stir Welding Joint of Same Material," Ultrasonics, **102**, p. 106058.
[235] Zhang, Y. X., You, D., Gao, X., Wang, C., Li, Y., and Gao, P. P., 2020, "Real-Time Monitoring of High-Power Disk Laser Welding Statuses Based on Deep Learning Framework," J. Intell. Manuf., **31**(4), pp. 799–814.
[236] Liang, R., Yu, R., Luo, Y., and Zhang, Y. M., 2019, "Machine Learning of Weld Joint Penetration From Weld Pool Surface Using Support Vector Regression," J. Manuf. Process., **41**, pp. 23–28.
[237] Atwya, M., and Panoutsos, G., 2020, "Transient Thermography for Flaw Detection in Friction Stir Welding: A Machine Learning Approach," IEEE Trans. Ind. Inform., **16**(7), pp. 4423–4435.
[238] Sudhagar, S., Sakthivel, M., and Ganeshkumar, P., 2019, "Monitoring of Friction Stir Welding Based on Vision System Coupled With Machine Learning Algorithm," Measurement, **144**, pp. 135–143.
[239] Das, B., Pal, S., and Bag, S., 2017, "Torque Based Defect Detection and Weld Quality Modelling in Friction Stir Welding Process," J. Manuf. Process., **27**, pp. 8–17.
[240] Li, X. R., Zhang, Y. M., and Kvidahl, L., 2013, "Penetration Depth Monitoring and Control in Submerged Arc Welding," Weld. J., **92**(2), pp. S48–S56.
[241] Huang, Y.-W., Tung, P.-C., and Wu, C.-Y., 2007, "Tuning PID Control of an Automatic Arc Welding System Using a SMAW Process," Int. J. Adv. Manuf. Technol., **34**(1–2), pp. 56–61.
[242] Little, J., "The Impact of Model-Based Design on Controls, Today and in the Future," Plenary Speech, The 19th World Congress of the International Federation of Automatic Control (IFAC 2014), Cape Town, South Africa, August 24–29, 2014.
[243] Zhang, Y. M., Kovacevic, R., and Li, L., 1996, "Adaptive Control of Full Penetration Gas Tungsten Arc Welding," IEEE Trans. Control Syst. Technol., **4**(4), pp. 394–403.
[244] Zhang, Y. M., and Kovacevic, R., 1998, "Neurofuzzy Model-Based Predictive Control of Weld Fusion Zone Geometry," IEEE Trans. Fuzzy Syst., **6**(3), pp. 389–401.
[245] Santos, T. O., Caetano, R. B., Lemos, J. M., and Coito, F. J., 2000, "Multipredictive Adaptive Control of arc Welding Trailing Centerline Temperature," IEEE Trans. Control Syst. Technol., **8**(1), pp. 159–169.
[246] Tzafestas, S. G., and Kyriannakis, E. J., 2000, "Regulation of GMA Welding Thermal Characteristics via a Hierarchical MIMO Predictive Control Scheme Assuring Stability," IEEE Trans. Ind. Electron., **47**(3), pp. 668–678.
[247] Liu, Y. K., and Zhang, Y. M., 2014, "Model-Based Predictive Control of Weld Penetration in Gas Tungsten Arc Welding," IEEE Trans. Control Syst. Technol., **22**(3), pp. 955–966.
[248] Liu, Y., and Zhang, Y., 2013, "Control of 3D Weld Pool Surface," Control Eng. Pract., **21**(11), pp. 1469–1480.
[249] Anzehaee, M. M., and Haeri, M., 2012, "A New Method to Control Heat and Mass Transfer to Work Piece in a GMAW Process," J. Process Control, **22**(6), pp. 1087–1102.
[250] Zou, S., Wang, Z., Hu, S., Wang, W., and Cao, Y., "Control of Weld Penetration Depth Using Relative Fluctuation Coefficient as Feedback," J. Intell. Manuf., **31**(5), 1203–1213.
[251] Sartipizadeh, H., and Haeri, M., 2018, "Control of Droplet Detachment Frequency in a GMAW Process by a Hybrid Model Predictive Control," ASME J. Dyn. Syst. Meas. Control, **140**(11), p. 111008.
[252] Taysom, B. S., Sorensen, C. D., and Hedengren, J. D., 2016, "Dynamic Modeling of Friction Stir Welding for Model Predictive Control," J. Manuf. Process., **23**, pp. 165–174.
[253] Taysom, B. S., Sorensen, C. D., and Hedengren, J. D., 2017, "A Comparison of Model Predictive Control and PID Temperature Control in Friction Stir Welding," J. Manuf. Process., **29**, pp. 232–241.
[254] Doumanidis, C. C., and Hardt, D. E., 1991, "Multivariable Adaptive-Control of Thermal-Properties During Welding," ASME J. Dyn. Syst. Meas. Control, **113**(1), pp. 82–92.
[255] Suzuki, A., Hardt, D. E., and Valavani, L., 1991, "Application of Adaptive-Control Theory to Online GTA Weld Geometry Regulation," ASME J. Dyn. Syst. Meas. Control, **113**(1), pp. 93–103.
[256] Song, J. B., and Hardt, D. E., 1994, "Dynamic Modeling and Adaptive-Control of the Gas Metal Arc-Welding Process," ASME J. Dyn. Syst. Meas. Control, **116**(3), pp. 405–413.
[257] Doumanidis, C. C., 1995, "Thermal Regulation in Multiple-Source Arc-Welding Involving Material Transformations," Weld. J., **74**(6), pp. S185–S194.
[258] Doumanidis, C. C., 1994, "Modeling and Control of Timeshared and Scanned Torch Welding," ASME J. Dyn. Syst. Meas. Control, **116**(3), pp. 387–395.
[259] Kwon, W. H., Choi, H., Byun, D. G., and Noh, S., 1992, "Recursive Solution of Generalized Predictive Control and Its Equivalence to Receding Horizon Tracking Control," Automatica, **28**(6), pp. 1235–1238.
[260] Doumanidis, C., and Kwak, Y. M., 2002, "Multivariable Adaptive Control of the Bead Profile Geometry in Gas Metal Arc Welding With Thermal Scanning," Int. J. Press. Vessels Piping, **79**(4), pp. 251–262.
[261] Wu, D., Chen, H., Huang, Y., and Chen, S., 2019, "Online Monitoring and Model-Free Adaptive Control of Weld Penetration in VPPAW Based on Extreme Learning Machine," IEEE Trans. Ind. Inform., **15**(5), pp. 2732–2740.
[262] Zhang, K., Li, D. Y., Gui, H., and Li, Z. G., 2018, "Adaptive Control for Laser Welding With Filler Wire of Marine High Strength Steel With Tight Butt Joints for Large Structures," J. Manuf. Process., **36**, pp. 434–441.
[263] Gibson, B., Cook, G., Prater, T., Longhurst, W., Strauss, A. M., and Cox, C. D., 2011, "Adaptive Torque Control of Friction Stir Welding for the Purpose of Estimating Tool Wear," Proc. Inst. Mech. Eng. B J. Eng. Manuf., **225**(B8), pp. 1293–1303.